

GLOBAL ASSESSMENT OF PRECIPITATION
OF RADIATION BELT ELECTRONS BY
ELECTROMAGNETIC WAVES FROM LIGHTNING

A DISSERTATION
SUBMITTED TO THE DEPARTMENT OF ELECTRICAL
ENGINEERING
AND THE COMMITTEE ON GRADUATE STUDIES
OF STANFORD UNIVERSITY
IN PARTIAL FULFILLMENT OF THE REQUIREMENTS
FOR THE DEGREE OF
DOCTOR OF PHILOSOPHY

Erin Selser Gemelos

July 2011

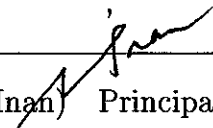
© 2011 by Erin Selser Gemelos. All Rights Reserved.
Re-distributed by Stanford University under license with the author.



This work is licensed under a Creative Commons Attribution-Noncommercial 3.0 United States License.
<http://creativecommons.org/licenses/by-nc/3.0/us/>

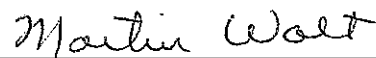
This dissertation is online at: <http://purl.stanford.edu/fv996mh8063>

I certify that I have read this dissertation and that, in my opinion, it is fully adequate in scope and quality as a dissertation for the degree of Doctor of Philosophy.



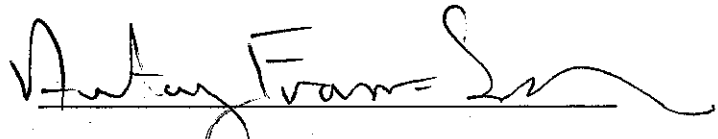
(Umran Inan) Principal Adviser

I certify that I have read this dissertation and that, in my opinion, it is fully adequate in scope and quality as a dissertation for the degree of Doctor of Philosophy.



(Martin Walt)

I certify that I have read this dissertation and that, in my opinion, it is fully adequate in scope and quality as a dissertation for the degree of Doctor of Philosophy.



(Antony Fraser-Smith)

Approved for the University Committee on Graduate Studies

This dissertation is dedicated to my mother.

Abstract

Lightning discharges are well known sources of electromagnetic radiation in the frequency range of a few Hz to many MHz, with the most intense radiation typically being in the range of 5–10 kHz. Electromagnetic waves originating in lightning discharges often propagate through the most densely ionized regions of the Earth's atmosphere and populate the radiation belts. High-energy electrons in this region constitute a hazard to the increasing number of scientific and commercial spacecraft that orbit the Earth, and quantitative understanding of this radiation and its sources and losses are thus important. Electromagnetic whistler waves injected into the radiation belts by lightning discharges can pitch-angle scatter the energetic electrons and cause them to precipitate out of their stably trapped radiation belt orbits and onto the dense upper atmosphere of the Earth.

This dissertation examines the detection of lightning-induced energetic electron precipitation via long-term analysis of in-situ observations of drift loss cone fluxes (i.e., fluxes destined to be precipitated over the South Atlantic Anomaly within ~ 2 hours). The primary measurement tool used is an energetic electron detector (IDP) on board the DEMETER satellite—a French micro-satellite in a sun-synchronous low Earth orbit. Energetic electron flux data are analyzed alongside ground-based lightning data recorded by the National Lightning Detection Network (NLDN) to determine the relationship between drift loss cone fluxes and lightning. While lightning-induced electron precipitation events occur globally, the best region for making in-situ observations of fluctuations in drift loss cone fluxes is over the continental United States. Measurements of VLF wave activity in the typical frequency range

of lightning-generated whistler waves (5–10 kHz) on DEMETER show a substantial increase of electromagnetic wave power over the United States, particularly during the northern summer months when lightning activity is at its highest.

Analysis of particle precipitation data on the DEMETER spacecraft over a three-year period shows that energetic electron fluxes in the drift loss cone exhibit a seasonal dependence consistent with lightning-induced electron precipitation (LEP) being an important source of loss of such energetic radiation. Over the United States, energetic electron fluxes in the slot region ($2 < L < 3$) are significantly higher in the northern summer than in the winter, consistent with the seasonal variation of lightning activity in the Northern Hemisphere. The variation of electron precipitation in energy and L -shell is explored and found to be consistent with expected pitch-angle scattering by lightning-generated whistler waves, indicating that lightning is a significant contributor to the loss of slot region electrons.

To quantitatively relate IDP fluxes with NLDN lightning activity, a physical model of lightning-induced energetic electron precipitation is utilized to determine the size and location of the expected precipitation hot spot for each causative lightning discharge. Incorporation of energy and L -dependent drift periods into the calculation of the precipitation region results in a forward estimation of expected energetic electron precipitation at the satellite location that is then used to quantify the association between lightning and electron precipitation. Assessment of the relationship between lightning and drift loss cone fluxes is performed by correlating the relative fluxes expected from the electron precipitation model with the measured fluxes on the IDP instrument. A peak correlation between measured and expected fluxes of 0.42 for 126 keV electrons at $L \sim 2.2$ indicates that lightning is a significant contributor to the loss of 126 keV electrons. Determination of the energy ranges and L -shell regions for which a strong correlation between expected and measured fluxes exists implies that lightning plays a continuous role in affecting the lifetime of radiation belt electrons, particularly at low energies (100–300 keV) within the slot region ($2 < L < 2.5$).

Acknowledgments

This dissertation represents the culmination of my time here at Stanford. As I complete the final pages of this dissertation, I cannot help but reflect on all of the support that has enabled me to reach where I am today.

I would like to express my gratitude to my principle adviser, Professor Umran Inan, for his guidance and support throughout my years at Stanford. The word ‘impossible’ does not seem to exist in his world. His limitless energy and passion for VLF research were a constant source of inspiration. Thanks to Umran, I traveled to many wonderful, far-off places, including a two-week journey through the South Pacific Ocean that I will never forget.

Throughout my more formative years here, I had the pleasure of working closely with my second adviser, Professor Martin Walt. Martin’s enthusiasm for the field, his approachability, unending helpfulness, and patience were unparalleled, even when mine was not. I would also like to thank Professor Antony Fraser-Smith not only for taking on the role of third reader, but also for taking me under his wing when I was without an adviser, for giving me a desk, a computer, and, most importantly, his friendship. We have had many interesting and enlightening conversations throughout the years, and when the going got tough, he was always nearby with an uplifting story, a bar of dark chocolate, or both.

I would like to thank Professor Phillip Scherrer and Professor Tsachy Weissman for serving on my thesis defense committee. I would also like to thank Dr. J. Bernard Blake of the Aerospace Corporation, who got me started on satellite analysis with the SAMPEX data. Although that data did not work out for the purposes of completing

this dissertation, it was the analysis and understanding of that data that helped me find my way with the DEMETER data. Access to, and understanding of, the DEMETER data was made possible with the help and support of Doctors Michel Parrot, Jean-André Sauvaud, and Jean-Yves Brochot.

Helen Nui and Shaolan Min have saved me more times than I can count. Not only do they ensure the everyday operation of the VLF group runs smoothly, but they also make sure we are paid on time, reimbursed (eventually), and never locked out of our office. Add to that their invaluable friendship, and they are absolutely irreplaceable!

The VLF group, past and present, counts more students than I can possibly name here, so I will instead thank them as a whole. I have enjoyed the many friendships, soccer games (played and watched), and homework sessions shared with various members of the group. There was always someone to talk to about any problem and someone who had already written that horrid piece of code you had just spent weeks trying to reinvent yourself. I particularly cherish the time spent with a few of my good friends within the group, including (but not limited to) Doctors Sarah Harriman, Maria Spasojevic, Benjamin Cotts, and Ryan Said.

I was also fortunate to have spent many years sharing Room 306 with some wonderful people, including Doctors Timothy Chevalier, Robert Marshall, and Cécile Mackay. Throughout the many coffee breaks, afternoon walks, and random discussions that one is wont to undertake when one should be working, great friendships were developed that extend far beyond the office, for which I am eternally grateful.

My decision to come to Stanford was heavily influenced by some wonderful women I met during EE Visit Day many years ago. Doctors Kerri Cahoy, Hrefna Gunnarsdóttir, and Deirdre Robinson O'Brien gave me an inside look at the life of a graduate student and encouraged me to come to Stanford and join them for their daily lunch escapades. Many years later, I am fortunate to still call them wonderful friends and mentors.

Outside of school, I divided my free time between soccer in the spring and summer and triathlons in the autumn and winter. To my soccer teammates Natalie, Alex, Sarah, Sebastien, Paul, Jordan, Scott, and Michelle: thanks for some great soccer and fun times at the Nut House afterwards. To the winter triathlon team: I wouldn't jump into the waters of Redwood Shores with anyone but you.

Last, but certainly not least, are my family. In addition to my own wonderful family who were sort of stuck with me whether they wanted me or not, I inherited through marriage a big fat Greek family that treated me like the daughter/sister/cousin they never had. To Vivian, Michael, and Steven: thank you for your unfailing love and support. To my sisters, Karen and Kristen: thank you for always being there for me, keeping me sane, listening to me vent, and reminding me that there is life outside of my office. To Lauren, David, Ryan, and Trey: thank you for keeping me young at heart and refreshing my memory of algebra and trigonometry on occasion. To my mother: thank you for your unconditional love, support, and encouragement. You believed in me unfailingly and inspired me to always do my best. Finally, to my husband George: thank you for your endless patience and steadfast love throughout this process.

Erin Selser Gemelos

Stanford, California
June 12, 2011

This work has been supported at various times by a Stanford Graduate Fellowship; NASA Graduate Student Research's Program Fellowship NNG05GN78H; the Office of Naval Research via contract number N00014-09-1-0100; and the Office of Naval Research through a Multi-University Research Initiative (MURI) program through subcontract 2882802-A to Stanford University from University of Maryland.

Contents

Abstract	v
Acknowledgments	vii
1 Introduction	1
1.1 Purpose	1
1.2 Scientific Background	2
1.2.1 Magnetosphere	2
1.2.2 Earth's Magnetic Field	4
1.2.3 Van Allen Radiation Belts	6
1.2.4 Loss Cones	10
1.3 Review of Past Work	14
1.4 Thesis Organization	18
1.5 Scientific Contributions	19
2 Lightning-induced Electron Precipitation	20
2.1 Introduction	20
2.2 Wave-particle Interactions	20
2.3 Resonant Energy Calculations	23
2.4 Methods of Detection	27
2.4.1 Ground-based Observations	27
2.4.2 In-situ Observations	29

3	Description of Available Data	31
3.1	Introduction	31
3.2	DEMETER Satellite	31
3.2.1	Detector Details	32
3.2.2	Drift Loss Cone Sampling	34
3.3	NLDN	36
3.4	Location for Observations	36
4	Seasonal Variation of Electron Precipitation	40
4.1	Introduction	40
4.2	Seasonal Variation of Drift Loss Cone Fluxes	40
4.3	Energy and L -shell Dependencies	44
4.4	Day/Night Effect	46
4.5	Yearly Variation of Fluxes and Lightning	48
5	The Physical Connection between Lightning and Electron Fluxes	51
5.1	Introduction	51
5.2	Model of Lightning-induced Precipitation	52
5.2.1	Whistler Wave Simulation	52
5.2.2	Electron Scattering Calculations	55
5.2.3	Gaussian Precipitation Model	56
5.3	Expected Precipitation at Satellite Location	58
5.4	Comparing Modeled and Measured Fluxes	63
5.4.1	Energy and L -shell Characteristics of Precipitation	65
5.4.2	Seasonal Variations in Energy and L Characteristics	67
5.4.3	Poleward Offset of Precipitation Region	71
6	Summary and Future Work	75
6.1	Summary	75
6.2	Suggestions for Future Work	78
6.2.1	Extension of the Forward Estimation Model	78

6.2.2	Effect of Geomagnetic Activity	80
-------	--	----

List of Figures

1.1	Magnetosphere	3
1.2	Earth’s magnetic field	6
1.3	Earth’s radiation belts	7
1.4	Charged particle motion	9
1.5	Loss cone angles	12
1.6	Geomagnetic field strength	13
1.7	Equatorial loss cone pitch angles	14
2.1	Earth-ionosphere waveguide	21
2.2	Lightning-induced electron precipitation	22
2.3	Wave-particle interaction geometry	24
2.4	Cyclotron resonance	26
2.5	Plasmaspheric density	27
2.6	Resonant energy electrons	28
2.7	Ionospheric disturbance	29
3.1	DEMETER orbital ground track	32
3.2	LEP on DEMETER	33
3.3	Mirror point altitudes	35
3.4	Seasonal variation of lightning	37
3.5	5–10 kHz wave spectral intensities on DEMETER	39
4.1	Seasonal variation of drift loss cone fluxes and lightning	43
4.2	Seasonal variation of drift loss cone fluxes over the Pacific Ocean	44

4.3	Ratio of August and December median nighttime fluxes	45
4.4	August and December median nighttime fluxes as a function of L -shell	46
4.5	Ratio of August and December median daytime fluxes	47
4.6	August and December median daytime fluxes as a function of L -shell	47
4.7	Yearly variation of fluxes and lightning	49
5.1	Modeled precipitation energy spatial density	56
5.2	2-D Gaussian model of relative precipitated flux	57
5.3	Flux calculation technique illustrated	61
5.4	Computation procedure flowchart	62
5.5	Example LEP event used to test precipitation model	64
5.6	Example LEP event correlation results	65
5.7	Yearly flux averages	66
5.8	Nighttime correlations in 2007	68
5.9	Spring correlations 2006–2008	69
5.10	Summer correlations 2006–2008	69
5.11	Autumn correlations 2006–2008	70
5.12	Winter correlations 2006–2008	70
5.13	Comparison of ducted and nonducted electron scattering models . . .	73

Chapter 1

Introduction

1.1 Purpose

The purpose of this dissertation is to determine the extent to which lightning plays a role in precipitating energetic electrons from the radiation belts into the atmosphere. The primary tools used for measurements are the DEMETER satellite—a French micro-satellite used to study electromagnetic waves and energetic electrons—and the National Lightning Detection Network (NLDN)—a network of ground-based stations over the United States that detects lightning and measures its location [*Cummins et al.*, 1998]. The specific areas upon which we focus our attention are: (i) the seasonal variation of energetic electron precipitation in relation to lightning; (ii) the ideal geographic location for measuring lightning-induced electron precipitation (LEP) events; and (iii) a quantification of the relationship between electron precipitation and lightning activity, including dependence on energy and magnetic latitude.

The role of lightning in the removing electrons from the radiation belts has long been in question. At relativistic energies (>1 MeV), pitch angle diffusion of radiation belt electrons via cyclotron resonant interaction with plasmaspheric hiss is thought to be the dominant loss mechanism [*Lyons et al.*, 1972; *Lyons and Thorne*, 1973; *Imhof et al.*, 1986]. Recently, *Green et al.* [2005] suggested lightning to be an embryonic source of hiss due to the geographic (preferential occurrence over land masses) and local time (stronger in the afternoon sector) characteristics that are consistent with

properties of lightning [*Christian et al.*, 2003]. Observations of radiation belt losses due to lightning-induced electron precipitation (LEP) [e.g., *Burgess*, 1993; *Voss et al.*, 1998; *Blake et al.*, 2001; *Rodger and Clilverd*, 2002] suggest that LEP may be an important loss mechanism at lower energies (< 500 keV). Theoretical estimates have suggested that LEP might be a significant contributor to electron loss at mid-latitudes [*Abel and Thorne*, 1998a], but experimental evidence of such a global role has been lacking. Through a comparison of global satellite observations of energetic electron precipitation with ground-based lightning detection, we herein present a regionally averaged statistical assessment of accumulated fluxes of electrons in the drift loss cone and determine their relation to lightning. The analysis described in this dissertation represents the first extension of heretofore transient and localized observations of LEP to a regionally averaged assessment of the role of lightning, suggesting that lightning plays an important role in affecting the lifetime of radiation belt electrons in the slot region.

1.2 Scientific Background

The focus of this dissertation is on studying the effect of lightning-generated whistler waves on energetic electrons in the near-Earth space environment. In the following, we examine the physics of this environment, focusing on the magnetosphere and the radiation belts, and discuss the formation of so-called bounce and drift loss cones, which classify the orbits of energetic particles in the radiation belts which are either stably trapped or destined to be precipitated into the Earth's atmosphere.

1.2.1 Magnetosphere

Environmental conditions in the near-Earth space environment are always changing. While space weather is affected by a variety of factors, one of the most important is the solar wind—a stream of charged particles, or plasma, ejected from the Sun's atmosphere. These hot, energetic particles travel through space and around the Earth,

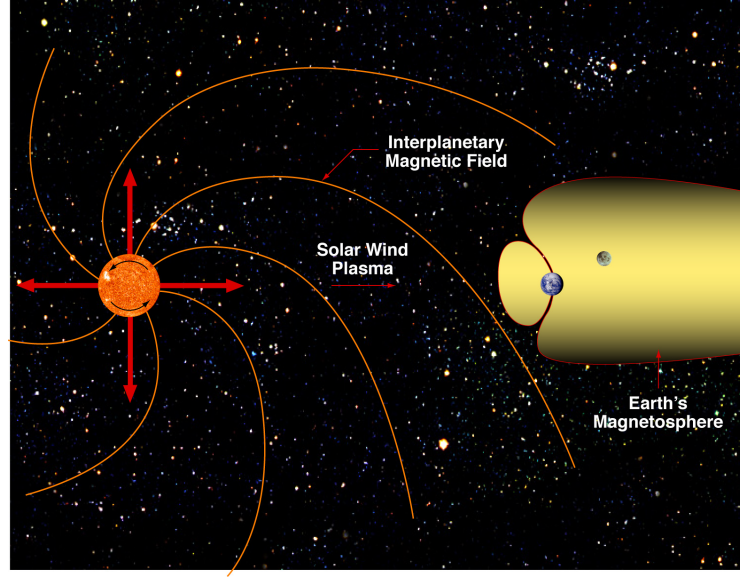


Figure 1.1: Cartoon depicting the Earth’s magnetosphere, compressed on the day side by the solar wind and extending to a cylindrical shape on the night side.

where some of these energetic particles become trapped by the Earth’s magnetic field. The magnetosphere is a region of space where the behavior of the plasma is controlled primarily by the geomagnetic field. The shape of the magnetosphere is determined by the Earth’s internal magnetic field, the solar wind plasma, and the interplanetary magnetic field, and is schematically illustrated in Figure 1.1. In the absence of the Sun and its magnetic field, the Earth’s dipole field would extend to great distances in all directions, but pressure from the solar wind distorts and confines the geomagnetic field. On the day side the boundary between the Earth’s field and the solar wind is compressed to ~ 10 Earth radii (R_E), while on the night side the Earth’s field is stretched to several hundred R_E ($1 R_E \simeq 6370$ km), as seen in Figure 1.1.

This work focuses on the inner regions of the magnetosphere (up to $\sim 5 R_E$) where the geomagnetic field lines are ‘closed.’ The bulk of the inner magnetospheric plasma is composed of ions and ‘cold’ electrons that have a temperature of < 1 eV, and densities of $10\text{--}10^4$ el-cm $^{-3}$. These background populations of cold plasma within the magnetosphere determine the plasma wave properties, and comprise a region known as the ‘plasmasphere.’ Within this so-called plasmaphere, the plasma is “frozen-in” to

the geomagnetic field, and corotates with the Earth. A natural boundary is formed where the density of the plasma drops off by approximately two orders of magnitude at a location termed the ‘plasmopause.’ The location of the plasmopause is highly dependent on geomagnetic activity, but is generally between 3–7 R_E [[Carpenter, 1966](#)]. The inner magnetosphere is also host to a region of high-energy particles, or hot plasma, with energies that range from ~ 1 keV up to 5×10^5 keV. These hot particles comprise what are known as the Van Allen radiation belts and constitute a hazard to satellites travelling through these regions of hot plasma. Understanding the distribution and physical properties, as well as the sources and losses of these radiation belt particles, is of utmost importance to predicting satellite lifetimes and satellite safety in these regions.

1.2.2 Earth’s Magnetic Field

As mentioned above, particle dynamics within the magnetosphere are strongly influenced by the Earth’s magnetic field. It is therefore essential to accurately describe the geomagnetic field at any point in space. The geomagnetic field is most accurately modeled by a multipole expansion, with the expansion coefficients given by the International Geomagnetic Reference Field (IGRF) [[IAGA, 2010](#)]. The IGRF is a series of mathematical models of the Earth’s main field and its annual rate of change. In the absence of external current sources, the magnetic field \mathbf{B} is defined as $-\nabla\psi$, where ψ is the scalar potential which can be represented by a truncated series expansion in the following manner:

$$\psi = R_E \sum_{n=1}^{\infty} \left(\frac{R_E}{r} \right)^{n+1} \sum_{m=0}^n (g_n^m \cos m\phi + h_n^m \sin m\phi) P_n^m(\cos \theta) \quad (1.1)$$

where P_n^m is a Legendre function, and the coefficients g_n^m and h_n^m are contained within the IGRF model.

Due to the $r^{-(n+1)}$ dependence of ψ , the importance of the higher order terms decreases rapidly with distance from the Earth. To zeroth order, the Earth’s magnetic

field can be approximated as a tilted centered dipole, the strength of which can be found by calculating the gradient of the $n=1$, $m=0$ term of the magnetic potential ψ [Walt, 1994, p. 29]. It is then possible to represent the magnetic field, \mathbf{B} , in spherical polar coordinates as

$$B_r(r, \lambda) = -2B_0 \left(\frac{R_E}{r} \right)^3 \sin \lambda \quad (1.2)$$

$$B_\lambda(r, \lambda) = B_0 \left(\frac{R_E}{r} \right)^3 \cos \lambda \quad (1.3)$$

where $B_0 = -g_1^0$ is the mean value of the magnetic field at the Earth's surface along the equator ($\sim 3.12 \times 10^{-5}$ T), R_E is the radius of the Earth (~ 6370 km), r is the distance measured from the center of the dipole field, and $\lambda = 90^\circ - \theta$ is the geomagnetic latitude. The intensity of the dipole field can thus be written as

$$B = \sqrt{(B_r^2 + B_\lambda^2)} = B_0 \left(\frac{R_E}{r} \right)^3 \sqrt{(1 + 3 \sin^2 \lambda)}. \quad (1.4)$$

The above calculation of the dipole field model is useful for illustrative purposes and is often applied when discussing trapped radiation (as seen in the next section), but is insufficient for quantitative calculations. The lack of symmetry and the irregularities of the more realistic multipole expansion model of the geomagnetic field make it difficult to determine geographic coordinates within a three-dimensional grid in a manner such as the one described above.

Instead, we refer to the location of a particle in the radiation belts in terms of the McIlwain L -shell or drift shell on which a particle drifts about the Earth. If the Earth's field were a centered dipole, the L -shell value (in R_E) of a field line would be equal to the distance from the dipole to the equatorial crossing of the field line as seen in Figure 1.2. For example, " $L=2$ " would describe the set of the geomagnetic field lines which cross the Earth's magnetic equator two earth radii (R_E) from the center of the dipole (which, for the centered dipole model, is also the center of the Earth). In the distorted IGRF geomagnetic field model, the L value of a field line is approximately equal to the distance from the Earth's center to the equatorial crossing

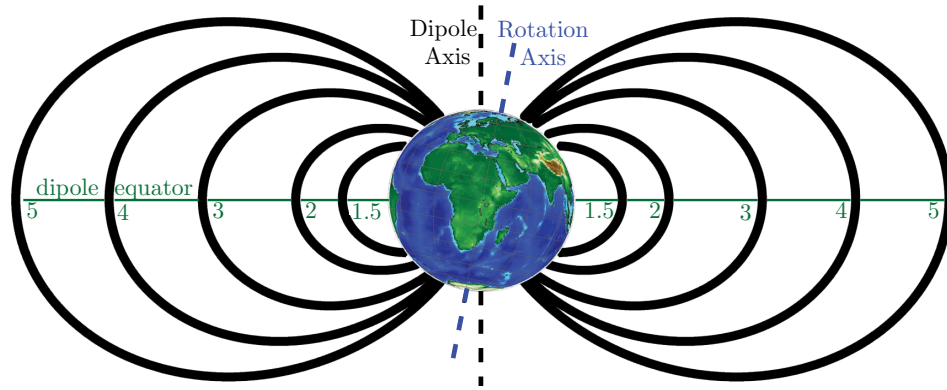


Figure 1.2: Simplistic model of Earth’s magnetic field as a tilted dipole, offset with respect to the Earth’s rotation axis. L -shells, or units of distance along the magnetic equator, are labeled in green.

of the field line, but as the particle drifts around the Earth on a particular L -shell, this distance varies somewhat with longitude.

1.2.3 Van Allen Radiation Belts

The Van Allen radiation belts are comprised of energetic particles, consisting mostly of electrons and protons with energies greater than 100 keV that experience long-term trapping in the geomagnetic field. Three distinct regions of electrons exist in the Earth’s radiation belts. The inner belt, ranging from $1.1 < L < 2$, is comprised of energetic protons as well as electrons with average energies on the order of hundreds of keV. The low-altitude limit of the inner belt ($L = 1.1$) is governed by the Earth’s atmosphere, where frequent collisions between trapped particles and the dense upper atmosphere result in the removal of radiation belt particles. The outer belt, nominally in the region of 3–9 Earth radii above the Earth’s surface, consists of mainly high energy electrons with energies ranging from 100 keV to many MeV. In between these two belts is a region known as the slot region where the electron fluxes have been depleted, as shown in Figure 1.3. It is this region that is the focus of this work.

Radiation belt physics are governed by the Earth’s magnetic field. The fundamental equation describing the motion of a charged particle in the presence

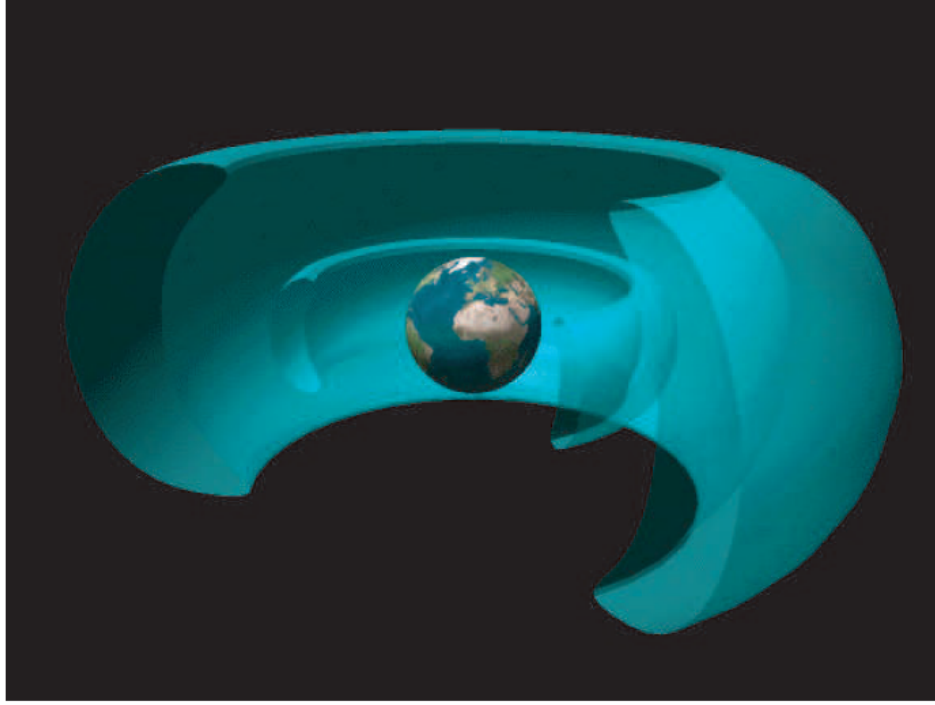


Figure 1.3: Cartoon depicting the Earth's radiation belts, showing the inner and outer radiation belts to scale.

of electric and magnetic fields is the Lorentz Force equation:

$$\mathbf{F} = \frac{d\mathbf{p}}{dt} = q(\mathbf{v} \times \mathbf{B} + \mathbf{E}) \quad (1.5)$$

where \mathbf{p} is the particle momentum, q is the charge of the particle, \mathbf{v} is the particle velocity, \mathbf{B} is the magnetic field, and \mathbf{E} is the electric field.

In the absence of an external electric field, and for conditions when \mathbf{B} is approximately uniform, Equation (1.5) can be separated into components of particle momentum perpendicular and parallel to the magnetic field, giving

$$\left(\frac{d\mathbf{p}}{dt}\right)_{\parallel} = 0 \quad (1.6)$$

$$\left(\frac{d\mathbf{p}}{dt}\right)_{\perp} = q(\mathbf{v}_{\perp} \times \mathbf{B}) \quad (1.7)$$

Integrating Equation (1.6), we find that \mathbf{p}_{\parallel} is a constant, indicating that the particle travels parallel to \mathbf{B} at a constant speed while rotating about \mathbf{B} in a circle with gyroradius

$$\rho = \frac{p_{\perp}}{Bq} \quad (1.8)$$

where p_{\perp} is the particle momentum in the direction perpendicular to the magnetic field. The superposition of the circular motion of the particle perpendicular to \mathbf{B} with a uniform motion parallel to \mathbf{B} describes a helical motion of the particle about the magnetic field. Because the non-uniformities in the field are small over distances the length of the gyroradius, this helical motion is the primary motion of trapped particles in the geomagnetic field [*Walt, 1994*, p. 12].

While the helical motion is the primary motion of a charged particle in a magnetic field, two other prominent periodic motions also exist: bounce motion, and drift motion. The particle gyrates about the magnetic field line while also travelling parallel to the magnetic field. When the particle encounters increased magnetic field intensities closer to the surface of the Earth, it experiences an opposing force that ultimately causes the particle to mirror, or bounce back toward the other hemisphere. Additionally, slight deviations of ∇B perturb the otherwise helical motion of the particle, introducing what are known as gradient and curvature drifts in a direction perpendicular to \mathbf{B} , resulting in a longitudinal drift motion around the Earth. The direction of the drift is charge-dependent, with electrons drifting eastward, and protons westward. An illustration of the gyration, bounce, and drift motions of a charged particle in a magnetic field is shown in Figure 1.4.

Each of the three main types of motion of a charged particle in a magnetic field occurs under vastly different time scales. The magnitude of the gyrofrequency is directly proportional to the magnitude of the Earth's magnetic field, and is typically on the order of $\sim 10^5$ Hz for electrons. The bounce period is a function of electron energy and L -shell, and is typically on the order of 1 second. The location at which the particle reverses directions in its traverse of the geomagnetic field line during its bounce motion is called the mirror point. Like the bounce period, the drift period

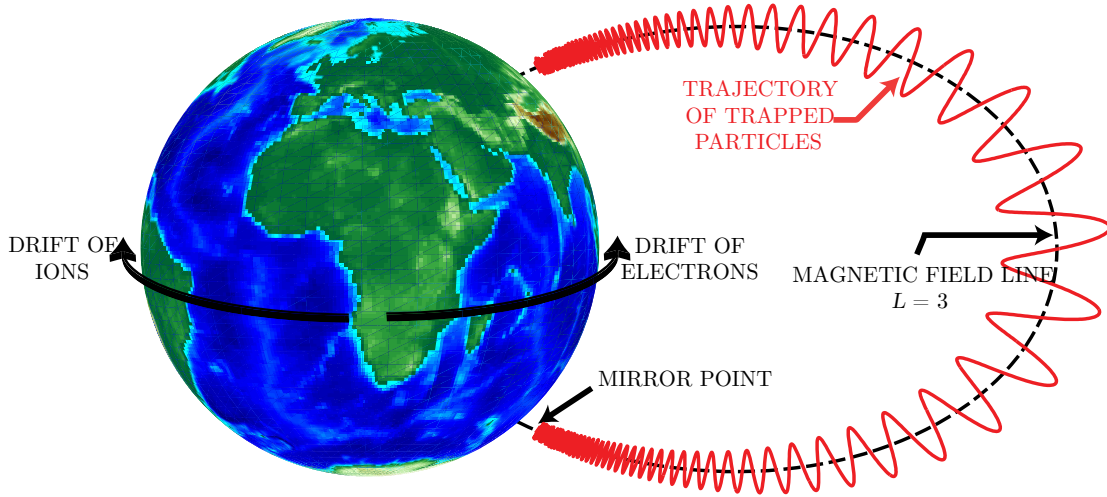


Figure 1.4: Diagram illustrating charged particle motion in the presence of a magnetic field.

also depends on location and energy, and ranges from tens of minutes up to a few hours.

In the absence of outside forces, the trapped energetic particles would remain in their stable orbits indefinitely. However, the particle fluxes exhibit substantial variations over a variety of time scales (see, for example, *Li et al.* [2001, Fig. 1]). Electron fluxes in the radiation belts exhibit variations related to geomagnetic activity, with average flux values changing with the solar cycle. Although the radiation belts have been studied intensely for the last fifty years, the principle source and loss mechanisms of radiation belt particles is still under investigation [*Walt, 1994*, p. 1]. The main source of the electrons fluxes appears to be the solar wind, although the ionosphere also supplies charged particles to the radiation belts.

The loss of radiation belt electrons is likely due to interaction with whistler mode waves, as first suggested by *Dungey* [1963], although the origin and relative contribution of various types of whistler mode waves is uncertain [*Horne, 2002*]. Among these possible wave sources are naturally occurring phenomena such as plasmaspheric hiss and lightning-generated whistler waves, as well as anthropogenic

sources such as VLF transmitter signals. The present work aims to determine the relative contribution of lightning-generated whistler waves to radiation belt losses in the inner belt and slot regions.

1.2.4 Loss Cones

Precipitation is a term commonly used to describe energetic electron loss from the radiation belts. Precipitation occurs when the mirror point of a particle is sufficiently low such that the particle has an enhanced probability of collision with neutral atoms in the dense upper atmosphere of the Earth. Such a collision drastically changes the trajectory of a particle and thereby causes the particle to be released from the influence of the geomagnetic field. The physics behind this phenomenon of particle precipitation is described in the following paragraphs.

For simple field geometries, Equation (1.5), or the Lorentz force equation, can be integrated to give the trajectory of the particle. However, tracking the trajectory of an electron from, for example, Europe to South America would require many numerical integrations of the drift and mirroring force equations, which are likely to be both computationally intensive and prone to cumulative errors. It is therefore pertinent to introduce approximate constants of motion, or so-called ‘adiabatic invariants’, whose values remain constant within the respective periodicity of the equations of motion so long as forces that can change the value of the periodicity are slowly varying.

With respect to the present work, the most important adiabatic invariant is the so-called first adiabatic invariant, which is obtained by integrating the canonical momentum of the charged particle around the particle gyration orbit in the following manner:

$$J_1 = \oint [\mathbf{p} + q\mathbf{A}] \cdot d\mathbf{l} \quad (1.9)$$

where \mathbf{p} is the particle momentum, \mathbf{A} is the vector potential of the magnetic field, and $d\mathbf{l}$ is an element of the particle path around the gyration orbit [[Walt, 1994](#), p.

39]. Solving this integral, we find that

$$J_1 = \frac{\pi p_{\perp}^2}{qB} = \text{constant} \quad (1.10)$$

Removing the constants from the above equation, we are left with the relationship

$$\frac{p_{\perp}^2}{B} = \text{constant} \quad (1.11)$$

This relationship is pivotal in determining the motion of the particle parallel to the field lines. Let the pitch angle, α , of the particle define the angle of the particle velocity vector with respect to the magnetic field

$$\tan \alpha = \frac{v_{\perp}}{v_{\parallel}} \quad (1.12)$$

Thus, we can rewrite Equation (1.11) as

$$\frac{p_{\perp}^2}{B} = \frac{p^2 \sin^2 \alpha}{B} = \text{constant} \quad (1.13)$$

As a particle moves along the magnetic field line towards the Earth, the strength of the magnetic field increases. When the strength of the field increases, p_{\perp}^2 must also increase to maintain the constant relationship described by Equation (1.13). In the absence of electric fields or other forces, p^2 is constant, so α must increase to balance the increase in B . When α reaches 90° , the parallel component of the particle velocity reverses direction and the particle travels towards the other hemisphere.

The distance a particle travels away from the magnetic equator before mirroring is determined by its equatorial pitch angle, α_{eq} , or the angle of the particle velocity with respect to the magnetic field at the equator. A larger equatorial pitch angle results in the particle mirroring at a higher altitude along the field line, as seen in Figure 1.5. If the equatorial pitch angle is sufficiently small, the mirror point of the particle may fall below ~ 100 km, an altitude below which the increased atmospheric density significantly reduces the mean free path of an electron, implying that any particle

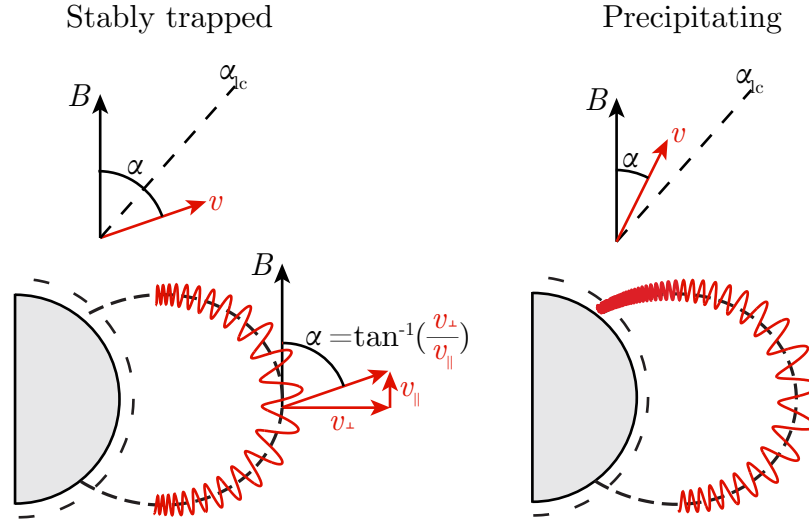


Figure 1.5: Schematic illustrating the pitch angle, α , and how it relates to both magnetic field and particle velocity vectors. Two cases are shown: stably trapped and precipitating particles.

whose mirror altitude is at or below 100 km is highly likely to be lost. In Figure 1.5, this critical angle is labeled as α_{lc} , and particles whose equatorial pitch angles are greater than this value are considered to be stably trapped, whereas particles whose pitch angles are below this value are considered to be precipitating.

Figure 1.6 shows a plot of the surface magnetic field strength as a function of latitude and longitude around the globe. If the geomagnetic field were a perfect dipole, these isointensity lines of magnetic field strength would be horizontal, and the loss cone angle would be the same at all longitudes. However, the actual magnetic field strength varies as a function of longitude, with a minimum occurring in the southern Atlantic Ocean. This region is known as the South Atlantic Anomaly (SAA), and this asymmetry results in two distinct loss cones for particle precipitation.

At any particular longitude, there exists an equatorial pitch angle below which a particle is destined to precipitate during its bounce motion. This condition defines a bounce loss cone. The lifetime of electrons in the bounce loss cone is typically on the order of seconds, so no stable population in the bounce loss cone can exist. Recall that in addition to gyrating about the magnetic field, and bouncing between

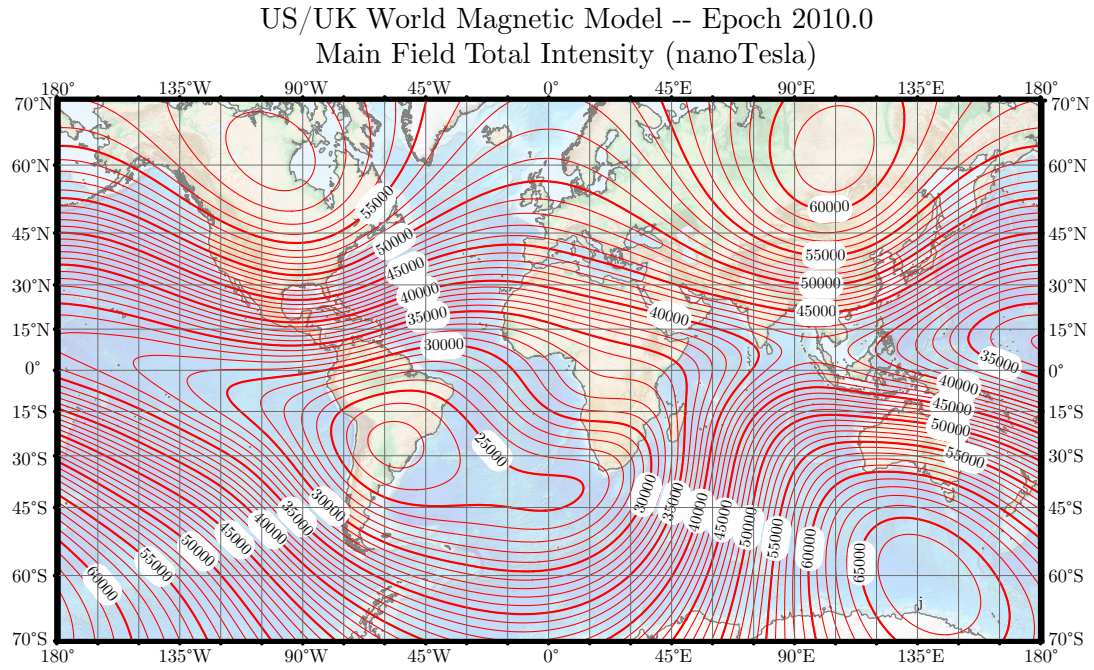


Figure 1.6: Isointensity lines of geomagnetic field strength around the globe. Map developed by NOAA/NGDC and CIRES (<http://ngdc.noaa.gov/geomag/WMM/>).

hemispheres, charged particles also undergo a charge dependent drift, eastward in the case of electrons, and that the mirror point is a function of the magnetic field strength, and thus longitude. The asymmetry of the geomagnetic field results in the formation of the so-called drift loss cone.

The drift loss cone angle is a function of L -shell, and is defined as the maximum bounce loss cone angle over all longitudes, as shown in Figure 1.7. Plotted in the lower left are the equatorial pitch angles of particles at the edge of the bounce loss cone as a function of longitude. These values are calculated using the IGRF-10 model of the Earth's magnetic field, assuming no external current systems (valid for L -shells $< \sim 4$), and assuming that a particle whose mirror altitude is at, or below, 100 km is likely to collide with a neutral particle in the Earth's atmosphere, and be precipitated. The values shown in Figure 1.7 are calculated for an L -shell of 2 in 2008. Because the Earth's static magnetic field changes very slowly over time, numerical values of loss cone pitch angles in other years are very similar.

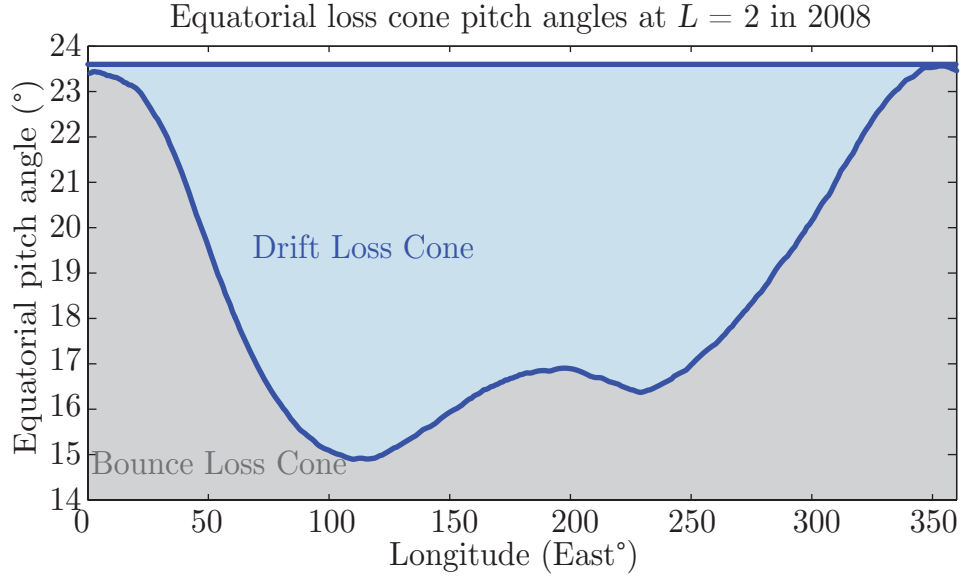


Figure 1.7: Equatorial pitch angle as a function of longitude describing both the drift and bounce loss cone angles. In this example, these values were calculated in 2008 at $L=2$.

Locally any particle whose equatorial pitch angle falls below the lower line in Figure 1.7 is lost in seconds. Consider, however, a particle at $\sim 100^\circ$ East longitude whose equatorial pitch angle is 23° . At this longitude, the pitch angle of that particle is above the bounce loss cone, but as the particle drifts eastward, it will drop below the bounce loss cone line and be lost at $\sim 340^\circ$ East. Thus the drift loss cone consists of particles that precipitate upon reaching longitudes of the South Atlantic Anomaly, and these fluxes persist on the order of hours for a few hundred keV, making drift loss cone fluxes easy to measure over long time scales. We revisit this concept in Section 3.2.2 when making measurements of drift loss cone fluxes at low Earth orbit.

1.3 Review of Past Work

One means of removing energetic electrons from their otherwise stably trapped orbits is through wave-particle interactions with electromagnetic whistler waves originating from lightning discharges on the Earth. The physical mechanisms of this process are

further explored in Chapter 2. A complete review of the relevant literature is outside the scope of this study. We choose instead to highlight the history of wave-particle interactions, focusing on studies related specifically to lightning-generated whistler waves.

As mentioned in Section 1.2.3, *Dungey* [1963] was the first to suggest that whistler waves originating from lightning discharges may be responsible for the loss of radiation belt particles through wave-particle interactions. *Kennel and Petschek* [1966] studied the role of incoherent whistler mode waves generated by the electrons, while *Lyons et al.* [1972] also investigated the effect of such waves (also called plasmaspheric hiss) on trapped electrons. Measurements since then have shown that whistler waves from lightning often represent the dominant wave energy in the 1–25 kHz range (e.g., [*Gurnett and Inan*, 1988]) and that individual whistlers can cause significant precipitation. A comparative theoretical study of pitch angle scattering by waves from different sources [*Abel and Thorne*, 1998a,b] concluded that lightning-produced waves significantly affect trapped energetic electrons, especially at $1.5 < L < 2.5$ and for energies between 100–300 keV.

At relativistic energies (> 1 MeV), pitch angle diffusion of radiation belt electrons via cyclotron resonant interaction with plasmaspheric hiss is thought to be the dominant loss mechanism [*Lyons et al.*, 1972; *Lyons and Thorne*, 1973; *Imhof et al.*, 1986]. Recently, *Green et al.* [2005] examined three years of plasma wave observations from the Dynamics Explorer and the Imager for Magnetopause-to-Aurora Global Exploration (IMAGE) spacecraft and concluded that lightning was a very likely source of plasmaspheric hiss which, through wave-particle interactions, maintains the slot region in the radiation belts. Objections to this conclusion were raised by *Thorne et al.* [2006], although the main point of dispute concerned the source of the low frequency (< 500 Hz) portion of the plasmaspheric hiss which contributes to the relativistic (> 1 MeV) losses. *Meredith et al.* [2006] studied CRRES wave data together with the global distribution of lightning to also test the origins of plasmaspheric hiss and found lightning-generated whistler waves to be the dominant contributor to wave

frequencies above 2 kHz. These findings suggest that lightning-generated whistlers affect the lower energy electrons in the slot region whereas the loss of relativistic electrons is attributed to natural plasma turbulence (as opposed to lightning).

While the significance of whistler waves in the process of lightning-induced electron precipitation (LEP) events was recognized early, the spatial extent of LEP events was determined more recently. Formerly, LEP events were thought to be produced only by ducted whistlers. Ducted whistler waves are only able to propagate in magnetic field-aligned ducts of enhanced ionization, and affect a relatively small region of the electron belt (< 400 km horizontal extent at the geomagnetic equator) [Burgess and Inan, 1990]. However, uncertainties in the number and size of ducts made it difficult to estimate the global consequences of the LEP phenomenon [Voss *et al.*, 1998]. The first recognition of the spatial extent of LEP regions resulted from a juxtaposition of theoretical prediction [Lauben *et al.*, 1999] and experimental observation [Johnson *et al.*, 1999], demonstrating that LEP events are also produced by non-ducted whistlers launched by lightning. Special magnetic field conditions need not exist for these waves to be present. This discovery suggests that the LEP process occurs much more commonly than previously believed, with each lightning flash able to precipitate particles over an ionospheric region of ~ 2000 km in lateral extent at ~ 100 km altitude, thus affecting a correspondingly large region of the radiation belts.

On the ground, evidence of LEP has been observed via subionospheric remote sensing of very low frequency (VLF) signals propagating in the Earth-ionosphere waveguide to detect perturbations in the upper atmosphere associated with lightning-induced electron precipitation. Early work focused on ducted LEP events [e.g., Inan *et al.*, 1985, 1988, 1990; Burgess, 1993], while later work confirmed precipitation over larger spatial extent, consistent with non-ducted precipitation [e.g., Johnson *et al.*, 1999; Clilverd *et al.*, 2004; Peter and Inan, 2004]. Thousands of observations of these kinds exist, but they are generally limited by the location of the VLF receivers, and most studies have been restricted to short case studies.

Lightning-induced electron precipitation can also be measured in space. The first satellite measurements of LEP events were provided by the Stimulated Emissions of Energetic Particles (SEEP) investigation on the S81-1 spacecraft [*Voss et al., 1984*]. SEEP observed short bursts of electrons in the bounce loss cone and found a one-to-one correlation between these measurements of precipitating electrons and ground-based measurements of lightning-generated whistler waves. However, SEEP measurements of these transient events could not reveal the global event rate or their spatial extent, and the altitude of the satellite was too low to allow sufficient sampling of enhanced LEP fluxes in the drift loss cone.

The next set of significant satellite observations comes from the Solar Anomalous and Magnetospheric Particle Explorer (SAMPEX) satellite. With its relatively low (~ 600 km) altitude, SAMPEX is well-placed to observe electrons freshly scattered into the drift loss cone during their eastward drift toward the South Atlantic Magnetic Anomaly (SAA). The advantages of observing electrons in the drift loss cone are that all such electrons must necessarily have been recently scattered into the drift loss cone, and that there are no stably trapped particles to obscure the new arrivals by causing background counts in the instruments. Analyses of energetic (> 150 keV) electron fluxes in the drift loss cone showed hundreds of cases of newly enhanced drift loss cone fluxes associated with individual thunderstorms [*Blake et al., 2001*]. These data indicated that thunderstorms around the world may continually precipitate energetic electrons from the radiation belts, but the solid state detector upon which these measurements were based did not operate long enough to allow a significant statistical analysis of drift loss cone fluxes. The SAMPEX satellite continues to provide energetic electron flux data for electrons with energies > 500 keV and > 1 MeV, but these energies tend to be higher than expected resonances with lightning generated whistler waves, as discussed in Section 2.3. Investigation of years of data by the present author found no clear evidence of lightning-induced electron precipitation on these higher energy channels.

More recently, the DEMETER satellite was launched in a low-altitude orbit similar to SAMPEX. Initial observations indicated short bursts of lightning-induced electron precipitation coincident with in-situ observations of the upgoing whistler wave [*Inan et al.*, 2007]. These cases represent bounce-loss cone observations during which the LEP bursts occur within <1 s of the causative lightning strike. There exist only a handful of such events, as they are transient by nature and require temporal and spatial coincidence of the satellite pass over the exact region of precipitation. However, a three-year analysis of drift loss cone fluxes on DEMETER demonstrated a seasonal association with lightning, indicating that LEP is a significant contributor to the loss of slot region electrons [*Gemelos et al.*, 2009]. Further exploration of drift loss cone flux enhancements associated with lightning is presented in Chapters 4 and 5 of this dissertation.

1.4 Thesis Organization

The present work is organized into six chapters:

Chapter 1 (the current chapter) introduces the magnetosphere, the Van Allen radiation belts, and the concept of the drift loss cone. This chapter also provides the context of the drift and bounce loss cones in terms of radiation belt research, and reviews previous work related to the present research.

In Chapter 2 we introduce lightning-induced electron precipitation (LEP) as one mechanism for removing radiation belt electrons from their otherwise stably trapped orbits. An analysis of previous means of measuring precipitated electrons is presented, and expected energy and time dependencies are explored.

In Chapter 3 we describe the instruments used to make observations of both lightning and electron precipitation, namely the DEMETER satellite and the National Lightning Detection Network. We also submit the United States as an ideal location for making drift loss cone observations of LEP events.

In Chapter 4 we present a detailed analysis of the seasonal characteristics of both lightning and energetic electron precipitation, indicating that lightning is indeed a significant contributor to radiation belt losses on a global scale. We also explore how these relationships vary from day to night, with L -shell, and over many years of data.

In Chapter 5 we further explore the relationship between lightning and electron precipitation by using a physical model to calculate the relative amount of flux we expect to see at the satellite's location, and comparing these expected flux values to the fluxes measured on the DEMETER satellite.

Chapter 6 summarizes the results presented in Chapters 3 to 5, and concludes with a discussion of future extensions to this work, as well as possibilities of making these measurements under geomagnetically active conditions.

1.5 Scientific Contributions

The major contributions of this research may be summarized as follows:

1. Discovered a seasonal variation in electron precipitation at mid-latitudes consistent with lightning as a major loss driver for electrons with energies of a few hundred keV.
2. Identified the continental United States as the best geographic region for measurements of lightning-induced electron precipitation at low Earth orbit.
3. Quantified the relationship between electron precipitation and lightning activity, including the dependence on energy and L -shell.

Chapter 2

Lightning-induced Electron Precipitation

2.1 Introduction

Lightning discharges are well-known sources of electromagnetic radiation in the frequency range of a few Hz up to many MHz (typical peak at 5–10 kHz [[Rakov and Uman, 2003](#), p. 6]). A fraction of this electromagnetic radiation reaches the radiation belts, interacts through cyclotron resonance with energetic electrons therein, and precipitates them from their otherwise stably trapped orbits. In this section, we explore this process in further detail and present methods with which lightning-induced electron precipitation (LEP) can be detected.

2.2 Wave-particle Interactions

Lightning is pervasive around the Earth, with an average of 45 lightning flashes occurring around the globe every second [[Christian et al., 2003](#)]. A terrestrial lightning discharge emits a broadband spectrum of electromagnetic waves with frequencies ranging from a few Hz up to many MHz. Electromagnetic waves originating from lightning discharges propagate away from the lightning flash and through the Earth-ionosphere waveguide. If the Earth's ionosphere were a perfect conductor, the electromagnetic wave energy would remain trapped in the confines of the Earth-ionosphere waveguide. However, the presence of the geomagnetic field allows a

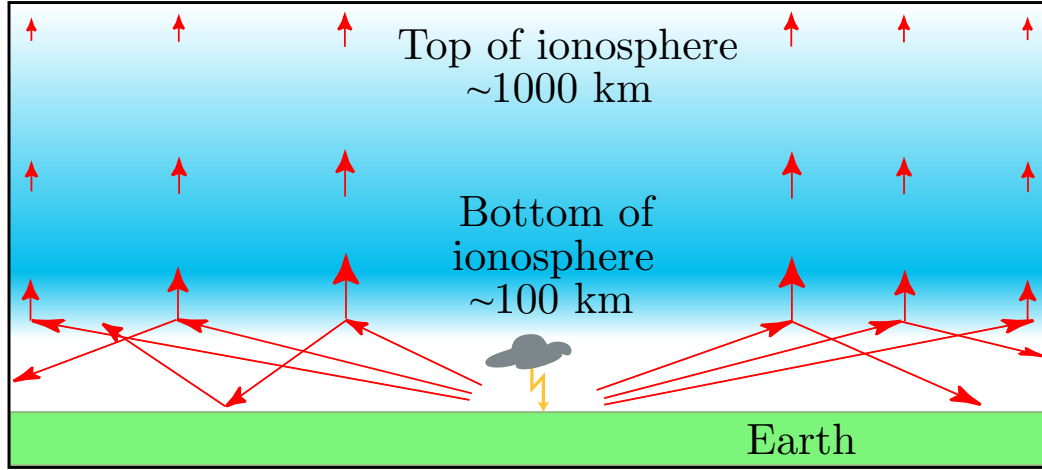


Figure 2.1: Cartoon demonstrating the propagation of a lightning-generated electromagnetic wave away from the source lightning, a portion of which leaks through the Earth-ionosphere waveguide and couples into the magnetosphere.

portion of this wave energy to leak through the highest ionized regions of the Earth's atmosphere (Figure 2.1) where it excites a so-called whistler-mode wave which propagates obliquely through the magnetosphere. The whistler-mode wave energy travels along ray trajectories away from the Earth, being guided by gradients in the Earth's magnetic field strength and direction, as well as by gradients in electron number density. A fraction of the trapped energetic electrons resonate with the whistler wave (under certain conditions), resulting in pitch-angle scattering of the electrons. If the pitch angle of the electrons is sufficiently decreased via cyclotron resonant interaction with the whistler-wave field, the lowered mirror height of the electrons may lie in the dense upper atmosphere and the electron may thus very likely be lost from the radiation belts. This four-step process of wave generation, wave propagation, gyroresonance pitch-angle scattering, and electron precipitation is illustrated in Figure 2.2.

During resonance, the electron and the whistler wave exchange momentum, and the electron momentum is redirected by the wave magnetic field, causing a deflection in pitch angle that can be cumulative over a time period during which this condition holds. Repeated interaction can cause pitch angle scattering of electrons, sometimes

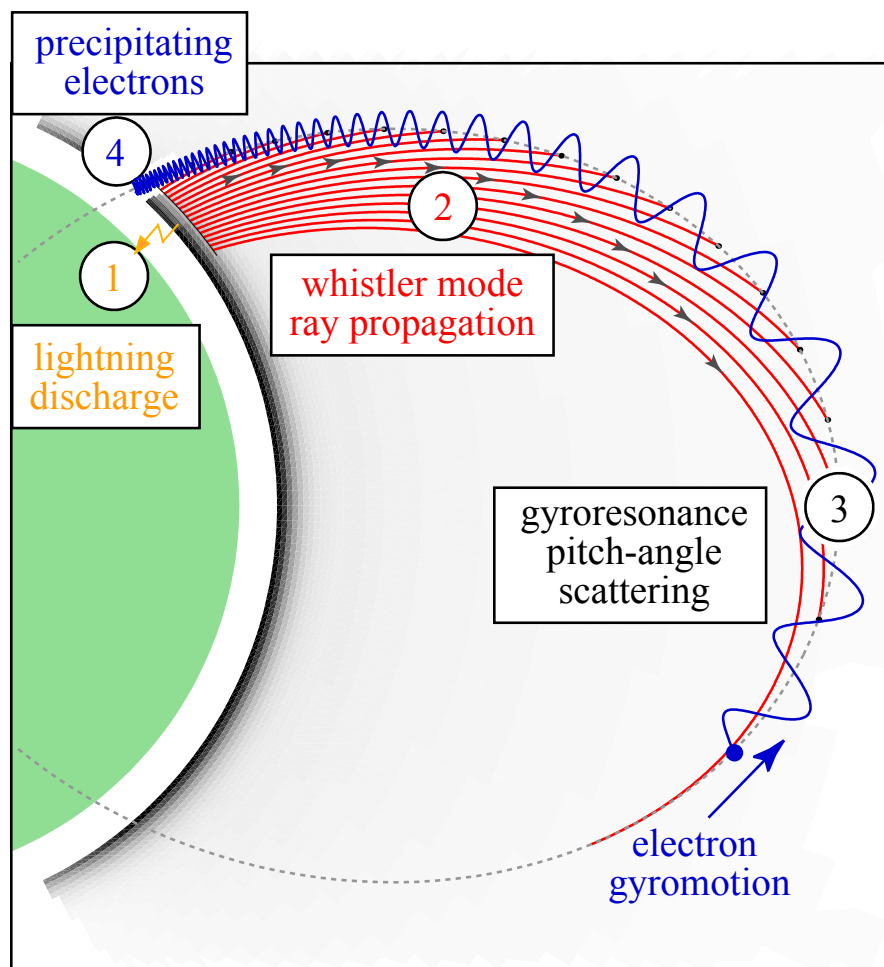


Figure 2.2: Illustration of the lightning-induced electron precipitation process. 1. Lightning discharge emits a broadband electromagnetic wave. 2. A portion of this wave energy propagates obliquely through the magnetosphere. 3. Electrons encounter the wave field and experience gyroresonance pitch-angle scattering. 4. Electrons precipitate into the dense upper atmosphere.

by as much as 1° [Inan *et al.*, 1989], and can move electrons just above the loss cone edge into the loss cone. If the pitch angle is sufficiently lowered into either the bounce or drift loss cones, the electron is lost from the radiation belts.

2.3 Resonant Energy Calculations

Interaction of charged particles with an external electromagnetic wave field such as a whistler wave is described by the Lorentz force equation. In the case of an external wave field, the Lorentz force equation (1.5) is modified to include the presence of magnetic (\mathbf{B}^w) and electric (\mathbf{E}^w) fields due to an electromagnetic wave as follows:

$$\frac{d\mathbf{p}}{dt} = q_e \{ \mathbf{v} \times [\mathbf{B}^w + \mathbf{B}_0(\mathbf{r})] + \mathbf{E}^w \} \quad (2.1)$$

At each point $C = (L, \lambda)$ along the field line, we establish a local Cartesian coordinate system as shown in Figure 2.3a with $\hat{\mathbf{z}} \parallel \mathbf{B}_0$ and $\hat{\mathbf{x}}$ pointing towards higher L -shells, providing a reference frame for the electron helix and wave field components. Following the methods of Bell [1984], we use this reference frame to provide expressions for the various field components in (2.1) as:

$$\mathbf{E}^w = -\hat{\mathbf{x}}E_x^w \sin \Phi + \hat{\mathbf{y}}E_y^w \cos \Phi - \hat{\mathbf{z}}E_z^w \sin \Phi \quad (2.2)$$

$$\mathbf{B}^w = \hat{\mathbf{x}}B_x^w \cos \Phi + \hat{\mathbf{y}}B_y^w \sin \Phi - \hat{\mathbf{z}}B_z^w \cos \Phi \quad (2.3)$$

where $\Phi(\mathbf{r}) = \int \omega dt - \int \mathbf{k} \cdot d\mathbf{r}$ is the wave phase, \mathbf{k} is the wave vector, and \mathbf{r} is the position vector along the ray path. We assume that locally the Earth's magnetic field \mathbf{B}_0 is directed along the positive z -axis of our coordinate system. Because the gyroradius of the resonant energetic particles is generally small at the L -shells of interest, we additionally assume that $\mathbf{B}_{0z}(x, y, z) = \mathbf{B}_{0z}(0, 0, z) \equiv \mathbf{B}_0(z)$.

Inserting \mathbf{B}_0 , (2.2), and (2.3) into (2.1), we obtain the detailed equations of motion of an energetic electron in an obliquely propagating whistler-mode wave field. However, the dynamics of the resonant interaction are such that cumulative changes in

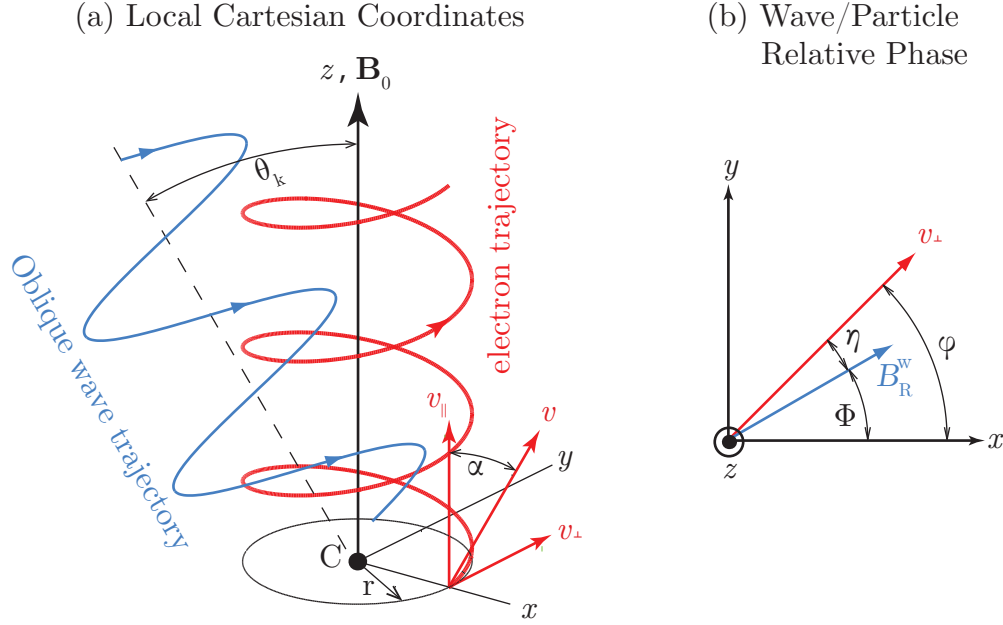


Figure 2.3: (a) Energetic electron helix in local Cartesian coordinate frame in which the elliptically polarized wave fields are applied. (b) Interaction geometry between an energetic electron and an obliquely propagating whistler wave showing the gyro-averaged angle η between v_{\perp} and the right-hand circularly polarized wave magnetic field vector \mathbf{B}_R^w at wave phase Φ . Figure modified from *Lauben et al. [2001]*.

the pitch angle of the particle occur over time scales much greater than the gyroperiod. Thus, it is useful to cast the equations of motion in a gyro-averaged form such that rapid fluctuations occurring on the time scale of a gyroperiod are averaged out.

The whistler wave magnetic field is naturally elliptically polarized in the cold magnetospheric plasma. It is convenient to decompose the wave magnetic field into two circularly polarized components with opposite senses of rotation, i.e.,

$$\begin{aligned} \mathbf{B}_R^w &= \frac{B_x^w + B_y^w}{2} [\hat{\mathbf{x}} \cos \Phi + \hat{\mathbf{y}} \sin \Phi] \\ \mathbf{B}_L^w &= \frac{B_x^w - B_y^w}{2} [\hat{\mathbf{x}} \cos \Phi - \hat{\mathbf{y}} \sin \Phi] \end{aligned} \quad (2.4)$$

Using the above decomposition together with (2.1) and averaging over a gyroperiod, we obtain the gyro-averaged equations of motion for a general harmonic resonance m [Bell, 1984]. The full solution to this complicated set of equations is beyond the scope

of this work. However, [Bell \[1984\]](#) also put forth the resonance condition relating the angle η (shown in Figure 2.3b) between the whistler wave magnetic field (\mathbf{B}_R^w) and v_\perp . The resonance condition holds that for any appreciable change in electron momentum to occur, η must remain relatively constant over some portion of the integration space. For the non-relativistic case the resonance condition can be expressed as:

$$\frac{d\eta}{dt} = m\omega_H - \omega - k_z v_z \simeq 0 \quad (2.5)$$

where $\omega_H = qB/m_e$ is the electron gyrofrequency in the electron rest frame, $q = 1.602 \times 10^{-19}$ C, $m_e = 9.11 \times 10^{-31}$ kg is the electron rest mass, B is the geomagnetic field strength, v_z is the electron velocity along the magnetic field vector, ω is the instantaneous whistler wave radial frequency, and k_z is the portion of the wave magnetic field along the magnetic field vector.

Figure 2.4 depicts the resonance for the simplified case of wave propagation parallel to the static magnetic field. An electron gyrating about the magnetic field line and moving in one direction encounters an electromagnetic wave traveling in the opposite direction. Looking into the opposite direction to B_0 , the sense of the electron gyration is counter-clockwise, and, with respect to a stationary observer, the sense of wave field rotation is also counter-clockwise. The physical meaning of (2.5) is that resonance occurs when the Doppler-shifted wave frequency as experienced by the electron is matched to the electron gyrofrequency (or an integer multiple thereof).

Using the resonance condition along with typical wave parameters in the inner magnetosphere, we compute the energies of resonantly interacting electrons as a function of wave frequency and L -shell. In these calculations, electron number density along the geomagnetic equator is calculated by assuming the cold electrons to be in a state of diffusive equilibrium along any particular field line [[Angerami and Thomas, 1964](#)] and to vary smoothly throughout the magnetosphere. Figure 2.5 shows the assumed equatorial electron density profile that is modeled after [Carpenter and Anderson \[1992\]](#) who used in-situ measurements from the ISEE 1 satellite in

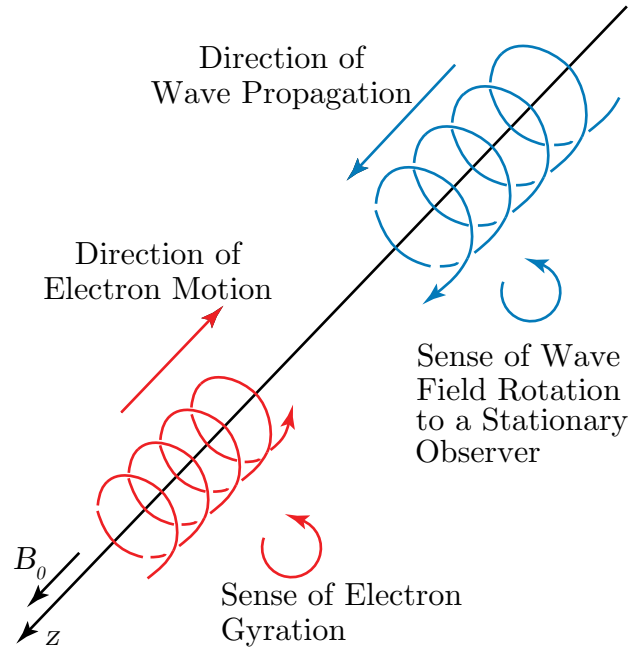


Figure 2.4: An electron gyrating about the magnetic field line in one direction encounters an electromagnetic wave traveling in the opposite direction.

conjunction with whistler data to develop an empirical model of equatorial electron density.

Figure 2.6 shows cyclotron resonant electron energies computed as a function of L -shell at a variety of wave frequencies typical of lightning-generated whistler waves, with a wave normal angle $\theta = 80^\circ$ (oblique propagation), and for particles just above the edge of the loss cone. General behavior of note is that the resonant energy of particles increases with decreasing wave frequency and decreases with L -shell (for regions of $L < 4$, or within the plasmasphere). From this plot, it is evident that within the slot region cyclotron resonance with whistler waves is unlikely for electrons with energies much greater than a few hundred keV or above $L = 3$, except at the lowest wave frequencies.

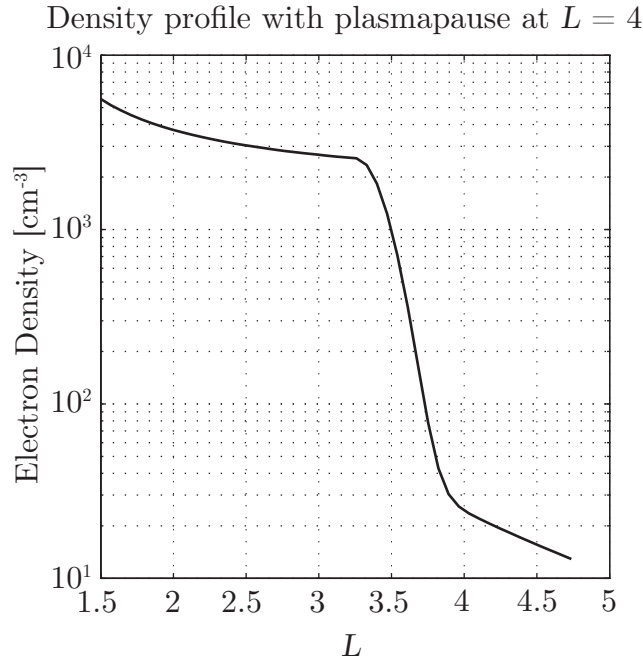


Figure 2.5: Assumed plasmaspheric density profile as a function of L -shell with the plasmopause located at $L = 4$.

2.4 Methods of Detection

Precipitation of electrons from the radiation belts is typically measured in one of two ways. The first method of detection is done via remote sensing of changes in ionospheric conductivity due to impingement of energetic particles on the upper atmosphere. The second method involves in-situ particle detectors oriented such that the pitch angle of at least some of the observed particles is within the loss cone.

2.4.1 Ground-based Observations

On the ground, evidence of lightning-induced electron precipitation, or LEP, has been observed via very low frequency (VLF) remote sensing of Navy transmitter signals. VLF radio waves ($\sim 3\text{--}30$ kHz) are guided by the spherical waveguide formed between the Earth's surface and the lower ionosphere (the so-called Earth-ionosphere waveguide), and they can propagate long distances with great efficiency. The

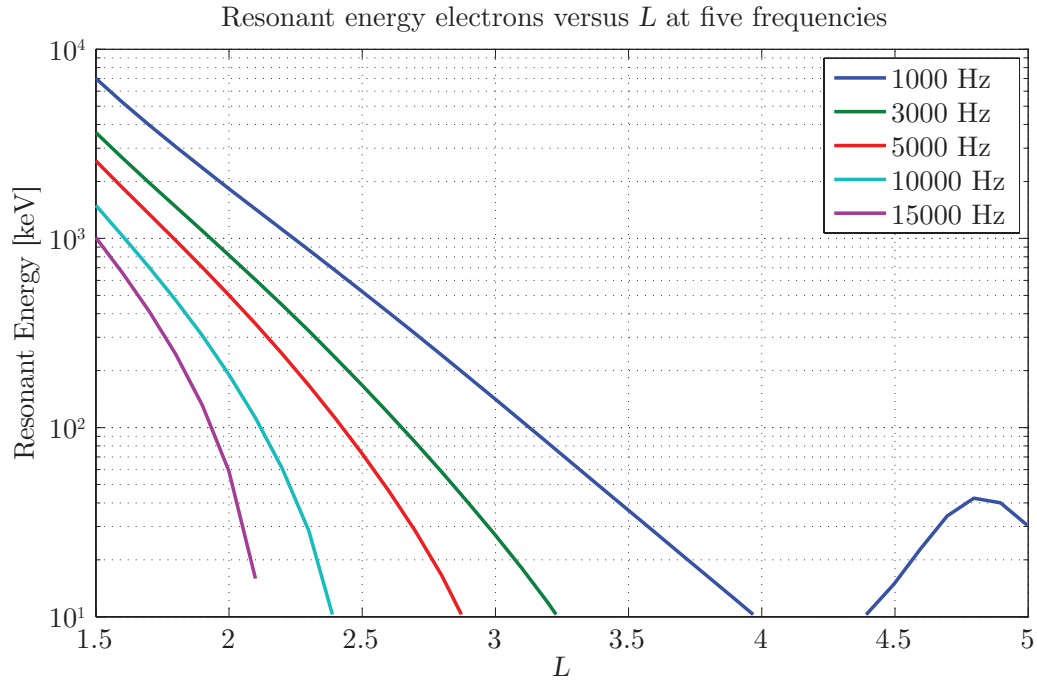


Figure 2.6: Calculated resonant energies of electrons with whistler waves of various frequencies typical of lightning as a function of L -shell.

amplitude and phase of the received signal is sensitive to the electrical conductivity of the waveguide along the path of travel. Hence, these signals are sensitive not only to changes in ground conductivity, but also to changes in ionospheric conductivity.

Precipitating electrons impinging on the upper atmosphere deposit energy into the atmosphere that, through secondary ionization, changes the electron density and electrical conductivity of the lower ionosphere (Figure 2.7). This ionospheric density enhancement perturbs VLF waves propagating through, or near, the disturbance. Remote sensing of the amplitude and phase of VLF signals can thus be used to measure spatial and temporal characteristics of localized disturbances in the ionosphere. Together with lightning data, this remote sensing technique has been used extensively to map the occurrence rate and spatial extent [*Peter and Inan, 2004*, and references therein] of lightning-induced electron precipitation events. However, these types of remote observations are spatially limited by the locations of the receivers, and

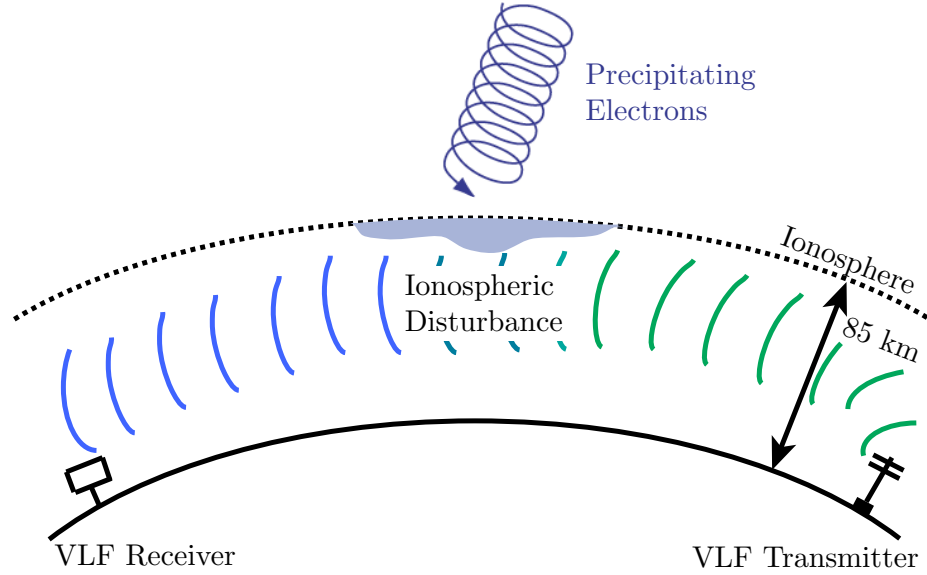


Figure 2.7: Cartoon illustrating how precipitating electrons on the upper atmosphere create an ionospheric disturbance that changes the conductivity of the Earth-ionosphere waveguide.

most studies to date consider only short time periods or case studies [e.g., *Johnson and Inan*, 2000; *Peter and Inan*, 2004, 2007].

2.4.2 In-situ Observations

We can also observe direct effects of lightning-induced electron precipitation in space. This type of observation typically relies on data from solid state electron spectrometers mounted on low Earth orbiting satellites [e.g., *Voss et al.*, 1984; *Inan et al.*, 2007]. However, in-situ measurements of LEP have also been reported using rocket data [e.g., *Rycroft*, 1973; *Goldberg et al.*, 1986]. Most of the recorded events involve short bursts of electrons into the bounce loss cone, often directly associated with a causative lightning strike [e.g., *Voss et al.*, 1984, Figure 1]. This type of measurement requires coincidence of the satellite directly over the precipitation region at the time of a thunderstorm. As a result, in-situ measurements of LEP into the bounce loss cone are not as common as ground-based measurements.

In addition to bounce loss cone measurements, drift loss cone measurements of LEP in situ are also possible. These types of measurements exploit the fact that low altitude satellites spend a majority of their orbit below the stable trapping region for charged particles. Measurements of electrons in the drift loss cone have been going on for decades [*Vernov et al.*, 1965], but association of drift loss cone fluxes with lightning has only recently been reported [*Blake et al.*, 2001; *Gemelos et al.*, 2009]. These observations require knowledge and location of thunderstorm activity, either via ground-based lightning location networks (e.g., the National Lightning Detection Network [*Cummins et al.*, 1998]), or in-situ optical imagers (e.g., the Lightning Imaging Sensor [*Christian et al.*, 1999]) in addition to the energetic particle data. Drift loss cone measurements of lightning-induced electron precipitation allow an extension of transient and localized observations of LEP to a global assessment of the role of lightning in the lifetime of radiation belt electrons. This concept is further explored in Chapters 4 and 5.

Chapter 3

Description of Available Data

3.1 Introduction

This chapter introduces the instruments used to make observations of both lightning and electron precipitation. We also discuss an ideal location for making drift loss cone observations of LEP events and present seasonal variations of lightning and electromagnetic wave activity.

3.2 DEMETER Satellite

The DEMETER satellite is a French micro-satellite that was launched in June 2004 to study ionospheric disturbances and the Earth’s electromagnetic environment. On-board instruments include electric and magnetic field sensors, a plasma analyzer, a Langmuir probe, and a particle detector [*Lagoutte et al., 2006*]. DEMETER is in a 670 km altitude, quasi heliosynchronous circular orbit with an inclination of $\sim 98.23^\circ$. The satellite orbits 14 times per day, and is always located near 10:30 or 22:30 local time [*Parrot et al., 2006*]. Figure 3.1 shows an example of the orbital ground track of the satellite over one day. Orbits for other days follow a similar progression.

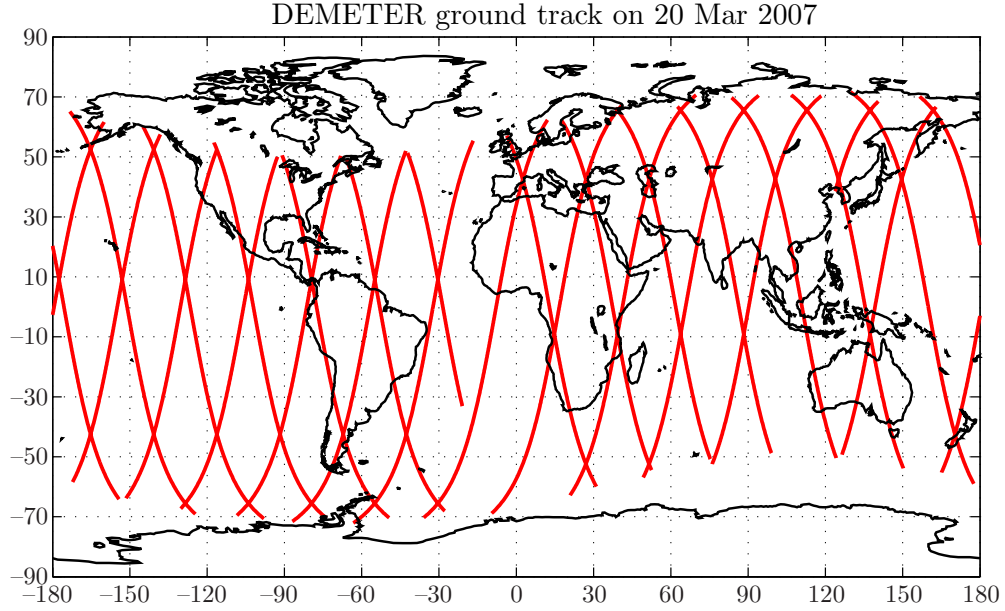


Figure 3.1: Orbital ground track of DEMETER, shown on 20 March 2007. Ground tracks are shown for invariant latitudes $< 65^\circ$. When the satellite progresses through the auroral regions, most instruments are systematically switched off [Sauvaud *et al.*, 2006]. Only regions for which scientific data are recorded are shown in this figure.

3.2.1 Detector Details

We use wave data from the Instrument Champ Electrique (ICE) which provides measurements of the power spectrum of the electric field in the very low frequency (VLF) range (15 Hz – 17.4 kHz) [Berthelier *et al.*, 2006]. We also use data from the Instrument Detecteur de Plasma (IDP), measuring energetic electron fluxes in the energy range from 72.9 keV to 2.35 MeV with a 4 second time resolution and a 17.8 keV energy resolution. The IDP has a large geometric factor of $1.2 \text{ cm}^2 \text{ sr}$, with a view angle of $\pm 16^\circ$ [Sauvaud *et al.*, 2006]. The detector looks perpendicularly to the orbital plane, resulting in a detection of particles with local pitch angles near 90° .

Sample data from both the ICE and IDP instruments are shown in Figure 3.2. These data show an example of an LEP burst seen on DEMETER when the satellite was passing over Europe [Inan *et al.*, 2007, Figure 2]. The top panel shows the ICE electric field plotted as a function of frequency and time in a spectrogram format. Near

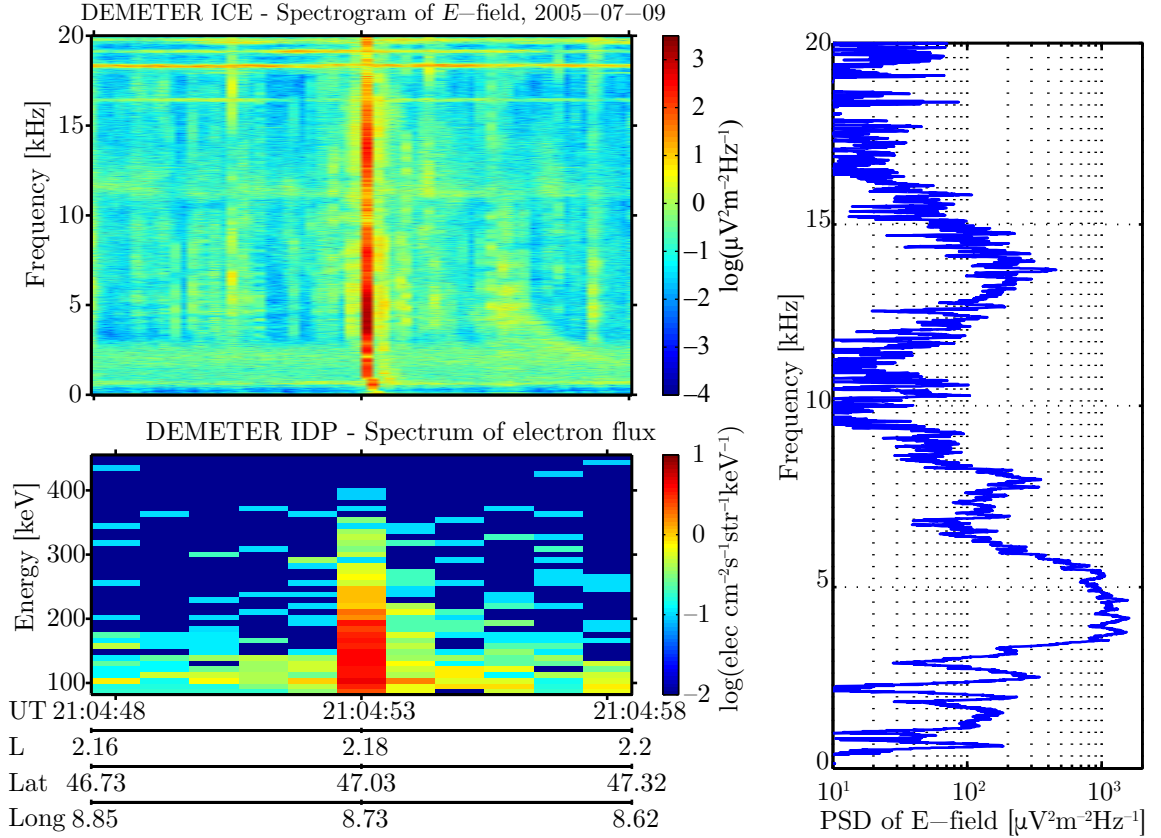


Figure 3.2: Example of LEP bursts on DEMETER. Top panel shows a spectrogram of the electric field from ICE on DEMETER showing a 0^+ whistler wave at 21:04:53. Bottom panel shows electron spectra from IDP on DEMETER showing bursts of precipitated electrons. Right panel shows the power spectral density of the 0^+ whistler (top panel) as a function of frequency.

the center of the panel, the strong broadband burst of wave energy in the electric field is evidence of an upgoing 0^+ whistler wave injected by a nearby lightning discharge. This whistler wave presumably led to a precipitation of electrons, as shown in the lower panel of IDP spectra, plotted as a function of energy and time. The panel on the right shows the power spectral density (PSD) of the whistler wave as a function of frequency, demonstrating a peak energy in the 3–7 kHz range that is typical of whistler waves recorded on the DEMETER satellite.

3.2.2 Drift Loss Cone Sampling

The IDP detector observes electrons with local pitch angles near 85° . These electrons are mirroring at or near the satellite altitude. Because of the low satellite altitude and the detector orientation, over a majority of its orbit DEMETER views drift loss cone particles. Recall from Section 1.2.4 that, using the first adiabatic invariant, the pitch angle $\alpha(s)$ at any point s with field $B(s)$ along a field line can be expressed in terms of the equatorial values of magnetic field strength and pitch angle (B_{eq} and α_{eq}) by the relationship:

$$\sin \alpha(s) = \sqrt{\frac{B(s)}{B_{\text{eq}}}} \sin \alpha_{\text{eq}} \quad (3.1)$$

Figure 1.7 illustrated the variation of the equatorial pitch angle (α_{eq}) as a function of longitude along the $L=2$ drift shell. From this figure we determined that the drift loss cone encompasses all equatorial pitch angles below $\sim 23.5^\circ$. An equatorial pitch angle of $\alpha_{\text{eq}} = 23.5^\circ$ corresponds to a magnetic field value $B(s) = 0.24$ G. Any electron that mirrors at $B = 0.24$ G sits at the edge of the drift loss cone; any electron that mirrors at $B > 0.24$ G falls below the edge of the drift loss cone and is lost.

Figure 3.3 shows the altitude of the $B = 0.24$ G mirror points along the $L = 2$ drift shell. The blue line represents mirror altitudes in the Northern Hemisphere, the red line represents mirror altitudes in the Southern Hemisphere, and the dashed black line represents the DEMETER altitude of 670 km. The implications of this plot are that, for most of its orbit, DEMETER observes electrons destined to precipitate in

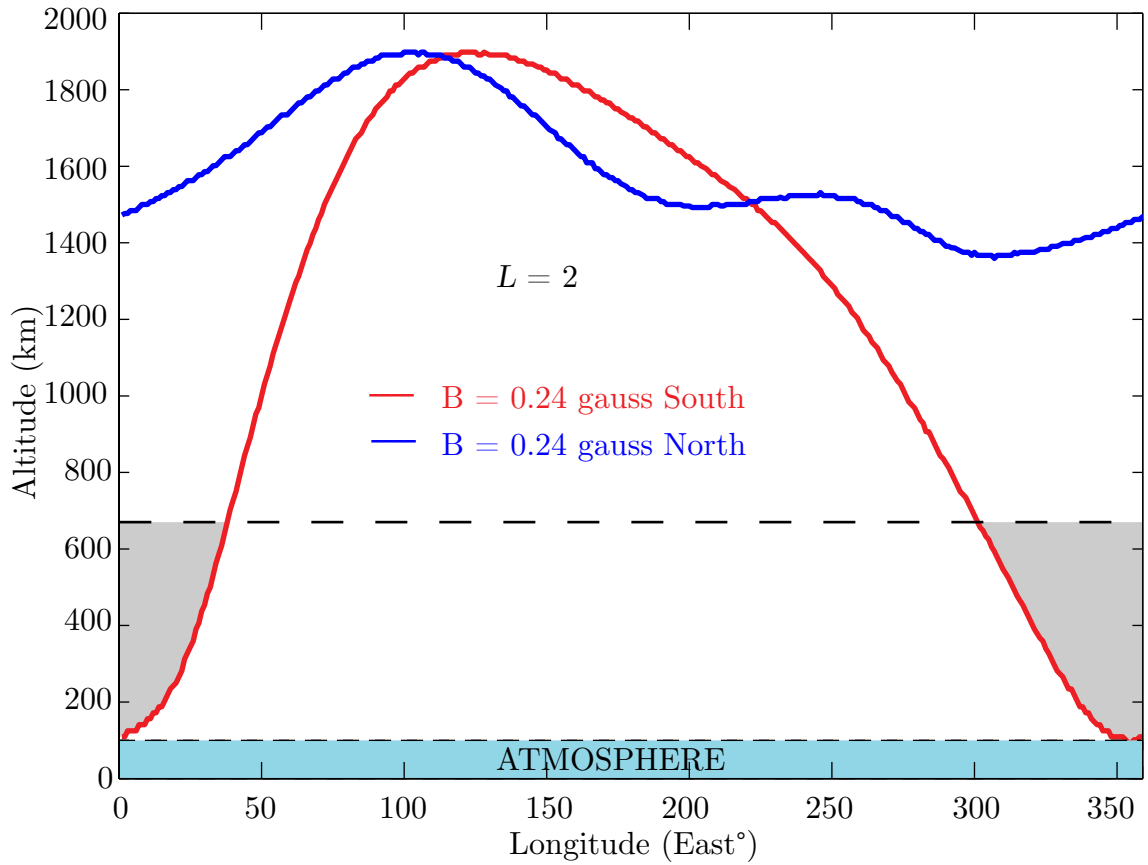


Figure 3.3: Altitude of the $B=0.24$ G mirror points as a function of longitude for both the Northern and Southern Hemispheres. Data points were calculated using the IGRF-10 model of the Earth’s magnetic field in 2008 for $L=2$. Note that the mirror point falls to 100 km in the Southern Hemisphere over the South Atlantic Anomaly.

the region of the South Atlantic Anomaly. Only at longitudes where the locus of $B = 0.24$ G falls below the dashed line does DEMETER see trapped particles. No stably trapped electrons are observed in the Northern Hemisphere. In the Southern Hemisphere, drift loss cone particles are observed between the longitudes of 37° E and 307° E.

From Figure 3.3 it is clear that for the majority of its orbits, DEMETER detects particles deep within the drift loss cone which are locally mirroring near the altitude of DEMETER (670 km) while drifting eastward. It takes a few hours for low energy (100–300 keV) electrons to drift through this region. What is observed on DEMETER at a given longitude is the superposition of all electrons in the drift loss cone that

have undergone multiple scattering events at locations west of the satellite position. In the following chapters, we explore the extent to which multiple scattering events from lightning discharges contribute to these drift loss cone fluxes.

3.3 NLDN

Comparison of drift loss cone fluxes with lightning data is done using data from the U.S. National Lightning Detection Network (NLDN). NLDN consists of a network of high frequency sensors around the United States that instantaneously detects the electromagnetic signals given off when lightning strikes the Earth’s surface [Cummins *et al.*, 1998]. Among the information recorded are flash location, current amplitude, polarity, and time with millisecond accuracy for cloud-to-ground (CG) flashes. One drawback of this system is its inability to detect intra-cloud (IC) flashes, which are thought to be the most common type of lightning flash [Rakov and Uman, 2003, p. 321]. However, IC discharges tend to have a lower peak current [Murphy and Cummins, 1998] and radiate a weaker field [Weidman *et al.*, 1981] than their CG counterparts. VLF whistler intensity from lightning is proportional to peak current [Reising *et al.*, 1996], and LEP flux is proportional to VLF amplitude [Inan and Carpenter, 1986]. Thus, while IC flashes are not detected within the NLDN network, their relative contribution to LEP may be comparable to or less than the contribution from CG flashes. Nevertheless, NLDN measurements of CG flash activity also provide an indication of IC flash activity since most storms have both types of flashes. Thus NLDN data are good indicators for us of general lightning activity.

3.4 Location for Observations

While we primarily utilize lightning data from NLDN over the U.S., it is important to first understand lightning activity on a global scale. The average distribution of lightning strikes worldwide has been measured by the Optical Transient Detector

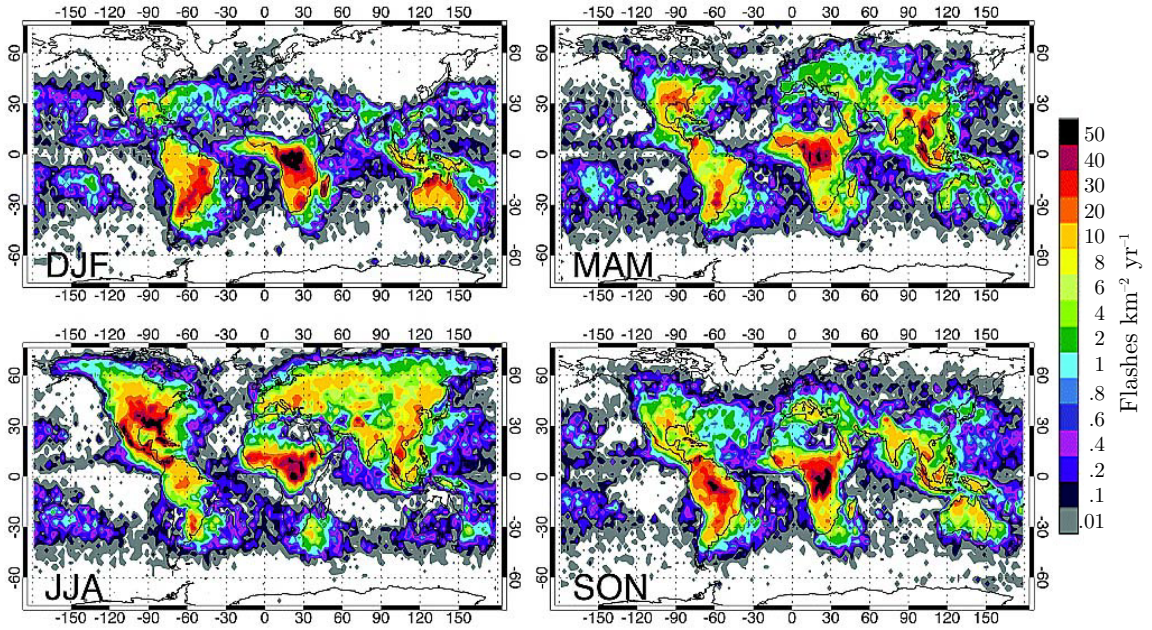


Figure 3.4: Annualized geographic distribution of lightning flash rate as a function of season from *Christian et al. [2003]*. (a) December, January, and February (DJF). (b) March, April, and May (MAM). (c) June, July, and August (JJA). (d) September, October, and November (SON).

(OTD) on board the MicroLab 1 satellite by *Christian et al. [2003]* and is shown in Figure 3.4. These plots show the annualized lightning flash rate averaged over 5 years, selected by season, and annualized in units of flashes per square kilometer per year. While flash density in the equatorial regions persists through all seasons, lightning at mid-latitudes is predominant in the local spring and summer months. For instance, virtually no lightning is observed in the Northern Hemisphere during the months of December, January, and February (local winter), whereas lightning activity in this region peaks during the local summer months of June, July, and August.

Continental regions see large seasonal variations in lightning flash density, whereas oceanic lightning remains fairly consistent during the entire year. In general lightning occurs mainly over landmasses, with a mean annual land to ocean flash ratio of 10:1 [*Christian et al., 2003*]. Furthermore, by dividing the globe into latitudinal sections, *Christian et al. [2003]* found that the maximum flash rate for the Northern Hemisphere

is significantly greater than the maximum flash rate for the Southern Hemisphere, and attributed this imbalance of the annual cycle to lightning activity in North America and northern Asia.

As discussed in Section 2.1, lightning discharges produce intense electromagnetic radiation, particularly in the 1–10 kHz range. Thus we expect to see a seasonal distribution of VLF wave intensity around the globe similar to that of lightning flash intensity, but modified by the ionospheric attenuation. Figure 3.5 shows average nighttime 5–10 kHz wave spectral intensity measured on the DEMETER ICE instrument in 1° by 1° latitude/longitude bins during August and December. As evidenced by these plots, wave spectral intensities over the United States dominate in the northern summer, whereas waves reaching 670 km are much less intense in the south even during southern summer (December). Waves observed in the Southern Hemisphere west of South America in August likely originate from U.S. lightning and propagate approximately along field lines to the Southern Hemisphere. This result is consistent with observations of an abundance of highly-dispersed whistlers in this region with the DEMETER on-board neural network [Parrot *et al.*, 2009] and with a lack of significant thunderstorm activity in this oceanic region [Christian *et al.*, 2003].

Because of this concentration of wave activity over the U.S., the continental United States is an ideal location for observing lightning-induced electron precipitation. Additionally, the region geomagnetically conjugate to the U.S. lies in the Pacific Ocean where there is very little lightning activity to obscure seasonal effects of LEP. Other regions of high lightning activity (e.g., the Amazon, central Africa, and southeast Asia) are too close to the geomagnetic equator—a region where whistler waves are virtually unknown. Whistler waves enter the ionosphere vertically. At low latitudes, the dip angle of the magnetic field is small. Vertically incident whistler waves in this region encounter large losses due to the strong dependence of the imaginary part of the refractive index (i.e., the loss or absorption rate) on the wave normal angle [Helliwell, 1965, p. 60]. While Figure 3.4 shows plenty of lightning activity in these

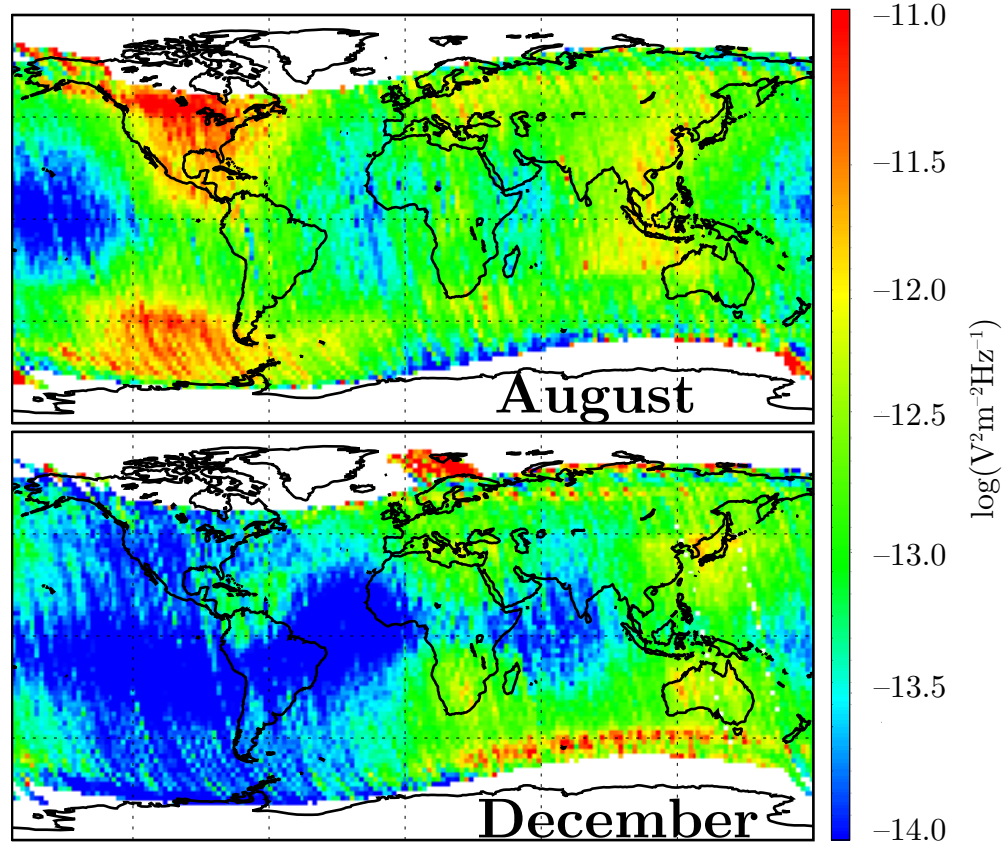


Figure 3.5: Global maps of the two year (2006–2007) monthly averages of nighttime wave spectral intensity ($\text{V}^2\text{m}^{-2}\text{Hz}^{-1}$) in the 5–10 kHz range in August and December.

near-equatorial regions, very little VLF wave power reaches the 670 km altitude of the DEMETER satellite, as seen in Figure 3.5.

Other regions in Figure 3.5 showing strong wave activity in the 5–10 kHz range are not of lightning origin. The thin, laterally extended region of wave activity below Africa and Australia is due to a minimum in plasmaspheric electron density in this region during December solstice [Clilverd *et al.*, 2007] which brings the lower hybrid frequency (and the associated quasi-electrostatic wave activity, not of lightning origin) into the 5–10 kHz range of the plot. The high wave intensities above Norway in December are produced by the EISCAT [Kimura *et al.*, 1994] radar experiments.

Chapter 4

Seasonal Variation of Electron Precipitation

4.1 Introduction

In this chapter we examine three years of electron flux data recorded on the DEMETER IDP instrument and compare this data with known seasonal effects from lightning. Over the United States, energetic electron fluxes in the slot region ($2 < L < 3$) are significantly higher in the northern summer than in the winter, consistent with the seasonal variation of lightning activity in the Northern Hemisphere. The increased precipitation of particles into the drift loss cone over the Northern Hemisphere in the summer is consistent with expected pitch-angle scattering by lightning-generated whistler waves, indicating that lightning is a significant contributor to the loss of slot region electrons. The results of this chapter are published in *Gemelos et al.* [2009].

4.2 Seasonal Variation of Drift Loss Cone Fluxes

To determine the relationship between lightning activity and drift loss cone fluxes on DEMETER, we begin by examining the seasonal variation of drift loss cone fluxes and comparing that to the seasonal variation of lightning. The previous chapter describes the occurrence of lightning and VLF wave activity on both a seasonal and a global scale. Of particular importance is that lightning occurs more frequently during the local summer months, and that VLF wave intensity from lightning

measured at 670 km altitude peaks over the continental United States. If lightning were a significant contributor to electron precipitation, we would expect to see a corresponding peak in drift loss cone fluxes on DEMETER during the local summer months, particularly over the continental United States.

Recall from Section 3.2.2 that the IDP detector on DEMETER primarily observes drift loss cone particles. As electrons drift eastward around the globe, an accumulation of electrons in the drift loss cone occurs. Upon reaching longitudes of the South Atlantic Anomaly, the mirror height of the electrons is sufficiently lowered towards the atmosphere that the electrons are lost from the radiation belts. What is observed on DEMETER at a given longitude is a superposition of all electrons that have been scattered into the drift loss cone at longitudes west of the satellite position. In situ evidence of individual electron precipitation events is thus limited to regions of low background counts—i.e., regions just to the east of the SAA [i.e., *Inan et al.*, 2007], or in regions conjugate to the SAA where electron populations exist for one bounce period before being scattered onto the atmosphere in the conjugate hemisphere.

Over the continental United States, an individual scattering event of electrons from just above the drift loss cone into the drift loss cone is not likely to be detected due to the high background accumulation of drift loss cone fluxes in this region. Thus, one needs to develop a large statistical database so that a particular trend, such as a seasonal variation, may appear above the background flux levels. For this reason, we explore three years of IDP electron data from 2006–2008. In the context of averaging three years of data, the transient and localized nature of the LEP phenomena introduces the danger of one or a few large events dominating the result. In such cases, it is preferable to use median (rather than mean) values which naturally minimize effects of outliers.

Figure 4.1a shows the logarithm of median monthly nighttime fluxes of 126 keV electrons in bins of 1° latitude by 1° longitude, for August and December of 2006–2008. Only nighttime data are considered because trans-ionospheric absorption of VLF wave power is significantly higher during the day [*Helliwell*, 1965, p. 71]. The

energy of 126 keV is within the observed range of ~ 100 –250 keV for other recorded LEP events [Voss *et al.*, 1984, 1998; Inan *et al.*, 2007], and is chosen as a representative example of data within this observed energy range. Data for other energies in this range exhibit similar behavior, and the energy dependence of the seasonal variation is further explored in Section 4.3.

Figure 4.1b shows median nighttime fluxes in the region geomagnetically conjugate to the United States. Black dots along the coastline in the Northern Hemisphere correspond to black dots in the Southern Hemisphere which illustrate the geomagnetic conjugate points. For instance, between -100° and -80° longitude, the conjugate outline of Florida is visible. L -shell contours for $L=2$ and $L=3$ are overlaid on these plots as white lines. The solid portion of the L -shell contour denotes regions where DEMETER observes drift loss cone particles. The dashed white lines in panel (a) correspond to regions where DEMETER observes bounce loss cone particles.

Figure 4.1c shows the number of nighttime lightning strokes per month, weighted by the magnitude of the peak current in each stroke and divided into 1° by 1° latitude/longitude bins, as detected by the National Lightning Detection Network (NLDN) in August and December 2006–2008. Substantially higher lightning activity in August is accompanied by notably higher fluxes of drift loss cone electrons in both hemispheres, while lower lightning activity in December is accompanied by lower fluxes. The largest difference is over the central United States, where the lightning activity is the most intense and widespread. The termination of electron flux near the eastern boundary of the continental U.S. is due to the South Atlantic Anomaly which causes the mirroring points in the Southern Hemisphere to fall below 100 km. Even though lightning activity extends beyond the coast, DEMETER observes only transient fluxes in this region. Increased fluxes are, however, apparent in the geomagnetic conjugate region which is accessible to drift loss cone electrons.

Increased electron precipitation during summer months is also consistent with the seasonal distribution of VLF wave amplitudes observed on DEMETER, as was seen in Figure 3.5. While these marked seasonal characteristics of drift loss cone fluxes

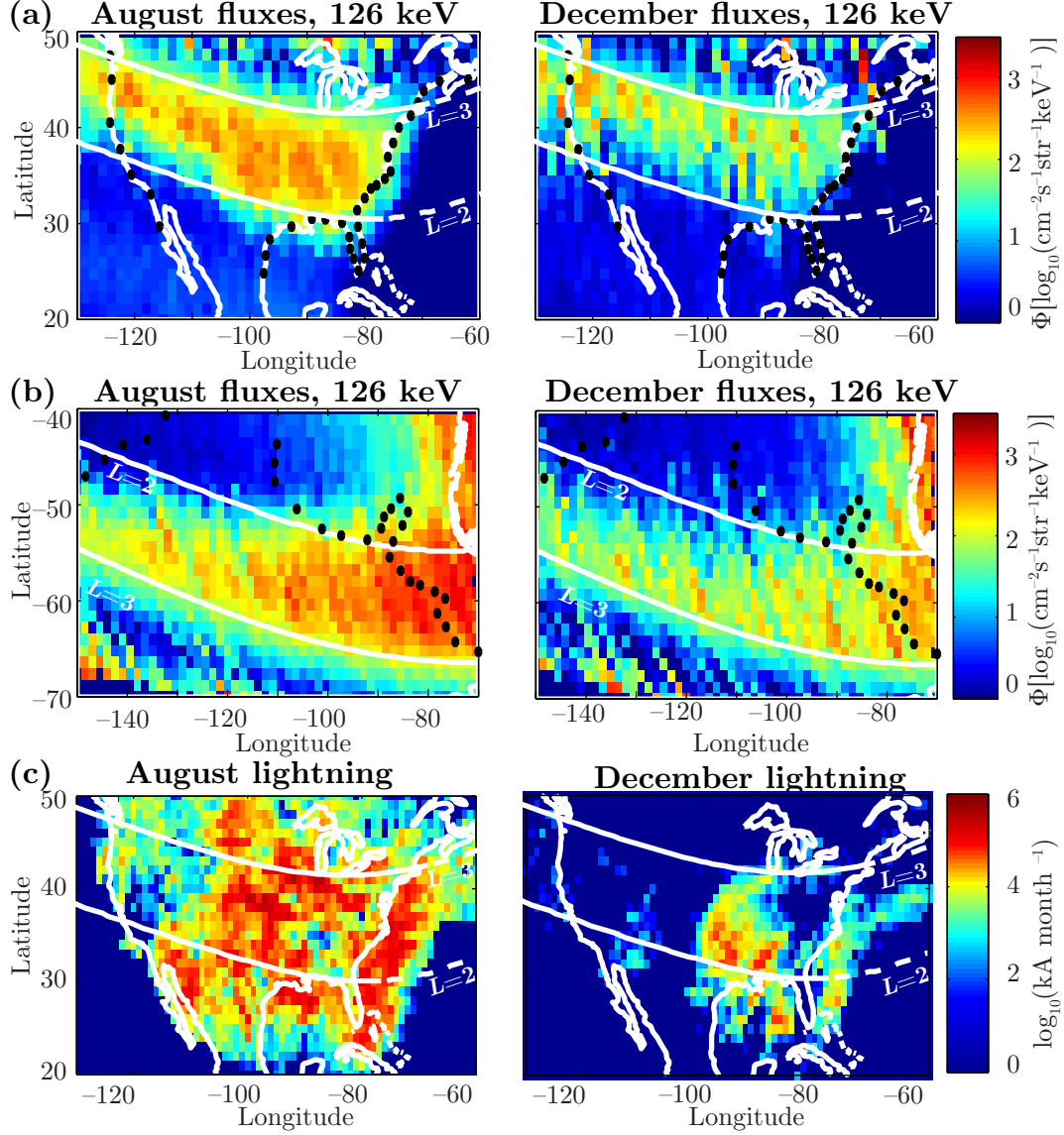


Figure 4.1: Seasonal variation of drift loss cone fluxes and lightning. (a) Median monthly nighttime 126 keV fluxes in 1° by 1° latitude/longitude bins over the U.S. for August and December 2006–2008. L -shell contours at satellite altitude are shown for reference. (b) Median nighttime 126 keV fluxes in conjugate region, denoted by black dots corresponding to U.S. coast. (c) Total nighttime lightning flash intensity in 1° by 1° latitude/longitude bins for August and December 2006–2008.

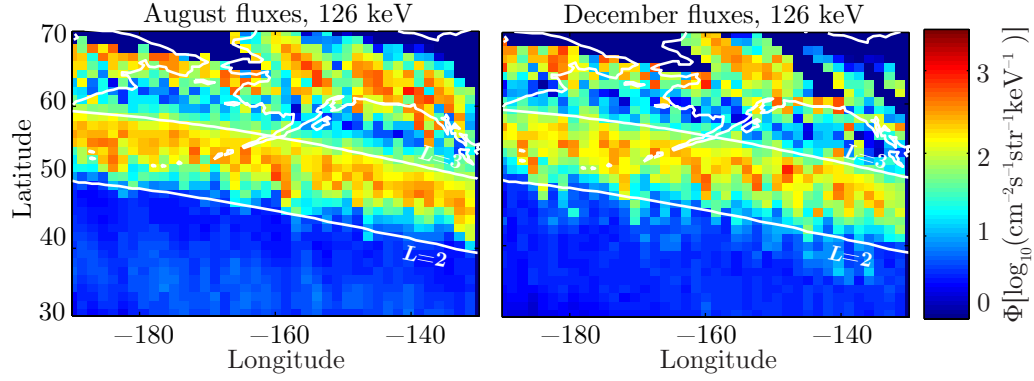


Figure 4.2: Median monthly nighttime 126 keV fluxes in 1° by 1° latitude/longitude bins over the Pacific Ocean for August and December 2006–2008. L -shell contours at satellite altitude are shown for reference.

are readily apparent over the United States, very little seasonal variation can be seen in the regions immediately to the west of the United States. Figure 4.2 shows the median nighttime 126 keV flux values over the Pacific Ocean in August and December. Figure 4.1 covers longitudes between -130° and -60° . Figure 4.2 covers longitudes between 170° and -130° , or an immediate westward extension of the region shown in Figure 4.1. The white contours represent $L=2$ and $L=3$, while the white lines in the upper left corners outline the northeastern edge of the Russian Chukchi Peninsula and the white lines in the upper right represent Alaska. The lack of significant seasonal variation over the Pacific region confirms that the United States is indeed an ideal location for drift loss cone flux measurements, as postulated in Section 3.4.

4.3 Energy and L -shell Dependencies

The precipitation map shown in Figure 4.1 implies a preference for electron precipitation to occur in the slot region ($2 < L < 3$), predominantly over the central and eastern United States (-100° to -80° longitude) where lightning is the strongest. The occurrence of precipitation predominantly over the slot region is consistent with

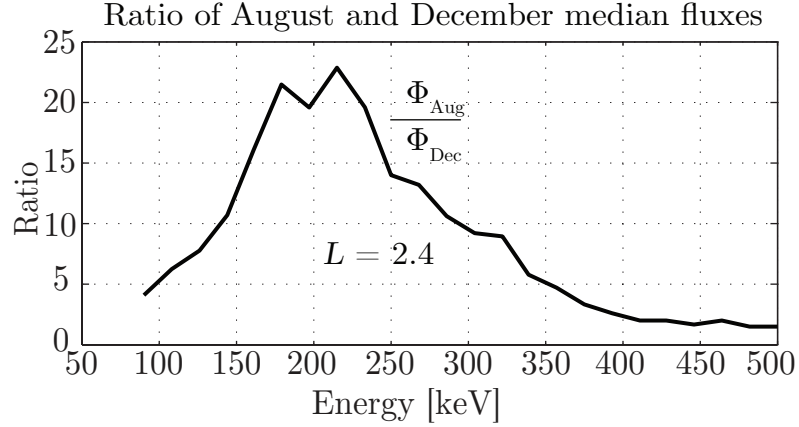


Figure 4.3: Ratio of median nighttime flux values in August and December 2006–2008, centered at $L=2.4$ and $-100^\circ < \text{longitude} < -80^\circ$.

resonant energy calculations shown in Figure 2.6. Lower energy electrons (~ 100 – 350 keV) can resonate with the full frequency spectrum of a typical lightning-generated whistler wave within the slot region, whereas above $L = 3$, cyclotron resonance with electrons of energies > 100 keV is unlikely. Figure 4.3 shows the ratio of August and December median nighttime flux values in 2006–2008 as a function of energy at $L=2.4$ over the central and eastern United States (-100° to -80° longitude). The largest seasonal differences occur for electrons with energies between 100–350 keV, as might be predicted by the theoretical resonant energy calculations of Figure 2.6.

Figure 4.4 shows the monthly median flux values for 126 keV electrons as a function of L -shell in August and December over the same longitude region ($-100^\circ < \text{longitude} < -80^\circ$) and three year time period (2006–2008) as the previous plot. It is clear that August fluxes in the slot region are significantly higher than those of December, demonstrating that a strong seasonal variation manifests in the slot region, whereas in the outer belt ($L > 4$) the seasonal differences are negligible. Based on the characteristics of median flux with both energy and L -shell, we conclude that most of the 100–300 keV drift loss cone electron fluxes in the slot region are maintained by cyclotron resonant interactions with whistler waves originating in lightning discharges.

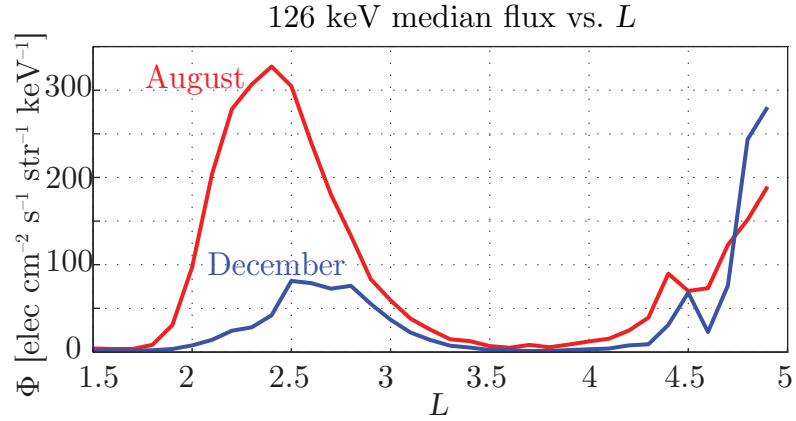


Figure 4.4: Median 126 keV nighttime fluxes as a function of L -shell in August and December 2006–2008.

4.4 Day/Night Effect

In the preceding sections, nighttime flux values were presented. The reason for this restriction is two-fold. First, lightning is more prevalent in the early afternoon and evening hours than it is during the morning. Since DEMETER measures electron fluxes at local times of approximately 10:30 and 22:30, there are statistically fewer storms during the daytime pass. Additionally, the ionospheric absorption of whistler waves is much higher during the daytime than at night, with typical relative losses of wave power (with respect to the nighttime equivalent wave power) on the order of 10–30 dB, depending on frequency [Helliwell, 1965, p. 71]. Nonetheless, a small but distinct seasonal difference between August and December daytime fluxes does exist in the DEMETER IDP data.

Figure 4.5 shows the ratio of median daytime flux values in August and December as a function of energy. These data were averaged over three years (2006–2008) and centered at an L -shell of 2.4. The median fluxes during the daytime from energies of ~ 100 –250 keV show that precipitation during August (summer) is almost five times higher than precipitation during December (winter). Similarly, the variation of 126 keV fluxes with L , plotted in Figure 4.6, shows that slot region fluxes in the

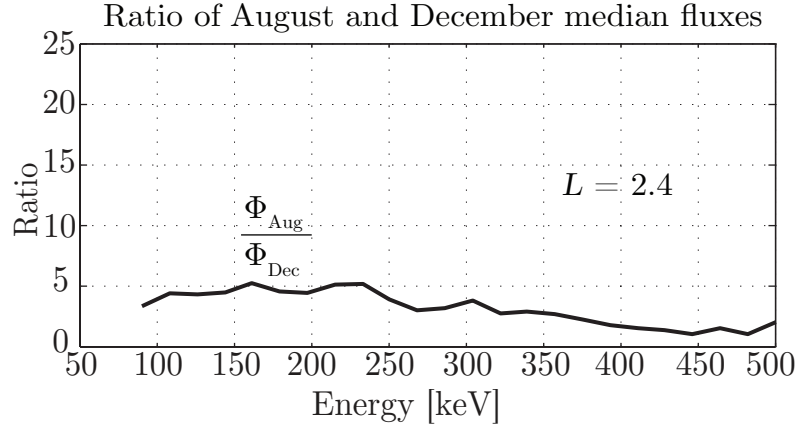


Figure 4.5: Ratio of median daytime flux values in August and December 2006–2008, centered at $L=2.4$ and $-100^\circ < \text{longitude} < -80^\circ$.

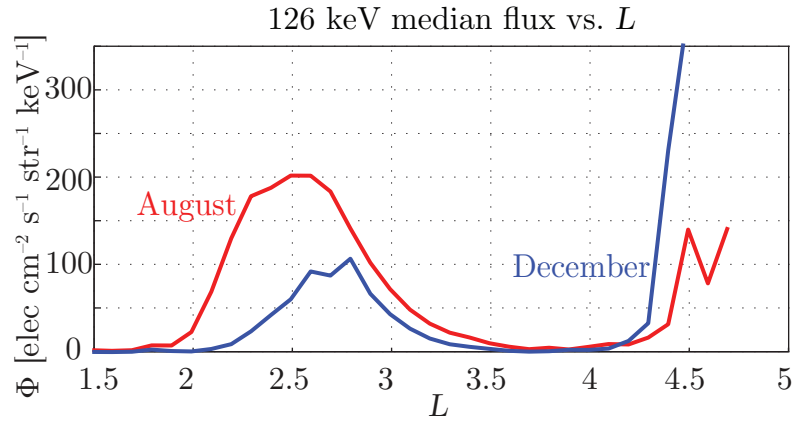


Figure 4.6: Median 126 keV daytime fluxes as a function of L -shell in August and December 2006–2008.

summer are still higher than those in the winter, but the difference is not as great as the one shown in Figure 4.4.

Of note when comparing Figures 4.4 and 4.6 is that the median flux values in December hardly vary between daytime and nighttime passes, whereas the median values in August are over fifty percent higher during the night than during the day. This discrepancy between electron fluxes recorded during the daytime and nighttime passes, particularly in the summer months when lightning is the most

intense and widespread, confirms that lightning is continually affecting the trapped particle populations, even during the daytime when ionospheric absorption of the whistler wave power is high. However, for the purposes of this dissertation, the effects of lightning-induced electron precipitation are more clearly viewed during the local nighttime hours. Thus, only nighttime measurements are considered in the remainder of this work.

4.5 Yearly Variation of Fluxes and Lightning

Full seasonal variation of both lightning and electron fluxes can be seen more clearly in Figure 4.7. The top panel shows median 126 keV electron fluxes averaged over five days (blue) and one month (red). These fluxes are median values spanning $2 < L < 3$ and $-100^\circ < \text{longitude} < -80^\circ$, i.e., the region of most concentrated lightning activity in Figure 4.1c. The bottom panel of Figure 4.7 shows lightning activity over the U.S. throughout the year in five-day and monthly averages. A broad peak in electron flux is clearly evident during the summer months of April–September, coincident with high lightning activity. In Figure 4.1, August and December were chosen as representative months for summer and winter because they represent the most and least intense months of lightning activity respectively. Each of the summer months shows a similar geographic distribution of electron flux and lightning to that shown in Figure 4.1.

Based on the characteristics of median flux with both energy and L -shell, we conclude that most of the drift loss cone electron flux in the slot region is maintained by cyclotron-resonant interactions with whistler waves originating in lightning discharges. To confirm this relationship, we formulate daily numbers for drift loss cone fluxes at 126 keV consisting of the summation of fluxes over nighttime passes in a region bounded by L -shells of 2 and 3, and longitudes of -100° to -80° , divided by the number of passes each day in this region. The daily lightning numbers are set equal to the number of flashes per day, weighted by the magnitude of the peak

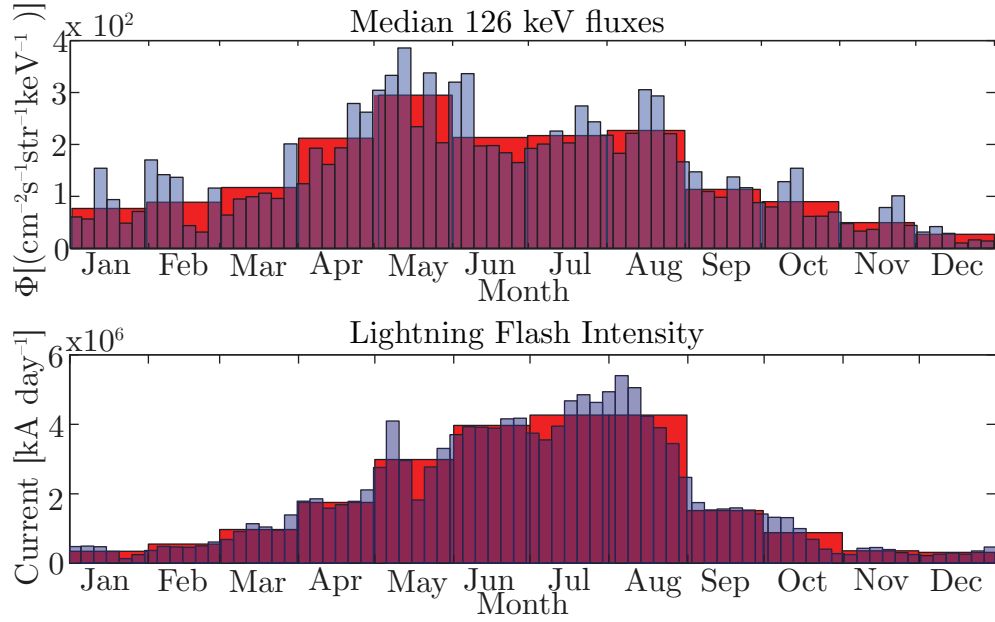


Figure 4.7: Yearly variation of fluxes and lightning. (Top) Five-day (blue) and one month (red) median nighttime 126keV flux values over 2006–2008. (Bottom) Average nighttime lightning flash intensity, shown in both five-day (blue) and one-month (red) sliding windows across 2006–2008.

current of each flash occurring within two hours of 22:30 LT, the approximate local time of DEMETER passes. Using these two sets of values in 2006–2008, we find the Spearman rank correlation coefficient, ρ , to be 0.42 with a p -value of 10^{-3} , implying a significant correlation [Berkson, 1942] between lightning and drift loss cone electron fluxes.

In the above calculation, we used the Spearman rank correlation as a non-parametric measurement of statistical dependence. This type of correlation assesses how well an arbitrary monotonic function describes the relationship between two variables without making any assumptions about the frequency distribution of the two variables. The Spearman rank correlation differs slightly from the more standard Pearson product-moment correlation in that the Pearson method assumes the behavior of the data follows a well-behaved probability distribution, such as a Gaussian distribution with a known mean and variance. A non-parametric measurement like the Spearman rank correlation is more robust to outliers [Devlin

et al., 1975], such as a single day with particularly high fluxes or a large number of thunderstorms, and lends itself well to large data sets of the sorts used within this dissertation.

Although the correlation of 0.42 is significant, the coefficient suggests that U.S. lightning is not responsible for all precipitation in the slot region. Scattering takes place elsewhere and from other causes (i.e., hiss, chorus, etc.), but the role of lightning is important. Chapter 5 further explores the causative relationship between lightning and energetic electron precipitation by using a physical model to calculate the relative amount of flux we expect to see at the satellite's location, and comparing these values to the fluxes measured on the DEMETER satellite.

Chapter 5

Assessing the Physical Connection between Lightning and Electron Fluxes

5.1 Introduction

The previous chapters describe how electromagnetic whistler waves from lightning can precipitate electrons from the radiation belts through resonant wave-particle interactions. Chapter 3 demonstrates why the United States is an ideal location for observing electron precipitation into the drift loss cone and introduces the DEMETER satellite and the National Lightning Detection Network (NLDN). Chapter 4 shows a clear seasonal variation of electron fluxes sampled by DEMETER in the drift loss cone over the United States consistent with the seasonal variation of U.S. lightning. In this chapter we utilize a physical model of lightning-induced electron precipitation to estimate the expected flux (on a normalized basis to compare different days and times with one another) at the satellite location due to lightning observed on the ground by NLDN. These values are then compared to the observed fluxes (again on a normalized basis) measured on the DEMETER satellite to determine the relative contribution of lightning over the United States to global drift loss cone fluxes.

5.2 Model of Lightning-induced Precipitation

The model of lightning-induced electron precipitation used in this chapter is based on a physical model introduced by *Lauben et al.* [2001] that calculates electron precipitation induced by obliquely propagating whistler waves generated by lightning discharges at specified locations. The following two subsections outline the methodology of the lightning-induced precipitation model implemented by *Lauben et al.* [2001]. This model is then used in Section 5.2.3 to determine a simplified two-dimensional Gaussian representation of the precipitation region estimated by the complete physical model summarized in Sections 5.2.1 and 5.2.2.

5.2.1 Whistler Wave Simulation

An oblique whistler wave field at any point is completely specified by the propagation delay with respect to the time of origin at the lightning flash t_g , the wave normal angle θ_k , and the wave power density S^w . In general these parameters vary with frequency and location throughout the magnetosphere and may be written as $t_g(\lambda, f, L)$, $\theta_k(\lambda, f, L)$, and $S^w(\lambda, f, L)$. As no closed form expression for these wave properties exists, a comprehensive VLF ray tracing methodology is used to determine these quantities.

The propagation of whistler-mode electromagnetic waves in the magnetosphere is determined largely by the geomagnetic field and the cold plasma density gradients. Here the geomagnetic field is taken to be dipolar. The cold background plasma is assumed to be in a state of diffusive equilibrium along any particular field line and to vary smoothly throughout the magnetosphere with a density profile similar to that shown in Figure 2.5. Ray paths are calculated using the Stanford VLF ray tracing program [*Inan and Bell, 1977*] over the first traverse through the magnetosphere, and ray tracings are repeated at 200 Hz spacing for frequencies $200 \text{ Hz} \leq f \leq 10 \text{ kHz}$. The bundles of ray paths are traced from the top side ionosphere throughout the magnetosphere, although for brevity, consideration is limited to the primary effect

induced by the first traverse of the whistler through the magnetosphere [*Lauben et al.*, 2001].

Wavefronts advance at the wave group velocity, and a set of ray/ L -shell intersection points are determined at which the group propagation time and wave normal angles are available directly. The wave power density, on the other hand, must be assessed from the combined effects of geometric ray-bundle defocusing and whistler-mode frequency-time dispersion determined by comparing rays launched at successive frequencies and incremental latitudes. The wave parameters t_g , θ_k , and S^w are then tabulated over frequency along L -shells in $\Delta L = 0.2$ over the range $1.8 < L < 4$ and afterward interpolated onto a finely spaced uniform latitude grid with $\Delta\lambda \leq 0.1^\circ$.

The whistler model described thus far assumes a normalized wave input power spectral density of $1 \text{ Wm}^{-2}\text{Hz}^{-1}$ at all ray injection points and for all frequencies. However, electromagnetic wave intensity radiated by a given lightning discharge exhibits a strong spatial and frequency dependence. In order to accurately determine the latitude/longitude extent of the magnetospheric region over which significant scattering and precipitation occurs, it is necessary to deploy a model of wave input power as a function of location, and for specified frequencies. These effects are accounted for in a lightning-magnetosphere illumination model.

Radiation at VLF frequencies is modeled using the discharge current profile [after *Cummer and Inan*, 1997]

$$I(t) = I_0(e^{-bt} - e^{-at}) \quad (5.1)$$

where a and b are discharge current parameters. Using the discharge current profile of (5.1), the time domain electric field at a distant point (R_l, ξ) is given by

$$\begin{aligned} E &= \mu_0 \frac{\sin \xi}{4\pi R_l} (2h_e) \left[\frac{dI}{dt} \right] \\ &= \mu_0 \frac{\sin \xi}{4\pi R_l} (2h_e I_0) [ae^{-at} - be^{-bt}] \end{aligned} \quad (5.2)$$

where R_l is the distance from the lightning source to the observation point, ξ is measured with respect to the local vertical, h_e is the height of the initial discharge

above the ground, and the brackets [] denote evaluation with time delay $t_0 = R_l/c$. The unbounded power spectral density of the cloud-to-ground lightning discharge is then given by

$$S(\omega) = \frac{1}{Z_0} \left(\frac{\mu_0 h_e I_0}{2\pi} \right)^2 \left(\frac{\sin \xi}{R_l} \right)^2 \frac{\omega^2 (a - b)^2}{(\omega^2 + a^2)(\omega^2 + b^2)} \quad (5.3)$$

where $Z_0 = 377 \, \Omega$ is the impedance of free space.

The lightning illumination model assumes discharge current parameters $a = 5 \times 10^3$ and $b = 1 \times 10^5$ to give an electromagnetic wave with a broadly-peaked frequency spectrum between $f = 2$ kHz and $f = 6$ kHz. Additionally, a stroke height $h_e = 5$ km and a reference current magnitude of $|I_0| = 10.53$ kA are assumed [Lauben *et al.*, 2001]. This lightning reference current magnitude is well within the range of typical peak current magnitudes recorded by NLDN over the United States.

In general, the cloud-to-ground lightning discharge radiates electromagnetic energy in all directions according to (5.3). In the whistler wave simulation model, wave input power for the ray tracing model is specified at a magnetospheric altitude of 1000 km. Because only a fraction of the radiated wave power is directed vertically, a factor of $\cos \xi$ is applied to (5.3) to conservatively estimate the available power flowing across the free-space/ionosphere boundary. Modifications to (5.3) are also made by accounting for ionospheric losses based on an assumed ionospheric electron density profile for ambient nighttime conditions [Lauben *et al.*, 2001, Plate 5]. After accounting for coupling and polarization loss (3 dB), the wave energy is taken to propagate vertically from $h = 100$ km to $h = 1000$ km where ray tracing begins, suffering additional absorption along the way after the frequency- and latitude-dependent loss profiles of Helliwell [1965, p. 71].

The lightning illumination model is evaluated for a set of lightning discharges at magnetic source latitudes $\lambda_s = 30^\circ$, 40° , and 50° and applied as input to the oblique whistler simulation model described above. Each lightning source leads to a maximum wave intensity for some point along the magnetic equator at an L -shell higher than

that of the source. Electron precipitation signatures are then determined through electron scattering calculations described below.

5.2.2 Electron Scattering Calculations

As the whistler wave propagates through the magnetic field, a distribution of counter-streaming electrons having pitch angles initially at the edge of the loss cone encounters the advancing wave packet. The test particles subsequently undergo gyroresonant pitch angle scattering at locations for which the resonance condition (2.5) holds. In general, roughly half the particles are scattered to larger pitch angles (outside the loss cone) and the remaining half to smaller pitch angles (inside the loss cone) [Lauben *et al.*, 2001]. An assumed ambient electron phase space density is then convolved with the full set of test particle deflections to determine the perturbed phase space density. Following the methods of Ristić-Djurović *et al.* [1998] and Chang and Inan [1985], the perturbed phase space density is then converted to an equivalent flux distribution and integrated over the loss cone to determine the precipitation flux signature at the foot of each L -shell as a function of electron energy.

The precipitation flux signature is then calculated for a fixed set of L -shells and longitude displacements to determine the extent and behavior of the two-dimensional precipitation footprints over extensive ionospheric regions. Finally the total precipitated energy flux is integrated over space and time for all particle energies > 100 keV to determine the total precipitated energy for lightning strikes at various source latitudes. The resultant precipitation hot spots occur in a broad region spanning several tens of degrees in latitude and longitude and develop at locations $\sim 7^\circ$ to $\sim 20^\circ$ poleward of the lightning discharge. Greater total precipitation energy is deposited when lightning occurs at the higher source latitudes of $\lambda_s = 40^\circ$ and 50° than at $\lambda_s = 30^\circ$. A graphical illustration of the precipitation fluence spatial density as well as the total precipitation energy flux can be seen in Figure 5.1. Note that the mapping from magnetic dipole coordinates to geographic coordinates has the effect of subtracting $\sim 11^\circ$ (the approximate dipole axis tilt) from the lightning magnetic

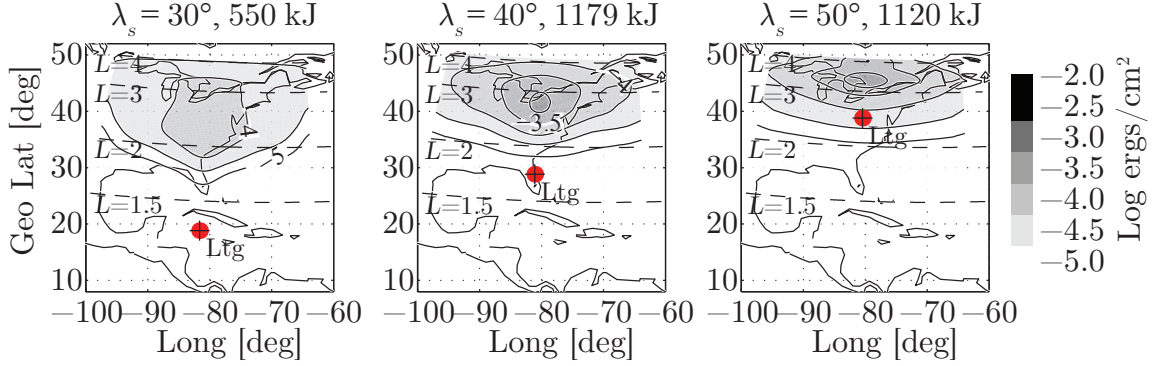


Figure 5.1: Precipitation energy spatial density of electrons with $E > 100$ keV, for lightning located at magnetic latitudes of $\lambda_s = 30^\circ$, 40° , and 50° (left to right). Figure modified from [Lauben et al. \[2001, Plate 12\]](#).

latitude for the chosen longitude ($\sim 80^\circ$ W). Thus a source at $\lambda_s = 30^\circ$ appears at a geographic latitude of $\sim 19^\circ$ [[Lauben et al., 2001](#)].

5.2.3 Gaussian Precipitation Model

Throughout the course of one year, approximately 79,000,000 lightning discharges occur over the continental United States. Since it is not possible to perform complicated ray tracing analyses and precipitation fluence calculations 79,000,000 times, we establish a simplified model of lightning-induced electron precipitation based on the model presented by [Lauben et al. \[2001\]](#). Using the precipitation fluence hot spots shown in Figure 5.1 as a reference, we develop a two-dimensional Gaussian model of electron precipitation patterns for lightning discharges with source latitudes between $30^\circ < \lambda_s < 50^\circ$. Our goal is to use this lightning-induced electron precipitation model to perform a forward estimation of the amount of precipitation flux one might expect to see at the satellite location given known lightning discharge occurrences over the United States.

The precipitation calculated by the lightning-induced electron precipitation model proposed by [Lauben et al. \[2001\]](#) is highly dependent on the near-loss-cone trapped radiation belt flux levels assumed. Our main objective is not to compare the model

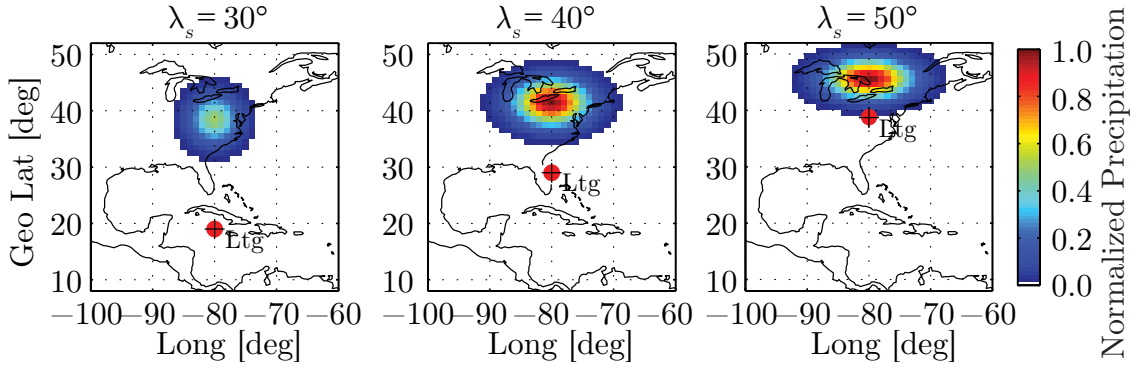


Figure 5.2: Two-dimensional Gaussian model of normalized precipitation fluence hotspot for lightning located at $\lambda_s = 30^\circ$, 40° , and 50° (left to right).

calculations and the DEMETER precipitation observations on an absolute basis but is rather to gain a sense of the relative contribution of lightning in the United States to drift loss cone flux levels. Because our interest lies only in determining the relative precipitation flux contributions, we normalize the precipitation distribution such that the region of strongest precipitation takes on a value of 1, and the regions with no precipitation have a normalized precipitation level of 0. Figure 5.2 shows the size and shape of three such precipitation regions. Comparison of Figures 5.1 and 5.2 demonstrates how closely the Gaussian precipitation model follows the shape and size of the precipitation hot spots proposed by *Lauben et al.* [2001]. Of note in Figure 5.2 is that the maximum normalized precipitation for a lightning discharge at $\lambda_s = 30^\circ$ is $\sim 50\%$ lower than it is for lightning discharges at higher source latitudes. This difference in precipitation strength is related to the fact that the total precipitated energy integrated for all space and time and particle energies $E > 100$ keV in Figure 5.1 is $E_{\text{tot}} = 550$ kJ for $\lambda_s = 30^\circ$, while $E_{\text{tot}} = 1179$ kJ for $\lambda_s = 40^\circ$ and $E_{\text{tot}} = 1120$ kJ for $\lambda_s = 50^\circ$.

For lightning discharges at source latitudes between 30° and 50° , the size and location of the normalized Gaussian precipitation region is interpolated between known source latitudes ($\lambda_s = 30^\circ$, $\lambda_s = 40^\circ$, and $\lambda_s = 50^\circ$) in 1° increments. Lightning discharges with $\lambda_s < 30^\circ$ are not recorded by the NLDN ground-detection network

as these latitude regions fall outside the realm of the continental United States. Lightning discharges with $\lambda_s > 50^\circ$ are assumed to produce a precipitation region in size and strength matching that of $\lambda_s = 50^\circ$, but with the appropriate $\sim 7^\circ$ poleward offset with respect to the source latitude. The oblique whistler precipitation model of [Lauben et al. \[2001\]](#) assumed a reference current magnitude of 10 kA for the modeled lightning discharge. In (5.3) wave power spectral density is seen to be directly proportional to reference current. For simplicity when determining the relative expected flux from each individual lightning discharge, we multiply each normalized precipitation region by the magnitude of the peak current in the respective lightning discharge.

5.3 Expected Precipitation at Satellite Location

Our purpose is to use the Gaussian precipitation model as described above to determine the relative contribution of lightning to the drift loss cone flux values measured on the DEMETER satellite. To do this we begin by examining the satellite orbit and determining which lightning discharges could have contributed to the fluxes measured at each 4 second time step of the satellite trajectory over the continental United States. Recall that electrons experience an eastward drift while traveling in the drift loss cone toward longitudes of the South Atlantic Anomaly. The rate at which the electrons drift in longitude is energy, pitch angle, and L -shell dependent, and the drift period can be approximated as

$$\tau_d = C_d \left(\frac{R_E}{R_0} \right) \frac{1}{\gamma \beta^2} [1 - 0.33333(\sin \alpha_{eq})^{0.62}] \quad (5.4)$$

where $C_d = 1.557 \times 10^4$ s for electrons, $R_0 = LR_E$, $\beta = (v/c)$ is the velocity in terms of the speed of light, $\alpha_{eq} = \text{constant}$ for near loss cone electrons, and $\gamma = (1 - \beta^2)^{-1/2}$ is the relativistic factor [[Walt, 1994](#), p. 49]. The drift period (τ_d) represents the length of time (in seconds) it would take for an electron to drift 360° in longitude.

When determining which lightning discharges may contribute to drift loss cone fluxes at the satellite location, all lightning discharges occurring to the south and west of the satellite location within a fractional drift period must be considered. Because the drift period is energy-dependent, these calculations are repeated for each energy channel of the IDP spectrometer in a separate manner. For every orbit over the United States, for every 4 second time step, for every energy, we first calculate the energy-dependent drift period for electrons at the L -shell corresponding to the satellite's location. Then we consider every lightning discharge to the west and south of the satellite location that occurred within $(\tau_d/6)$ seconds, where the $\frac{1}{6}$ fraction corresponds to a 60° window of time over the United States.

For each possible contributing lightning discharge, we first determine the size and strength of the precipitation region immediately following the lightning discharge. The Gaussian precipitation model presented in the previous section represents a calculation of the relative precipitated electron flux over all space and integrated over approximately three seconds in time. The actual precipitation footprint evolves in time with the energy flux at lower L -shells preceding that for higher L -shells by a few seconds [Lauben *et al.*, 2001, Figure 7]. This later arrival at high L -shells is due to both the longer propagation paths for the wave and the slower velocities of the generally lower resonant energy particles. Conversely, the earlier arrival at low L -shells is due to the faster velocities of the generally higher resonant energy particles and the shorter propagation paths for the wave. The time resolution of the recorded IDP fluxes on the DEMETER satellite is four seconds, and the drift period for resonant energy electrons in the range $100 \leq E_{\text{res}} \leq 500$ is ~ 25 sec/degree. Thus the three second time-integrated precipitation model is adequate for determining the relative expected flux at the satellite location.

Next we use the energy and L -dependence of the drift period to determine where the precipitation region is at the time of the satellite pass. If the precipitation region lies above the satellite location, the causative lightning discharge is assumed to have contributed to the relative expected flux at the given satellite location for the chosen

energy channel. The relative contribution from an individual lightning discharge is calculated by adding the normalized precipitation values for each element of the precipitation hot spot that lies at the same longitude and within $\pm 0.1 L$ of the satellite location, and weighting these values by the magnitude of the peak current of the causative lightning discharge. This final value of relative expected flux is then added to the relative expected flux values from every other lightning discharge whose precipitation region drifted to the satellite location until all possible causative lightning discharges have been accounted for. These calculations are repeated and the results are stored for every four second time step, for every energy channel from 92 keV up to 500 keV, and for every nighttime orbit over the United States.

Figures 5.3 and 5.4 illustrate in graphical and flowchart form the procedure used in determining the relative expected flux at the satellite location. In Figure 5.3, DEMETER passes over Alabama (denoted with a green \times) at 03:40:57 UT on July 7, 2007. Nine minutes prior to this pass, a lightning discharge was recorded on NLDN over Texas (denoted with a red \star). In panel (a), the modeled gaussian precipitation region occurring immediately after the lightning discharge is shown as a two-dimensional hot spot poleward of the lightning discharge. The energy and L -dependent drift period is then calculated to determine where the precipitation region lies at the time of the satellite pass. Panels (b) and (c) illustrate the results of these calculations at two different energies: 126 keV (b) and 304 keV (c). In the case of the 126 keV electrons, the modeled precipitation region lies above the satellite pass, and the relative expected flux from the lightning discharge which occurred at 03:31:53 is determined. The 304 keV electrons, on the other hand, drift at a faster rate and have already passed the satellite location at the time of the pass (03:40:57). The same lightning discharge that contributed to 126 keV fluxes does not contribute to 304 keV fluxes during this instance of the DEMETER pass. The example shown in Figure 5.3 demonstrates the importance of repeating these expected flux calculations for every energy and every lightning discharge.

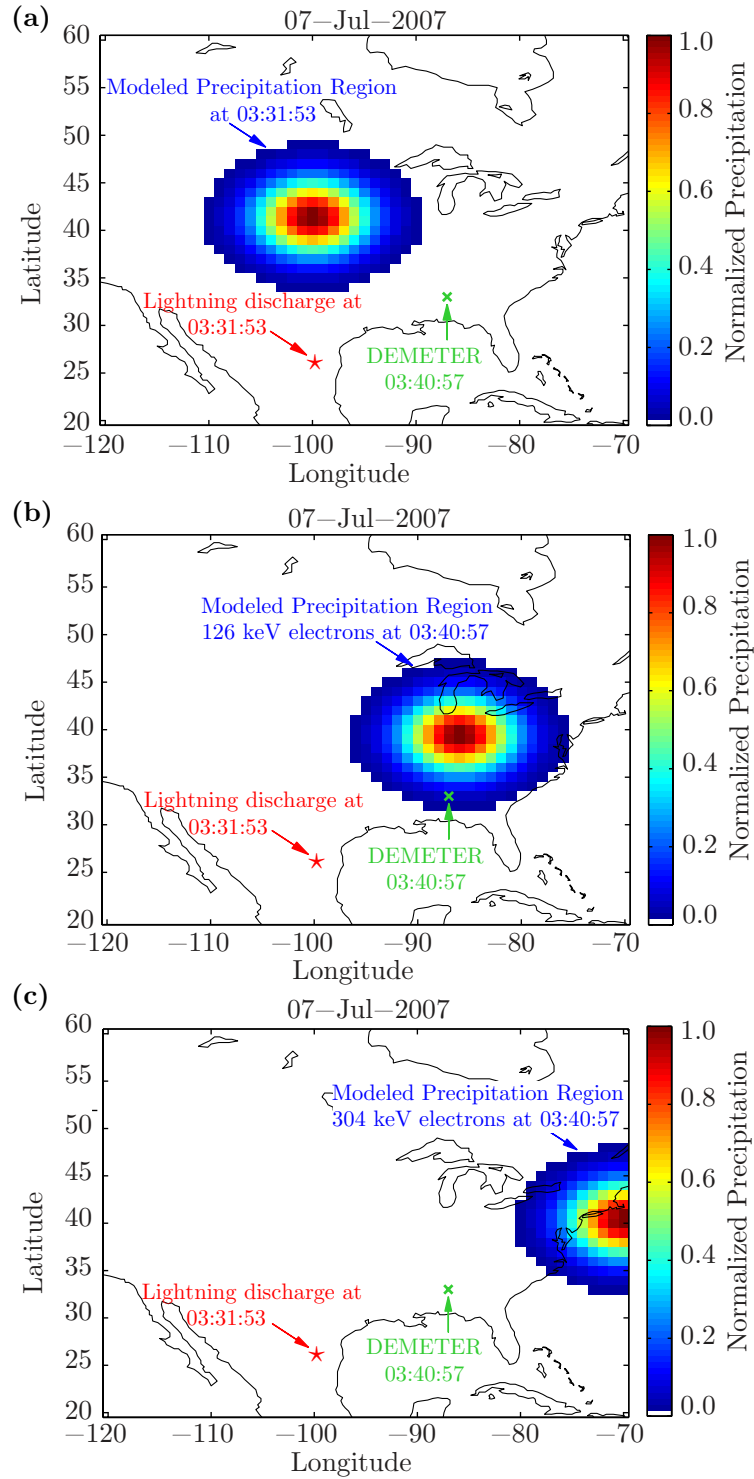


Figure 5.3: (a) Model gaussian precipitation region at time of lightning discharge. (b), (c) Location of the precipitation region at time of satellite pass. If precipitation region is above satellite location as in (b), determine relative expected flux.

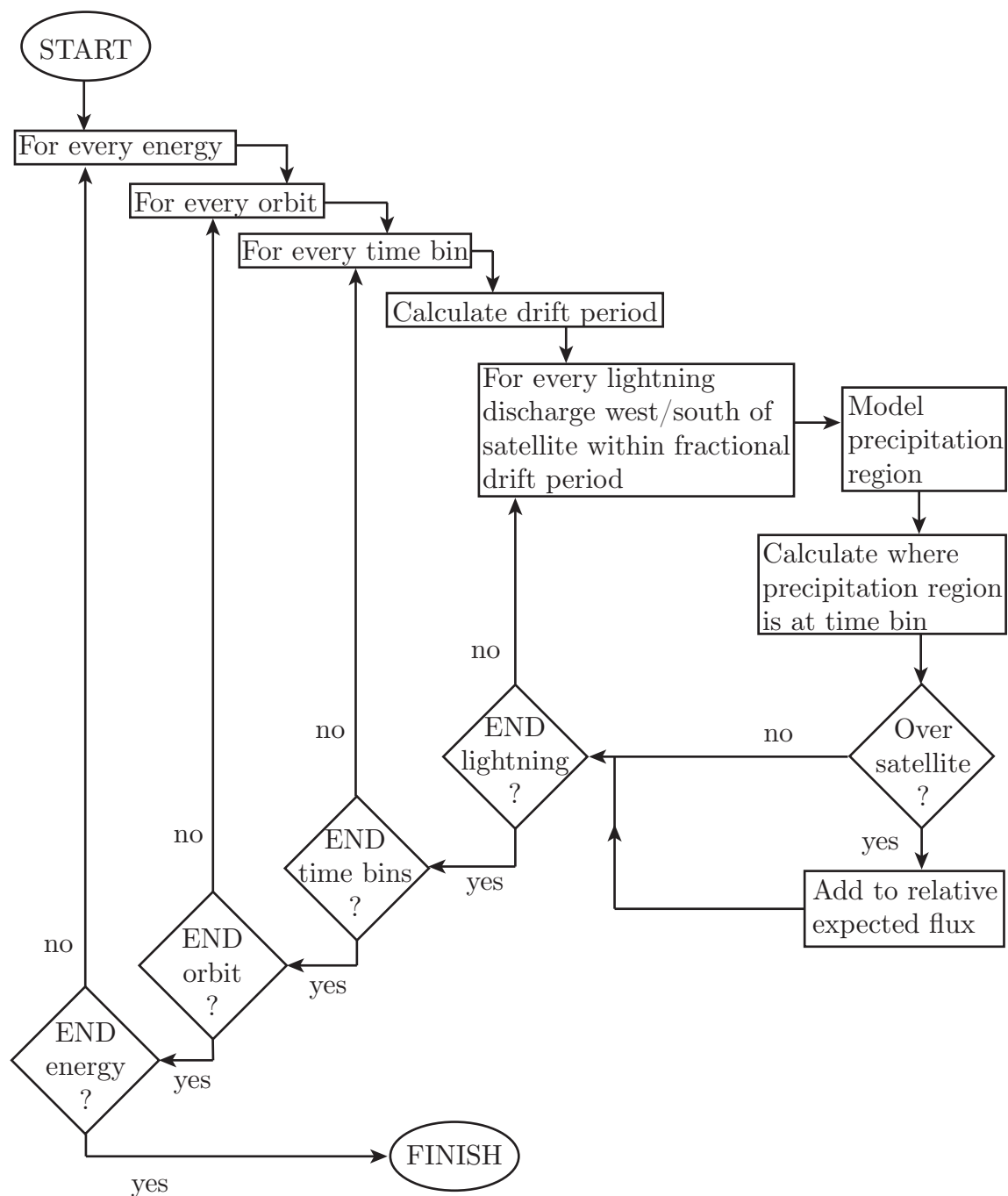


Figure 5.4: Flowchart illustrating the procedure for calculating relative expected flux at the satellite location.

5.4 Comparing Modeled and Measured Fluxes

The calculation of the relative expected flux from known lightning discharges in the above section represents a forward estimation of the drift loss cone fluxes that could have been scattered into the precipitation region by lightning over the United States. Every satellite pass then represents a spatial and temporal window glimpsing a portion of the precipitation we would expect to see given the precipitation model. In order to assess the physical connection between lightning and energetic electron fluxes over the United States, we determine the correlation of modeled, or expected, fluxes with energetic electron fluxes measured by the DEMETER satellite.

We begin by testing the forward estimation model on a known LEP event. Figure 5.5 shows an LEP event recorded on DEMETER on October 6, 2007. The top panel shows the ICE spectrogram of the electric field on DEMETER. The middle panel shows the peak current of lightning discharges over the United States as recorded by NLDN. The blue lines indicate the cloud-to-ground lightning discharges of interest, and the geographic location of the various lightning discharges is marked by + symbols on the map on the right. The larger symbols correspond to discharges with higher peak current, and the blue symbols correspond to the lightning discharges occurring near 02:45:25. The bottom panel shows the spectrum of IDP fluxes on DEMETER for energies < 350 keV. At 02:45:25 UT, a cluster of negative cloud-to-ground lightning discharges over the Atlantic Ocean causes electron precipitation into the bounce loss cone over the satellite location, resulting in a burst of energetic electrons with energies 100–250 keV recorded by the IDP.

We run our forward estimation model of Gaussian precipitation along the small portion of the DEMETER orbit corresponding to the LEP event shown in Figure 5.5 and compare the estimated expected flux values with the actual measured fluxes recorded by the IDP. This comparison is done by correlating the two times series data (between 02:45:15 UT and 02:45:35 UT) of the expected and actual fluxes, and a breakdown of the correlation as a function of resonant electron energies is shown in Figure 5.6. In this figure we see that the estimated expected fluxes agree well with

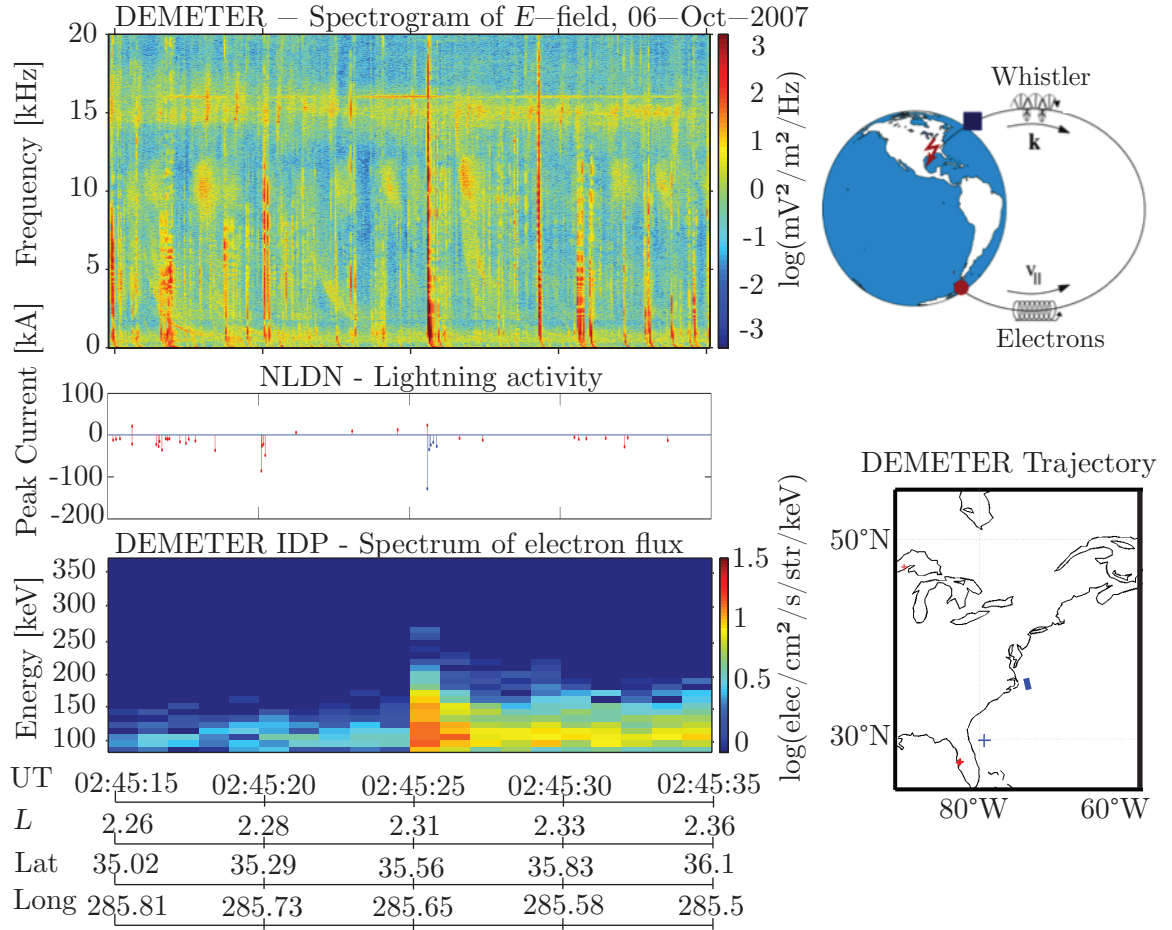


Figure 5.5: LEP event over the eastern United States. Top panel shows a spectrogram of the electric field on DEMETER. Middle panel shows the peak current of lightning discharges over the U.S. as recorded by NLDN. Bottom panel shows the electron spectrum on DEMETER. A map of the DEMETER trajectory during the 20 s time interval is represented with a blue swath on the lower right panel. Red and blue + signs correspond to locations of the red and blue lightning discharges shown in the middle panel on the left.

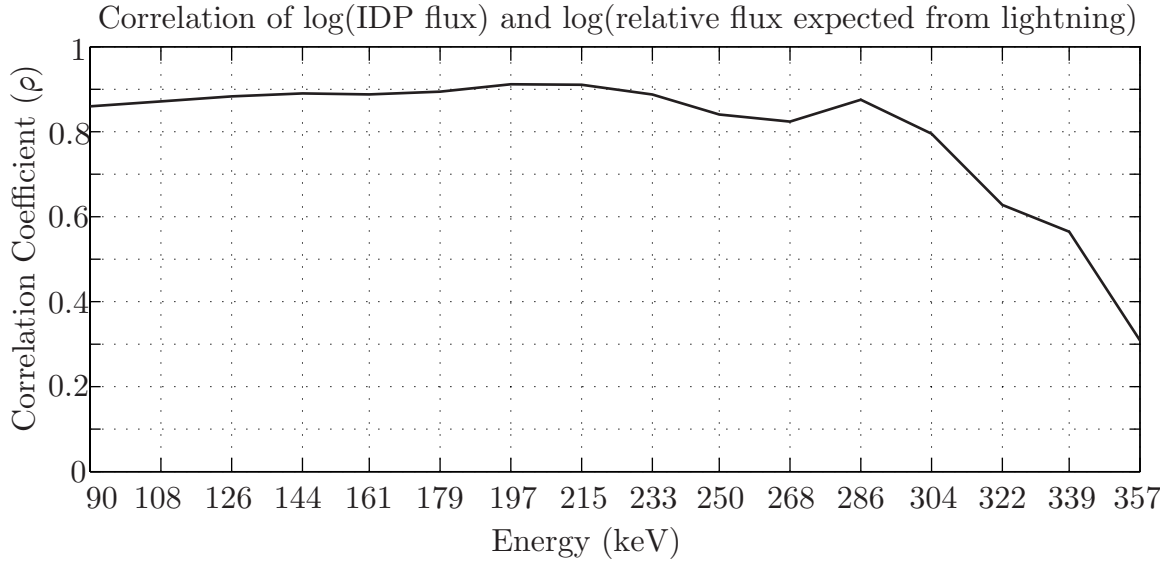


Figure 5.6: Correlation between measured IDP fluxes and relative fluxes expected from lightning on October 6, 2007 between 02:45:15 and 02:45:35 UT, plotted as a function of energy.

recorded fluxes up to ~ 300 keV, where there are no recorded fluxes. The results shown in Figure 5.6 indicate that our forward estimation model works well for the expected energy range of precipitation over the small portion of the orbit shown in Figure 5.5.

5.4.1 Energy and L -shell Characteristics of Precipitation

The drift period of electron precipitation hot spots is dependent on electron energy. Thus, when determining the relative expected flux at the satellite location, the energetic electron energy factors heavily into the selection of lightning discharges likely to have caused precipitation visible to the satellite at a given instance in time. Figures 5.3 and 5.6 demonstrate the sensitivity of the wave-particle interaction model to the energetic electron energy. In addition to taking into account the variation in energy, we also need to consider the variation in L -shell. Figure 5.7 shows a plot of particle precipitation and expected precipitation from lightning as a function of L -shell at a single energy (126 keV), and averaged over the continental United States

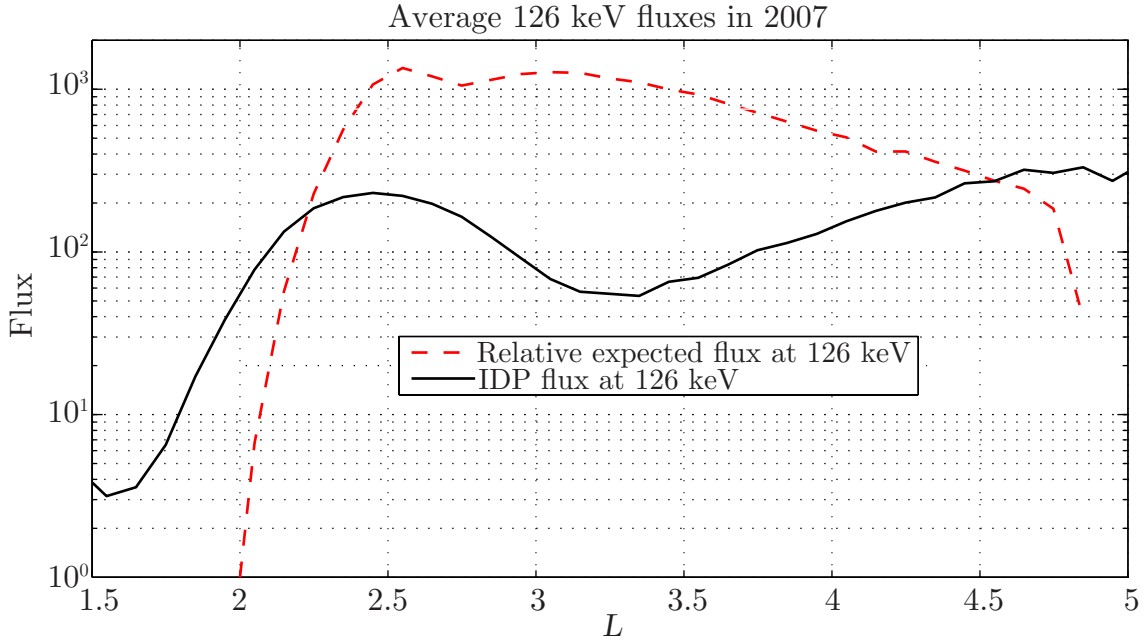


Figure 5.7: Expected and measured flux values as a function of L at 126 keV averaged over the United States in 2007.

in 2007. Both flux distributions are highly dependent on L -shell. In particular, they are both high for certain ranges of L -shell and low for others.

Our objective is to show a relationship between particle precipitation and lightning activity. In order to do this we need to rule out any sort of dependence between the two that comes from the fact that they are both dependent on L -shell. This joint dependence of two variables (expected and measured electron fluxes) on a third (L -shell) is typically taken into account by looking at the data conditioned on L -shell. Ideally when estimating a conditional correlation function, we have a model for the data in mind. For example, we could assume that particle precipitation, lightning activity, and L -shell are jointly Gaussian. Unfortunately, a jointly Gaussian model assumes that both expected and measured fluxes vary linearly with L . As evidenced by Figure 5.7, neither fluxes vary linearly with L . Therefore a jointly Gaussian model is not suitable. In fact, Figure 5.7 shows that a complicated non-linear model is at play. Instead of guessing at an accurate model for the variation of both measured and expected fluxes with L , we perform a very general estimate of the conditional

correlation by binning the particle precipitation and lightning activity data into very small bins ($0.1 L$) based on L -shell and calculate the correlation in each of those bins.

Figure 5.6 shows an example of the correlation between expected and measured flux values over a limited portion of a single orbit. The next step is to extend the methodology used in the correlation of this single example to an entire year by carefully binning the data in L -shell before computing an estimate of the conditional correlation between expected and measured fluxes. Figure 5.8 shows the correlation coefficient, ρ , between measured and expected fluxes as a function of both energy and L -shell for all 2007 nighttime passes over the United States. The colors here range from correlations of 0.5 at the darkest red down to -0.2 at the darkest blue. A strong correlation (e.g., $\rho=0.5$) indicates that the forward estimation of normalized expected flux accurately represents the normalized flux measured on DEMETER, while a weak correlation (e.g., $|\rho|<0.1$) indicates a disagreement between the measured fluxes and the model. The white boxes in Figure 5.8 indicate those regions where the p -value of the correlation was $p>0.05$, meaning the correlations are statistically insignificant [Berkson, 1942]. The correlations are strongest for regions of $L<2.5$ and for energies up to ~ 300 keV. This relationship of strong correlation at low energies and low L is consistent with the model of resonant electron energies seen in Figure 2.6, indicating that cyclotron resonant scattering by lightning plays a prominent role in the loss of trapped radiation in the inner belt and slot regions. Data for other years show a trend similar to that plotted in Figure 5.8.

5.4.2 Seasonal Variations in Energy and L Characteristics

In Figures 5.9, 5.10, 5.11, and 5.12, variations in the correlation between expected and measured fluxes are explored by season. Figure 5.9 shows the spring correlations between IDP fluxes and relative fluxes expected from the lightning precipitation model. For each of the seasonal figures, three months are assumed to represent an individual season, and three years (2006–2008) of data are considered. Thus, the spring correlations of Figure 5.9 represent data for March, April, and May of 2006,

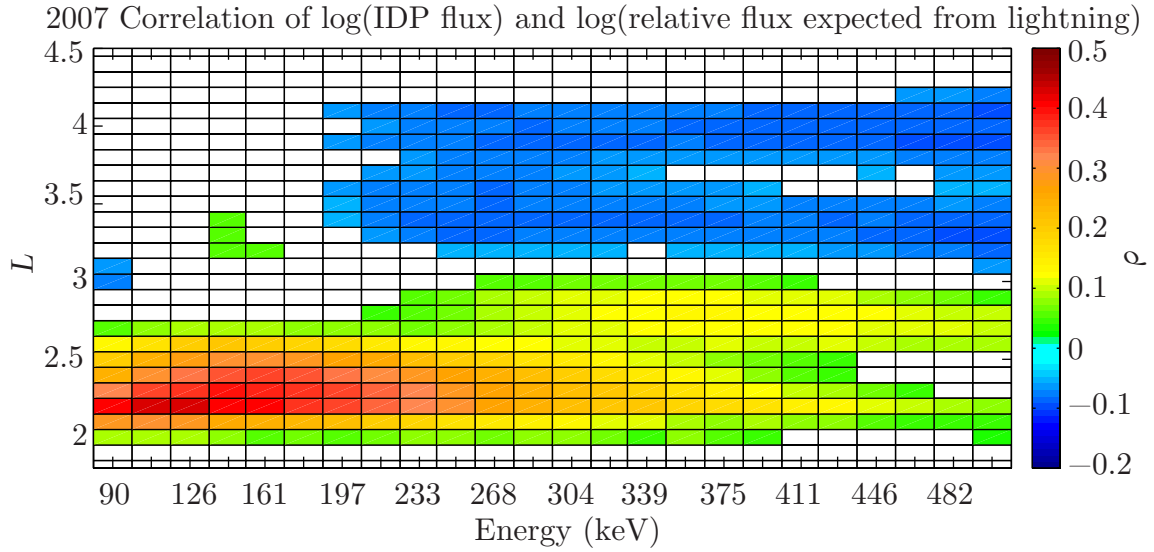


Figure 5.8: Correlation between nighttime measured fluxes in 2007 on DEMETER and relative fluxes expected from lightning based on the Gaussian precipitation model.

2007, and 2008. Summer is taken to occur in June, July, and August, autumn is represented by September, October, November, and winter consists of the months of December, January, and February.

Of particular note in each of the seasonal plots is the behavior in energy and L -shell at values of $L < 2.5$ and $E < 300$ keV—the region where the highest correlations exist on a yearly basis, as seen in Figure 5.8. In spring (Figure 5.9) the peak correlation between estimated expected fluxes at the satellite and measured fluxes on the IDP is ~ 0.35 at $L = 2$. In summer (Figure 5.10) the peak correlation is ~ 0.4 at $L = 2$, and the correlations are strongest at low energies ($E < 200$ keV). Additionally, a weak negative correlation manifests at $L > 3.5$. The summer months experience an abundance of lightning discharges at many source latitudes, resulting in an increase of modeled relative expected fluxes at these higher L -shells. The variation in L -shell between expected relative flux and measured flux (as seen in Figure 5.7) is greater at these L -shells, and the direct estimate of the conditional correlation in bins of $0.1 L$ in width may not be fine enough to estimate the conditional correlation at these higher L -values.

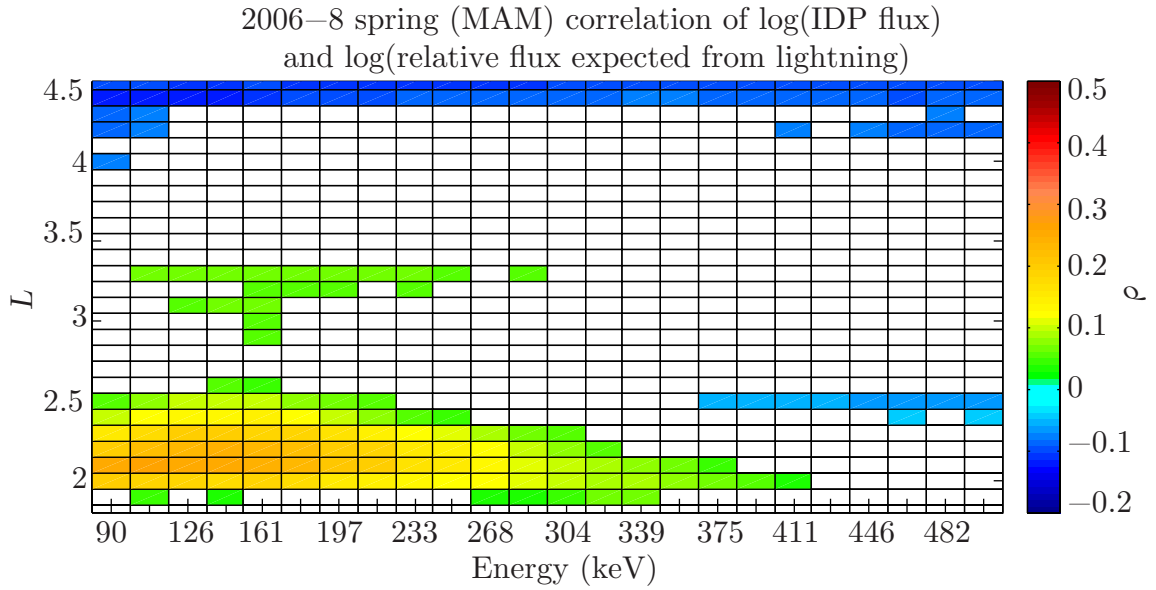


Figure 5.9: Correlation between nighttime measured fluxes during the spring months of March, April, and May (MAM) 2006–2008 on DEMETER and relative fluxes expected from lightning based on the Gaussian precipitation model.

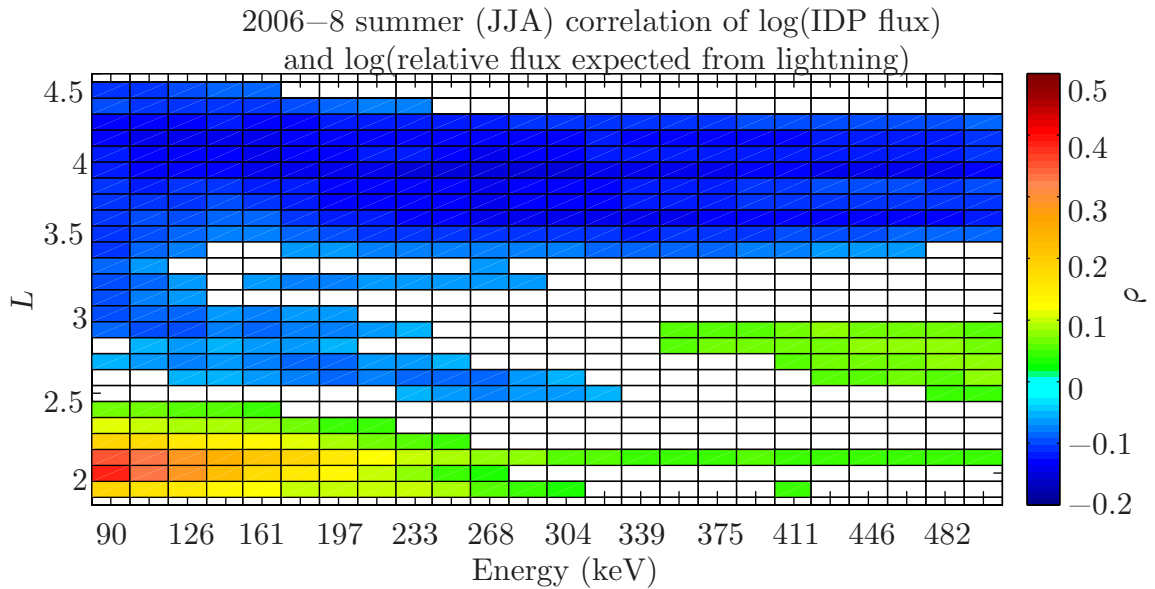


Figure 5.10: Correlation between nighttime measured fluxes during the summer months of June, July, and August (JJA) 2006–2008 on DEMETER and relative fluxes expected from lightning based on the Gaussian precipitation model.

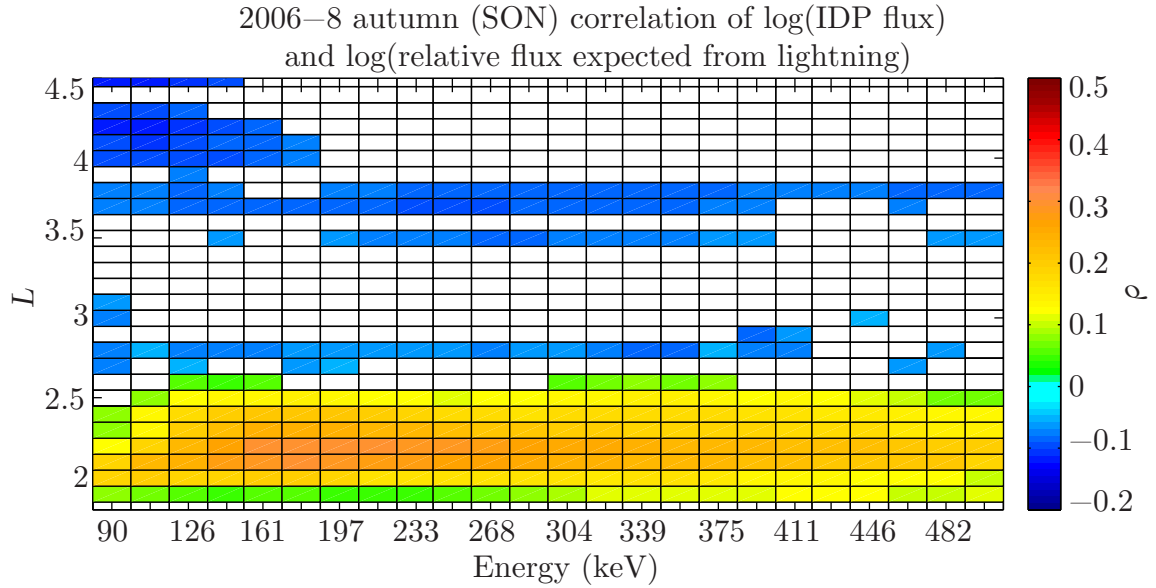


Figure 5.11: Correlation between nighttime measured fluxes during the Autumn months of September, October, and November (SON) 2006–2008 on DEMETER and relative fluxes expected from lightning based on the Gaussian precipitation model.

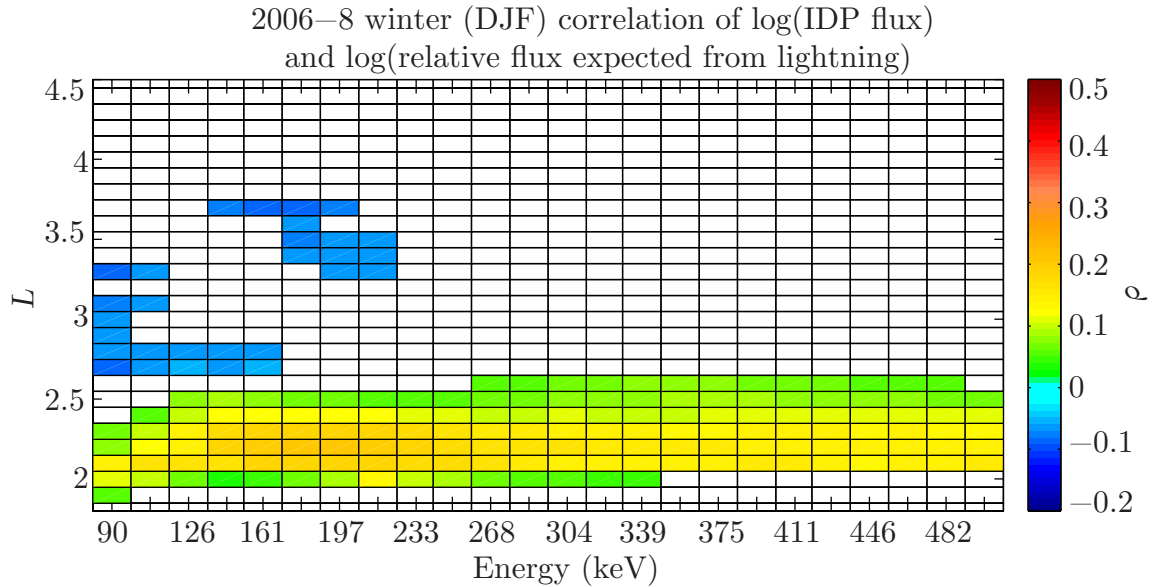


Figure 5.12: Correlation between nighttime measured fluxes during the winter months of December, January, February (DJF) 2006–2008 on DEMETER and relative fluxes expected from lightning based on the Gaussian precipitation model.

Figure 5.11 shows peak autumn correlations of ~ 0.35 at $L < 2.5$, and these peak correlation values persist up to higher energies than they did in the spring and summer months shown in the previous plots. Winter tells a similar story, with peak correlations in Figure 5.12 again extending up to $E = 500$ keV, although in the case of winter, the maximum correlation is on the order of 0.3 (as opposed to 0.4 in the summer). These lower correlation values indicate that while lightning plays a role in radiation belt losses, it is not the only factor at work. Among other possible sources of loss are plasmaspheric hiss, VLF transmitter signals, and lightning discharges which are not of U.S. origin. However, even in the winter when lightning occurrence rates are much lower than in the summer months, lightning is still a prominent source of radiation belt electron loss at mid-latitudes.

5.4.3 Poleward Offset of Precipitation Region

In Section 5.2, the electron scattering calculations modeled a precipitation region of large ionospheric extent that occurs poleward of the causative lightning strike. These calculations are based on an assumption that the whistler waves are nonducted, or obliquely propagating with respect to the magnetic field. A recent study by *Rodger et al.* [2010] compared the effectiveness of ducted and nonducted transmitter-produced VLF waves in driving radiation belt pitch angle scattering. This study focused on two powerful U.S. Navy transmitter signals with call signs NWC ($L = 1.45$) and NPM ($L = 1.17$) that transmit at 19.8 kHz and 21.4 kHz respectively. Well-defined enhancements in drift loss cone electron fluxes produced by the powerful NWC transmitter appear consistent with scattering by ducted waves, whereas nonducted waves propagating away from the low-latitude NPM transmitter produce enhancements that are at least 50 times smaller than those from NWC. This observation leads the authors to conclude that lower-latitude, nonducted VLF waves are less effective in driving radiation belt pitch angle scattering than ducted VLF waves [*Rodger et al.*, 2010].

By changing the distance of the poleward offset of the precipitation region in our electron scattering calculations, we test whether ducted lightning-generated whistler

waves are more effective in driving pitch-angle scattering than obliquely propagating whistler waves. The nonducted precipitation region presented by [Lauben et al. \[2001\]](#) computed a poleward offset of 20° , 13° , and 7° for lightning discharges at $\lambda_s = 30^\circ$, 40° , and 50° , respectively. Using these computed poleward offsets led to a maximum correlation between relative expected 126 keV fluxes and measured 126 keV IDP fluxes of $\rho = 0.43$ at $L = 2.2$ in 2007. When we run the same correlation model and calculate relative expected fluxes with 0° poleward offset (i.e., ducted propagation), the correlation of relative expected fluxes with 126 keV IDP fluxes drops to $\rho = 0.27$ at $L = 2.25$ in 2007. This result of a lower correlation for ducted propagation implies that ducted lightning-generated whistler waves are less likely to have contributed to the measured IDP fluxes than obliquely propagating whistler waves.

We expand the test of ducted propagation to include fractional offsets of the poleward offset of the precipitation region predicted by [Lauben et al. \[2001\]](#). For example, we test the correlation of relative expected fluxes with IDP fluxes if the poleward offset at $\lambda_s = 30^\circ$, 40° , and 50° were 10° , 6.5° , and 3.5° respectively, or one half of the poleward offset calculated by [Lauben et al. \[2001\]](#). At only half of the predicted poleward offset, the correlation of 126 keV IDP fluxes with relative fluxes expected from lightning drops to a maximum value of $\rho = 0.33$ at $L = 2.2$ in 2007. Figure 5.13 shows the results of correlations run between 126 keV IDP fluxes in 2007 and relative expected fluxes from lightning at various poleward offsets. In each case, the maximum correlation across L -shells for $L < 3$ is plotted as a function of the poleward offset of the center of the Gaussian precipitation region. A poleward offset of 0 indicates ducted propagation, while a fractional poleward offset of 1.5 indicates the center of the modeled Gaussian precipitation region lies at 1.5 times the poleward offset assumed by [Lauben et al. \[2001\]](#), i.e., 30° , 19.5° , and 10.5° at $\lambda_s = 30^\circ$, 40° , and 50° respectively.

That the correlation between measured and expected flux values is highest for the original electron scattering model presented by [Lauben et al. \[2001\]](#) indicates that nonducted, obliquely propagating lightning-generated whistler waves are more likely

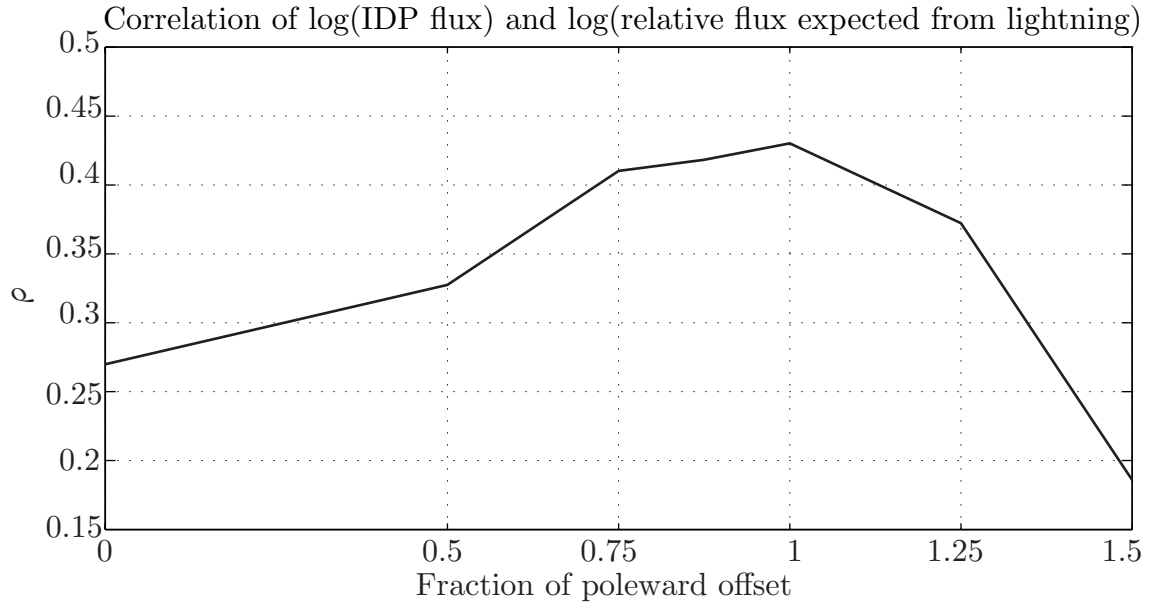


Figure 5.13: Comparison of correlation of 126 keV IDP fluxes in 2007 with relative fluxes expected from lightning based on electron scattering models for both ducted and nonducted propagation. The assumed poleward offset for the center of the precipitation region described by [Lauben et al. \[2001\]](#) is 20° , 13° , and 7° for lightning discharges at $\lambda_s = 30^\circ$, 40° , and 50° , respectively. The peak correlation, ρ , between measured and expected fluxes at $L < 3$ is plotted as a function a fraction of the poleward offset, where the value of 1 on the x -axis represents the poleward offset listed above, a value of 0 describes ducted propagation, and a value of 0.5 describes precipitation regions centered 10° , 6.5° , and 3.5° for lightning discharges at $\lambda_s = 30^\circ$, 40° , and 50° , respectively.

to account for the drift loss cone fluxes measured on DEMETER than ducted waves. The poleward-displacement of lightning-induced electron precipitation is consistent with ground-based observations [*Peter and Inan, 2004*] as well as DEMETER observations of individual bounce loss cone events [*Inan et al., 2007*]. Despite recent suggestions that pitch-angle scattering by VLF transmitters occurs predominantly from ducted propagation [*Rodger et al., 2010*], we find that nonducted whistler waves driven by lightning are more likely than ducted waves to cause drift loss cone precipitation over the United States.

Chapter 6

Summary and Future Work

6.1 Summary

This dissertation details in-situ observations of energetic electron losses from the radiation belts. In particular, we focus on one specific loss mechanism, that from lightning-generated whistler waves, with a goal of globally assessing the role these waves play in the scattering of radiation belt electrons.

Chapter 1 outlines the scope of the dissertation, namely: (i) determination of a seasonal variation of electron precipitation at mid-latitudes that is consistent with lightning as a major loss driver for electrons with energies of a few hundred keV; (ii) identification of the continental United States as an ideal geographic region for measurements of lightning-induced electron precipitation (LEP) events at low earth orbit; and (iii) determination of the relationship between electron precipitation and lightning activity, including dependence on energy and L -shell. In addition to outlining the scope of the overall dissertation, this chapter also reviews the role of LEP events in radiation belt research, describes the Van Allen radiation belts, and introduces the concept of the drift and bounce loss cones.

In Chapter 2 we describe the physics of the wave-particle interactions that lead to lightning-induced electron precipitation. We also explore the relationship between electron energy and the wave magnetic field that leads to gyroresonant pitch-angle scattering of electrons from stably trapped orbits into the drift and bounce loss

cones. We then discuss various methods of measurement of the effects of wave-particle interactions, including VLF remote sensing and in-situ observations of drift loss cone fluxes.

Chapter 3 introduces the instruments used throughout this dissertation to study LEP events in situ: namely the DEMETER satellite and the National Lightning Detection Network (NLDN). This chapter details the DEMETER orbit and describes the regions above which the instrument for particle detection (IDP) samples drift loss cone fluxes. We also discuss the occurrence rates of lightning on a global scale on both a yearly and a seasonal basis, and compare the seasonal distributions of lightning to the seasonal distribution of lightning-generated whistler waves recorded on the electric field instrument (ICE) on board the DEMETER satellite. We observe that lightning occurrence is much higher in the local afternoon and during the local summer months, and that lightning-generated VLF wave activity at 600 km altitude is much stronger over the United States in the summer than at any other time or location across the globe. In addition to this concentration of wave activity over the U.S., the United States is found to be in a fortuitous position for the assessment of global drift loss cone fluxes due to its location near the western edge of the South Atlantic Anomaly where the drift and bounce loss cones merge.

Chapter 4 describes a long term assessment of drift loss cone fluxes over the United States. We discover that energetic electron fluxes (100–300 keV) in the slot region ($2 < L < 3$) are significantly higher in the local summer months than in the local winter months. This seasonal variation of drift loss cone fluxes is found to be consistent with losses driven by lightning-induced electron precipitation, and the energy and L -dependencies of the seasonal variations are explored. In this chapter as well as the next we focus our findings on nighttime values of energetic electron fluxes because the ionospheric absorption of whistler wave power is much higher during the daytime. However, daytime fluxes also are still the order of 2–5 times higher in August (summer) than they are in December (winter), despite the higher ionospheric absorption. At the end of this chapter we explore the yearly variation of fluxes

and lightning and perform a coarse estimate of the correlation between energetic drift loss cone fluxes at a single energy (126 keV) and lightning to determine the statistical dependence between energetic electron precipitation and lightning. We find a correlation of 0.42, which implies that lightning is a significant contributor to drift loss cone fluxes over the United States, but which also suggests that lightning is not solely responsible for all energetic electron precipitation in the slot region.

Chapter 5 describes a more detailed method of determining the role of lightning in electron precipitation over the United States. In this chapter we describe a physical model of lightning-induced electron precipitation that is used as a basis for a forward estimation of the amount of relative flux we would expect to measure at the satellite location if the electrons were scattered by lightning-generated whistler waves. Millions of lightning discharges are assessed to determine the spatial extent of their precipitation regions, and the energy and L -dependencies of the drift period are considered when determining the relative expected flux at the satellite location in each of the 18 keV energy bins corresponding to energy channels on the DEMETER satellite. Each satellite pass therefore represents a spatial/temporal window glimpsing into the expected precipitation hot spots from various lightning discharges across the United States.

After assessing the forward estimation model over three years, we compare the relative expected electron fluxes to the measured IDP fluxes by determining the correlation between the expected and measured flux values. A correlation of 1 would imply that all of the fluxes measured on the satellite were likely scattered by obliquely propagating lightning-generated whistler waves over the United States, while a correlation of 0 would imply that lightning-induced electron precipitation does not account for the measured drift loss cone fluxes. What we find is a peak correlation of ~ 0.42 up to energies of a few hundred keV within the slot region (up to $L \sim 2.5$). These results imply that lightning plays a continuous role in affecting the lifetime of radiation belt electrons, but only for certain energies (100–300 keV) and only at low L -shells ($L < 2.5$).

6.2 Suggestions for Future Work

This dissertation serves as a first step toward the use of in-situ measurements of drift loss cone electron precipitation to estimate the relative importance of LEP events to radiation belt losses (especially in the 100–300 keV range). Future work will hopefully continue along this vein by extending the forward estimation of expected precipitation from lightning to a global model by utilizing a new global network for lightning detection and testing the performance of the forward estimation model under various parameters and physical models. Additionally, we are now entering a solar maximum phase of the solar cycle in which more coronal mass ejections and larger geomagnetic disturbances would affect the background cold plasma densities as well as the amount of trapped radiation levels and variations in the magnetosphere. How these changes affect LEP occurrence rates on a global scale remains to be seen.

6.2.1 Extension of the Forward Estimation Model

The first study which needs to be undertaken is assessment of the global applicability of the forward estimation model for expected precipitation. While the continental United States is an ideal location for assessing the effects of lightning on drift loss cone precipitation, lightning in other regions around the globe may also contribute in a significant way to drift loss cone fluxes. The results presented in this dissertation rely on data from the National Lightning Detection Network. Since then, a technique for long-range lightning geo-location has been developed by *Said et al.* [2010] that could be used to estimate the contribution of global lightning to drift loss cone fluxes. In addition to being limited longitudinally, NLDN data also impose a latitudinal, or L -shell, restriction on the forward estimation model for lightning-induced electron precipitation. Low-latitude lightning discharges that resonate with electrons in the $L < 2$ region are not recorded by NLDN. Thus, all calculations in Chapter 5 are limited to regions $L > 2$. Access to a dataset inclusive of low-latitude lightning discharges

would allow an extension of the analysis of the forward estimation model to lower L -shells where LEP may still be a dominant loss process.

The geo-location technique of *Said et al.* [2010] also allows for the inclusion of intra-cloud flashes, a flash type that is not recorded by NLDN. Incorporation of lightning discharges from a global lightning detection network based on the technique described by *Said et al.* [2010] would provide a more accurate picture of the contribution of global lightning discharges to drift loss cone electron fluxes. Additionally, inclusion of intra-cloud flashes could lead to a better understanding of the relative contribution of the different types of lightning discharges to drift loss cone fluxes.

A more detailed model of the physical process driving lightning-induced electron precipitation may lead to a better representation of the relative contribution of lightning to electron losses. Section 5.2.3 describes a simplified model of a Gaussian precipitation region based on the complex physical model described by *Lauben et al.* [2001]. Due to the computationally-prohibitive nature of the forward estimation model (determination of expected fluxes over 92,000 time steps, evaluating 79,000,000 possible lightning discharges, and repeating these calculations over 25 different energies), a gross simplification of the physical model is necessary. For the purposes of this dissertation, we use a Gaussian precipitation region in size and shape similar to the size and shape of the precipitation hot spots of *Lauben et al.* [2001] that are reproduced in Figure 5.1.

A number of assumptions are inherent to the model of *Lauben et al.* [2001], including an equatorial pitch angle distribution of particles just above the edge of the bounce loss cone and a lightning reference current magnitude of 10.53 kA. Also, the precipitation hot spots are calculated for all electrons with $E > 100$ keV. While the methodology presented herein gives a good first-order approximation of the relative contribution of lightning to drift loss cone fluxes, it is possible to improve upon the results of the forward estimation model by simulating precipitation hot spots in smaller energy intervals and for a wider range of lightning peak current magnitudes. Additionally, quantifying the effect of the shape of the near-loss-cone pitch angle

distribution of the test particles in the simulation of the precipitation hot spots may result in a more accurate representation of the effect of lightning discharges on drift loss cone fluxes.

6.2.2 Effect of Geomagnetic Activity

The time period (2006–2008) covered by this study corresponds to a relatively quiet time in the solar cycle. During periods of strong geomagnetic activity, an increase of solar wind pressure temporarily compresses the magnetosphere while the solar wind magnetic field interacts with the geomagnetic field and transfers energy into the magnetosphere. During these periods of geomagnetic activity, increased fluxes of energetic particles are transported to the inner magnetosphere via inward radial transport. The K_p index [*Bartels et al.*, 1939] is one commonly used proxy of geomagnetic activity. K_p quantifies disturbances in the horizontal component of the Earth’s magnetic field with a value in the range 0–9 with 1 denoting relatively quiet times, and 5 indicating a large geomagnetic storm.

It has been suggested that there is a relationship between geomagnetic activity and the occurrence of detectable LEP events in ground-based measurements [*Leyser et al.*, 1984; *Peter and Inan*, 2004]. During the time of the study presented in this dissertation, average K_p values are less than two, implying that increased fluxes in the slot region are being affected by lightning and are not the result of geomagnetic storms increasing the number of trapped particles available to be precipitated. The relative contribution of magnetospheric conditions and trapped flux populations to the LEP-driven global loss rates of energetic electrons is not yet fully understood. Future analysis of drift loss cone fluxes during geomagnetically active periods would allow for an assessment of the detectability and frequency of occurrence of LEP events in situ as a function of geomagnetic activity.

Bibliography

- Abel, B., and R. M. Thorne, Electron scattering loss in Earth's inner magnetosphere
1. Dominant physical processes, *Journal of Geophysical Research*, *103*, 2385–2396,
doi:10.1029/97JA02919, 1998a.
- Abel, B., and R. M. Thorne, Electron scattering loss in Earth's inner magnetosphere
2. Sensitivity to model parameters, *Journal of Geophysical Research*, *103*, 2397–
2408, doi:10.1029/97JA02920, 1998b.
- Angerami, J. J., and J. O. Thomas, Studies of planetary atmospheres 1. The
distribution of electrons and ions in the Earth's exosphere, *Journal of Geophysical
Research*, *69*, 4537–4560, doi:10.1029/JZ069i021p04537, 1964.
- Bartels, J., N. H. Heck, and H. F. Johnston, The three-hour index measuring
geomagnetic activity, *Terrestrial Magnetism and Atmospheric Electricity (Journal
of Geophysical Research)*, *44*, 411–454, doi:10.1029/TE044i004p00411, 1939.
- Bell, T. F., The nonlinear gyroresonance interaction between energetic electrons
and coherent VLF waves propagating at an arbitrary angle with respect to
the Earth's magnetic field, *Journal of Geophysical Research*, *89*, 905–918, doi:
10.1029/JA089iA02p00905, 1984.
- Berkson, J., Tests of significance considered as evidence, *Journal of the American
Statistical Association*, *37*(219), pp. 325–335, 1942.
- Berthelier, J. J., et al., ICE, the electric field experiment on DEMETER, *Planetary
and Space Science*, *54*, 456–471, doi:10.1016/j.pss.2005.10.016, 2006.

- Blake, J. B., U. S. Inan, M. Walt, T. F. Bell, J. Bortnik, D. L. Chenette, and H. J. Christian, Lightning-induced energetic electron flux enhancements in the drift loss cone, *Journal of Geophysical Research*, 106(A12), 29,733–29,744, doi:10.1029/2001JA000067, 2001.
- Burgess, W. C., Lightning-induced coupling of the radiation belts to geomagnetically conjugate ionospheric regions, Ph.D. thesis, Stanford Univ., CA., 1993.
- Burgess, W. C., and U. S. Inan, Simultaneous disturbance of conjugate ionospheric regions in association with individual lightning flashes, *Geophysical Research Letters*, 17(3), 259–262, doi:10.1029/GL017i003p00259, 1990.
- Carpenter, D. L., Whistler studies of the plasmapause in the magnetosphere 1. Temporal variations in the position of the knee and some evidence on plasma motions near the knee, *Journal of Geophysical Research*, 71, 693–709, doi:10.1029/JZ071i003p00693, 1966.
- Carpenter, D. L., and R. R. Anderson, An ISEE/Whistler model of equatorial electron density in the magnetosphere, *Journal of Geophysical Research*, 97, 1097–1108, doi:10.1029/91JA01548, 1992.
- Chang, H. C., and U. S. Inan, Test particle modeling of wave-induced energetic electron precipitation, *Journal of Geophysical Research*, 90, 6409–6418, doi:10.1029/JA090iA07p06409, 1985.
- Christian, H. J., et al., The Lightning Imaging Sensor, in *ICAE 99 - International Conference on Atmospheric Electricity, 11th*, pp. 746–749, 1999.
- Christian, H. J., et al., Global frequency and distribution of lightning as observed from space by the Optical Transient Detector, *Journal of Geophysical Research*, 108(D1), 4005–4019, doi:10.1029/2002JD002347, 2003.

- Clilverd, M. A., C. J. Rodger, and D. Nunn, Radiation belt electron precipitation fluxes associated with lightning, *Journal of Geophysical Research*, *109*(A12208), doi:10.1029/2004JA010644, 2004.
- Clilverd, M. A., N. P. Meredith, R. Horne, S. A. Glauert, R. R. Anderson, N. R. Thomson, F. W. Menk, and B. R. Sandel, Longitudinal and seasonal variations in plasmaspheric electron density: Implications for electron precipitation, *Journal of Geophysical Research*, *112*(A11210), doi:10.1029/2007JA012416, 2007.
- Cummer, S. A., and U. S. Inan, Measurement of charge transfer in sprite-producing lightning using ELF radio atmospherics, *Geophysical Research Letters*, *24*, 1731–1734, doi:10.1029/97GL51791, 1997.
- Cummins, K. L., E. P. Krider, and M. D. Malone, The US National Lightning Detection NetworkTM and applications of cloud-to-ground lightning data by electric power utilities, *IEEE Transactions on Electromagnetic Compatibility*, *40*(4), 465–480, doi:10.1109/15.736207, 1998.
- Devlin, S. J., R. Gnanadesikan, and J. R. Kettenring, Robust estimation and outlier detection with correlation coefficients, *Biometrika*, *62*(3), 531–545, doi:10.1093/biomet/62.3.531, 1975.
- Dungey, J. W., Loss of Van Allen electrons due to whistlers, *Planetary and Space Science*, *11*(6), 591–595, doi:10.1016/0032-0633(63)90166-1, 1963.
- Gemelos, E. S., U. S. Inan, M. Walt, M. Parrot, and J. A. Sauvaud, Seasonal dependence of energetic electron precipitation: Evidence for a global role of lightning, *Geophysical Research Letters*, *36*(L21107), doi:10.1029/2009GL040396, 2009.
- Goldberg, R. A., J. R. Barcus, L. C. Hale, and S. A. Curtis, Direct observation of magnetospheric electron precipitation stimulated by lightning, *Journal of Atmospheric and Terrestrial Physics*, *48*, 293–299, doi:10.1016/0021-9169(86)90105-4, 1986.

- Green, J. L., S. Boardsen, L. Garcia, W. W. L. Taylor, S. F. Fung, and B. W. Reinisch, On the origin of whistler mode radiation in the plasmasphere, *Journal of Geophysical Research*, 110(A03201), doi:10.1029/2004JA010495, 2005.
- Gurnett, D. A., and U. S. Inan, Plasma wave observations with the Dynamics Explorer 1 spacecraft, *Rev. Geophys.*, 26(2), 285–316, doi:10.1029/RG026i002p00285, 1988.
- Helliwell, R. A., *Whistlers and Related Ionospheric Phenomena*, Stanford Univ. Press, Stanford, 1965.
- Horne, R. B., The contribution of wave particle interactions to electron loss and acceleration in the Earth's radiation belts during geomagnetic storms, in *Review of Radio Science 1999-2002*, edited by W. R. Stone, chap. 33, pp. 801–828, John Wiley, Hoboken, N. J., 2002.
- IGA, International Association of Geomagnetism and Aeronomy, Working Group V-MOD. International Geomagnetic Reference Field: the eleventh generation, *Geophysical Journal International*, 183(3), 1216–1230, doi:10.1111/j.1365-246X.2010.04804.x, International Association of Geomagnetism and Aeronomy, Working Group V-MOD., 2010.
- Imhof, W. L., H. D. Voss, M. Walt, E. E. Gaines, and J. Mobilia, Slot region electron precipitation by lightning, VLF chorus, and plasmaspheric hiss, *Journal of Geophysical Research*, 91, 8883–8894, doi:10.1029/JA091iA08p08883, 1986.
- Inan, U. S., and T. F. Bell, The plasmopause as a VLF wave guide, *Journal of Geophysical Research*, 82, 2819–2827, doi:10.1029/JA082i019p02819, 1977.
- Inan, U. S., and D. L. Carpenter, On the correlation of whistlers and associated subionospheric VLF/LF perturbations, *Journal of Geophysical Research*, 91, 3106–3116, doi:10.1029/JA091iA03p03106, 1986.
- Inan, U. S., H. C. Chang, R. A. Helliwell, W. L. Imhof, J. B. Reagan, and M. Walt, Precipitation of radiation belt electrons by man-made waves: A comparison

- between theory and measurement, *Journal of Geophysical Research*, *90*, 359–369, doi:10.1029/JA090iA01p00359, 1985.
- Inan, U. S., W. C. Burgess, T. G. Wolf, D. C. Shafer, and R. E. Orville, Lightning-associated precipitation of MeV electrons from the inner radiation belt, *Geophysical Research Letters*, *15*(2), 172–175, doi:10.1029/GL015i002p00172, 1988.
- Inan, U. S., M. Walt, H. Voss, and W. Imhof, Energy spectra and pitch angle distribution of lightning-induced electron precipitation: Analysis of an event observed on the S81-1 (SEEP) satellite, *Journal of Geophysical Research*, *94*(A2), 1379–1401, doi:10.1029/JA094iA02p01379, 1989.
- Inan, U. S., F. A. Knifsend, and J. Oh, Subionospheric VLF ‘imaging’ of lightning-induced electron precipitation from the magnetosphere, *Journal of Geophysical Research*, *95*, 17,217–17,231, doi:10.1029/JA095iA10p17217, 1990.
- Inan, U. S., D. Pidgachiy, W. B. Peter, J. A. Sauvaud, and M. Parrot, DEMETER satellite observations of lightning-induced electron precipitation, *Geophysical Research Letters*, *34*, L07,103, doi:10.1029/2006GL029238, 2007.
- Johnson, M. P., and U. S. Inan, Spheric clusters associated with early/fast VLF events, *Geophysical Research Letters*, *27*, 1391–1394, doi:10.1029/1999GL010757, 2000.
- Johnson, M. P., U. S. Inan, and D. S. Lauben, Subionospheric vlf signatures of oblique (nonducted) whistler-induced precipitation, *Geophysical Research Letters*, *26*(23), 3569–3572, doi:10.1029/1999GL010706, 1999.
- Kennel, C. F., and H. E. Petschek, Limit on stably trapped particle fluxes, *Journal of Geophysical Research*, *71*, 1–28, doi:10.1029/JZ071i001p00001, 1966.
- Kimura, I., P. Stubbe, M. T. Rietveld, R. Barr, K. Ishida, Y. Kasahara, S. Yagitani, and I. Nagano, Collaborative experiments by Akebono satellite, Tromsø ionospheric heater, and European incoherent scatter radar, *Radio Science*, *29*(1), 23–37, doi:10.1029/93RS01727, 1994.

- Lagoutte, D., et al., The DEMETER Science Mission Centre, *Planetary and Space Science*, *54*, 428–440, doi:10.1016/j.pss.2005.10.014, 2006.
- Lauben, D. S., U. S. Inan, and T. F. Bell, Poleward-displaced electron precipitation from lightning-generated oblique whistlers, *Geophysical Research Letters*, *26*(16), 2633–2636, doi:10.1029/1999GL900374, 1999.
- Lauben, D. S., U. S. Inan, and T. F. Bell, Precipitation of radiation belt electrons induced by obliquely propagating lightning-generated whistlers, *Journal of Geophysical Research*, *106*, 29,745–29,770, doi:10.1029/1999JA000155, 2001.
- Leyser, T. B., U. S. Inan, D. L. Carpenter, and M. L. Trimpi, Diurnal variation of burst precipitation effects on subionospheric VLF /LF signal propagation near $L = 2$, *Journal of Geophysical Research*, *89*, 9139–9143, doi:10.1029/JA089iA10p09139, 1984.
- Li, X., D. N. Baker, S. G. Kanekal, M. Looper, and M. Temerin, Long term measurements of radiation belts by SAMPEX and their variations, *Geophysical Research Letters*, *28*, 3827–3830, doi:10.1029/2001GL013586, 2001.
- Lyons, L. R., and R. M. Thorne, Equilibrium structure of radiation belt electrons, *Journal of Geophysical Research*, *78*, 2142–2149, doi:10.1029/JA078i013p02142, 1973.
- Lyons, L. R., R. M. Thorne, and C. F. Kennel, Pitch-angle diffusion of radiation belt electrons within the plasmasphere., *Journal of Geophysical Research*, *77*, 3455–3474, doi:10.1029/JA077i019p03455, 1972.
- Meredith, N. P., R. B. Horne, M. A. Clilverd, D. Horsfall, R. M. Thorne, and R. R. Anderson, Origins of plasmaspheric hiss, *Journal of Geophysical Research*, *111*(A09217), doi:10.1029/2006JA011707, 2006.
- Murphy, M. J., and K. L. Cummins, Two-dimensional and three-dimensional cloud discharge detection, in *Int. Lightning Detection Conf.*, Tuscon, AZ, 1998.

- Parrot, M., U. S. Inan, N. G. Lehtinen, and J. L. Pinçon, Penetration of lightning MF signals to the upper ionosphere over VLF ground-based transmitters, *Journal of Geophysical Research (Space Physics)*, 114(A12318), doi:10.1029/2009JA014598, 2009.
- Parrot, M., et al., The magnetic field experiment IMSC and its data processing onboard DEMETER: Scientific objectives, description and first results, *Planetary and Space Science*, 54(5), 441–455, doi:10.1016/j.pss.2005.10.015, 2006.
- Peter, W. B., and U. S. Inan, On the occurrence and spatial extent of electron precipitation induced by oblique nonducted whistler waves, *Journal of Geophysical Research*, 109(A12215), doi:10.1029/2004JA010412, 2004.
- Peter, W. B., and U. S. Inan, A quantitative comparison of lightning-induced electron precipitation and VLF signal perturbations, *Journal of Geophysical Research*, 112(A12212), doi:10.1029/2006JA012165, 2007.
- Rakov, V. A., and M. A. Uman, *Lightning - Physics and Effects*, 698 pp., Cambridge University Press, 2003.
- Reising, S. C., U. S. Inan, T. F. Bell, and W. A. Lyons, Evidence for continuing current in sprite-producing cloud-to-ground lightning, *Geophysical Research Letters*, 23(24), 3639–3642, doi:10.1029/96GL03480, 1996.
- Ristić-Djurović, J. L., T. F. Bell, and U. S. Inan, Precipitation of radiation belt electrons by magnetospherically reflected whistlers, *Journal of Geophysical Research*, 103, 9249–9260, doi:10.1029/97JA03724, 1998.
- Rodger, C., B. Carson, S. A. Cummer, R. Gamble, M. A. Clilverd, J. C. Green, J. A. Sauvaud, M. Parrot, and J. Berthelier, Contrasting the efficiency of radiation belt losses caused by ducted and nonducted whistler-mode waves from ground-based transmitters, *Journal of Geophysical Research*, 115, 208–223, doi:10.1029/2010JA015880, 2010.

- Rodger, C. J., and M. A. Clilverd, Inner radiation belt electron lifetimes due to whistler-induced electron precipitation (WEP) driven losses, *Geophysical Research Letters*, 29(19), 1924–1927, doi:10.1029/2002GL015795, 2002.
- Rycroft, M. J., Enhanced energetic electron intensities at 100 km altitude and a whistler propagating through the plasmasphere, *Planetary and Space Science*, 21, 239–239, doi:10.1016/0032-0633(73)90009-3, 1973.
- Said, R. K., U. S. Inan, and K. L. Cummins, Long-Range Lightning Geo-Location Using a VLF Radio Atmospheric Waveform Bank, *Journal of Geophysical Research*, 115, D23,108, doi:10.1029/2010JD013863, 2010.
- Sauvaud, J. A., et al., High-energy electron detection onboard DEMETER: The IDP spectrometer, description and first results on the inner belt, *Planetary and Space Science*, 54 (5), 502–511, doi:10.1016/j.pss.2005.10.019, 2006.
- Thorne, R. M., R. B. Horne, and N. P. Meredith, Comment on “On the origin of whistler mode radiation in the plasmasphere” by Green et al., *Journal of Geophysical Research*, 111(A09210), doi:10.1029/2005JA011477, 2006.
- Vernov, S. N., I. A. Savenko, L. V. Tverskaya, B. A. Tverskoy, and P. I. Shavrin, On the asymmetry of the intensity of fast electrons in conjugate points at low altitude, *Advances in Space Research*, IV, 392, 1965.
- Voss, H. D., M. Walt, W. L. Imhof, J. Mobilia, and U. S. Inan, Satellite observations of lightning-induced electron precipitation, *Journal of Geophysical Research*, 103, 11,725–11,744, doi:10.1029/97JA02878, 1998.
- Voss, H. D., et al., Lightning-induced electron precipitation, *Nature*, 312, 740–742, doi:10.1038/312740a0, 1984.
- Walt, M., *Introduction to geomagnetically trapped radiation*, Cambridge University Press, 1994.

Weidman, C. D., E. P. Krider, and M. A. Uman, Lightning amplitude spectra in the interval from 100 kHz to 20 MHz, *Geophysical Research Letters*, 8, 931–934, doi:10.1029/GL008i008p00931, 1981.